NTNU

Norwegian University of
Science and Technology

Investigation of Unoccupied Electronic Bands in Graphene

Tomas Hadamek

MSc in Physics
Submission date: June 2018
Supervisor: Justin Wells, IFY

Norwegian University of Science and Technology
Department of Physics

Abstract

In recent years, a lot attention has been paid to various two-dimensional materials due to their unique properties stemming from the spacial refinement of one of the material's dimensions. Regardless of the incredible theoretical and experimental attention on graphene, unoccupied electronic bands are not yet well understood and there is a wealth of contradictory information in the literature about the band origin.

In this thesis, unoccupied electronic graphene states are investigated with a special focus on the lowest unoccupied bands rising from the valence atomic orbitals ($2s$, $2p_x$ and $2p_z$) localized in the graphene layer, known as the σ^* states. As a tool for the unoccupied band structure study, an inverse photoemission spectroscopy, is utilized.

To theoretically predict the spectrum which can be expected from measurements of the σ^* bands, graphene band structure is calculated from a tight-binding model. The so-called "three step model" is used and together with a dipole and free-electron initial state approximation results in the expected inverse photoemission spectrum. In order to account for possible many-body effects which are present in the occupied electronic bands and which can also be expected in the unoccupied electronic bands, electron-phonon coupling is included in the model.

A characterization of the NTNU laboratory inverse photoemission apparatus reveals the resolution being too poor for the intended measurements. The final experiment is performed at Physikalisches Institut, Münster, and shows a single electronic band about 3.5 eV above the Fermi level. The intensity of the measured peak is found to be non-vanishing at normal electron incidence which contradicts the calculated spectrum. The width of the peak and its position with respect to the vacuum level suggest that this peak originates from the two lowest graphene image-potential states which questions previously published inverse photoemission measurements.

Preface

This thesis as a part of two year Master of Science degree in physic is submitted to Norwegian University of Science and Technology (NTNU, Trondheim) to fulfil formal requirements of the degree. The work corresponds to 60 out of a total 120 ECTS credits and was carried out from August 2017 to June 2018. In this thesis, graphene's electronic band structure is investigated, both experimentally and theoretically, in order to understand the origin of the previously reported unoccupied electronic bands. This project was created as a free continuation of previous research related to electron-phonon coupling in graphene with

This work has been performed at NTNU, mainly in the spectroscopic laboratory, with final experiments carried out at Physikalisches Institut, Münster, within a group of Prof. Dr. Markus Donath.

Trondheim, June 2018

Tomáš Hadámek

Acknowledgment

First of all, I would like to thank my supervisor Assoc. Prof. Dr. Justin W. Wells who allowed me to work within his group. I would also like to thank him for his patience and the many fruitful discussions we had over the course of my studies. Additionally, I greatly appreciate the opportunities provided to me for international collaboration. I would also like to thank all the other group members who contributed to the discussions and to the friendly working environment, and especially Alex Schenk for his patience during my introduction to vacuum technology.

I would also like to acknowledge Prof. Dr. Markus Donath without whom the final measurements would not have been possible. I thank him and all his group members who supported us during the measurements.

Finally, I thank my friends, my girlfriend Ingeborg and my family for their support during my work. The biggest acknowledgement, however, belongs to my parents without whom I would never study at NTNU.

T.H.

Contents

Abstract i
Preface ii
Acknowledgment iii

1 Introduction **3**

2 Background **7**
2.1 Two-Dimensional Materials 7
2.1.1 Graphene and Graphite 7
2.1.2 Electrons in Periodic Systems 9
2.1.3 Graphene Electron Structure and Electron Bands 10
2.1.4 Image Potential States 12
2.1.5 Phonons in Two-dimensional Materials 12
2.1.6 Electron-phonon Interactions 14
2.2 A Short Overview Of Experimental Methods 15
2.2.1 Techniques for Band Structure Investigation 16
2.2.2 Methods to Investigate Surface Quality 18
2.3 Inverse Photoemision Spectroscopy 19
2.3.1 Basic Theory 19
2.3.2 Working Modes 20
2.3.3 Construction 21

3 Theory and Computational Approach for IPES Spectrum Simulations **25**
3.1 Band Structure Calclations 25
3.1.1 Tight-Binding Model 26
3.1.2 Construction of Bloch Waves 27
3.1.3 Secular Equation 28
3.1.4 Tight-Binding Model for Graphene 29
3.2 Many-Body Effects 32
3.2.1 Introduction to Green's Functions 32
3.2.2 Green's Function of Free Particles and the Spectral Function 33

3.2.3 Quasi-Particles Picture and Self-energy . . . 34
3.2.4 Spectral Function for Interacting Particle . . . 35
3.2.5 Modelling Electron-Phonon Coupling . . . 36
3.3 Revision of the IPES Theory and Matrix Element Calculation . . . 38
3.3.1 IPES Intensity in Ideal Systems . . . 38
3.3.2 Instrumentation and Many-body Effects . . . 40
3.3.3 The Interaction Hamiltonian . . . 42
3.3.4 Calculation of Matrix Elements . . . 43

4 Computational Results **47**
4.1 Band Structure Calculations . . . 47
4.2 Self-Energy and the Spectral Function . . . 48
4.3 Matrix Elements . . . 49
4.4 The Total IPES Spectrum . . . 50

5 Experimental and Analytical Methods **53**
5.1 Characterization of The Electron Beam . . . 53
5.1.1 Experimental Method . . . 54
5.1.2 Realisation of the Experiment . . . 54
5.1.3 Fitting Procedure . . . 55
5.1.4 Electron Beam Divergence and Momentum Uncertainty . . . 56
5.2 Characterization of Apparatus Energy Resolution Function . . . 56
5.2.1 Experimental Methods . . . 56
5.2.2 Realisation of the Experiment . . . 57
5.2.3 Analytical Method . . . 57
5.3 Graphene Measurements . . . 57
5.3.1 Experimental Method . . . 58
5.3.2 Analytical Method . . . 58

6 Experimental Results **59**
6.1 NTNU Apparatus Characterization . . . 59
6.1.1 Electron Beam Measurements . . . 59
6.1.2 Energy Resolution . . . 64
6.2 Experiments on Graphene . . . 65
6.2.1 LEED . . . 65
6.2.2 IPES . . . 65

7 Discussion **69**
7.1 Apparatus Characterization . . . 69
7.1.1 Beam Profile . . . 69
7.1.2 Momentum Uncertainty . . . 70

7.1.3 Energy Resolution 70
7.2 Model Justification 71
7.3 IPES Graphene 74
7.4 Final Thoughts and Further Work 77

8 Conclusion **79**

A Acronyms **81**

B Additional Figures and Theory **83**
B.1 Decomposition of Atomic Orbitals 83
B.2 The Full Form of The Transfer and Overlap Integral Matrices for Graphene 83
B.3 Real Atomic Orbitals 85
B.4 Energy Resolution Analysis of Instrument Data-Sheet 87
B.5 Standard Deviation of Calculated Parallel Momenta Deviation 88

Bibliography **89**

Chapter 1

Introduction

Despite the first theoretical study of graphene published in 1947 [1], graphene and other two-dimensional (2D) materials served mostly as a toy model for theoretical physicists. It was believed that a single layer graphene sheet was thermally unstable, which was, however, proven not to be true in 2004 when a single-layer graphene sheet was mechanically exfoliated for the first time [2]. This achievement and successive characterization were awarded the Nobel prize in Physics in 2010 [3]. Due to advances in graphene production [4, 5], graphene can be easily prepared and became commercially available.

The accessibility of graphene allowed the convergence of theoretical and experimental condensed matter physics since the two-dimensional phenomenon became suddenly accessible for experiments. Many predictions, such as the anomalous quantum hall effect were observed [6], confirming the theoretical work. Due to its extraordinary electron mobility [7], strong non-linear optical properties [8], flexibility and being the strongest material known [9], graphene promises huge application potential in almost any possible field. The nature of graphene theoretically being a zero-gap material with linear energy dispersion has prompted prompted the investment of much effort in band gap opening [10, 11, 12]. This together with the extraordinary electron mobility promises a new era of electronics [13, 14, 15]. Further spatial confinement into graphene quantum dots and graphene nanoribbons extends its applicability even further towards optoelectronic devices [16, 17, 18] and photovoltaic technology [19]. Moreover, recently revealed superconductivity [20, 21] and other topological states of matter [22, 23] in bilayer (BL) graphene has opened its way to spintronics, vallaytronics and quantum computing.

In order to tailor the properties for future applications, a deep understanding of basic properties and their origin is required. This leads to a consequent need for a good understanding of electronic band structure, which directly effects electrical and optical properties of graphene.

The valence bands of graphene have been well characterized using various techniques, the most powerful and versatile of which is angle-resolved photo angle-resolved photoemission spectroscopy (ARPES)[24] which provides a full picture of the valence bands and confirms theoretical predictions [25]. Despite this apparent corroboration, upon closer inspection deviations from the the theoretically predicted Dirac cone were found and attributed to electron-electron and electron-phonon coupling [26, 27]. The electron-phonon coupling effects were proven to be even stronger in the top-most intralayer states, and can even be observed in ARPES data by the naked eye [28, 29]. The strong electron-phonon coupling is of high interest since it serves as a mediator for Bardeen–Cooper–Schrieffer superconductivity [30, 31], which was already reported in the graphene-like system, MgB_2 [32].

In the conduction bands, however, the electronic structure is not well understood. Several first principle (*ab initio*) [33, 34] and tight binding (TB) simulations [35] were presented, showing different positions of the lowest unoccupied intralayer σ^* bands and assigning different origins to the lowest unoccupied states. Moreover, to the best of the authors' knowledge, no complete momentum resolved band mapping of graphene states above the vacuum level has been performed. The lowest energy region below the vacuum level was measured by two-photon photoemission spectroscopy (2PPES) [36] and the observed bands were assigned to image-potential states, which is also supported by *ab initio* calculations [37]. Be that as it may, in Ref. [34], the bands were predicted to be ordinary Kohn-Sham LDA energy bands rather than image-potential states. In addition to the previous work, a state at approximately the same energy (4 eV above the Fermi level) was measured using inverse photoemission spectroscopy (IPES) [38, 39, 40] and was identified as the σ^* state. According to the previously mentioned *ab initio* calculations, this state should be present at much higher energies. In graphite (layered graphene), simulations of the conduction bands [41] showed an additional interlayer σ^* state at a very similar energy to the observed graphene peak. This state should, however, not be present in graphene since it originates from wavefunctions localized between the stacked graphene sheets. Moreover, from the IPES experiments performed on graphite, the presence of the interlayer σ^* band could not be confirmed [42, 43] and later image potential states were found at approximately the same energy [44].

The confusion about the graphene band origin in the literature is rather surprising, considering that graphene is structurally one of the simplest possible materials to model, and therefore deserves attention.

Objectives

The main aim of this thesis is to investigate what spectrum can be expected at the lowest unoccupied intralayer σ^* bands of grapene in the IPES experiment and consequently compare the data to real IPES measurements. To the authors' best knowledge, the IPES intensity from the lowest intralayer σ^* band has not been calculated before, but is rather essential to fully understand the experimental result. The band origin should be directly reflected in the IPES spectra, similarly to ARPES [28, 29], due to practically time-reversed processes in both spectroscopic methods. The completion of this work will allow a better understanding of the unoccupied bands, and thus will enable further investigation of many-body effects, such as electron-electron and electron-phonon interactions.

Methods and Structure of the Thesis

The main content of this thesis begins in Chapter 2, with an introduction of basic solid-state concepts, graphene band structure, and potential processes which can strongly effect the band structure. Consequently, a short overview of spectroscopic techniques and techniques to investigate sample surface quality is given. The chapter is terminated by an introduction to IPES which is the central part of this thesis.

Chapter 3 introduces theoretical necessities for the IPES spectra calculation. A tight-binding model for graphene is described in order to calculate graphene band structure. A many-body theory follows to account for electron-phonon coupling which also has to be considered in the unoccupied bands [45]. In the last section, the three-step model for IPES is described and together with a free-electron like initial state and a dipole approximation, and an expression for expected IPES intensity is derived. Chapter 4 then summarizes the results from the simulations.

Chapter 5 presents experimental methods. The first part focuses on a characterization of the IPES apparatus available at the NTNU laboratory in the department of Physics. Both the experimental approach and the analytical methods are given. The second part of the chapter introduces the actual graphene measurements. The results of both experimental parts are then presented in Chapter 6.

Chapter 7 discusses the results and possibilities of further work. The whole thesis is then summarized in Chapter 8.

Chapter 2

Background

In this first chapter concepts central to this thesis are introduced. The purpose of this chapter is to provide a general framework and insight to the topic, rather than an exact mathematical formulation. First, basic nomenclature and graphene structure are described, followed by an introduction to the band structure of graphene and related phenomena directly effecting it. In the second section, a brief discussion about both structural and spectroscopical experimental methods is given. The last section then focuses on an introduction to inverse photoemission spectroscopy, which plays a central role within this thesis.

2.1 Two-Dimensional Materials

Up to this point, 2D materials have been mentioned several times, however no proper definition of 2D materials has been given which deserves clarification. Within this work, 2D material can be defined as a material heaving periodicity in two of the dimensions, but with a reduced periodicity in the third dimension. This, as will be shown later, directly effects a behaviour of electrons. Due to the atomic scale, crystal dimensions in the order of a few μm can be seen as infinite and the two dimensional character is assigned just to mono- or few-layer materials, such as graphene, hexagonal boron nitride, silicene[46] or borophene[47]. In the following, the focus is on graphene even though some parts are rather general.

2.1.1 Graphene and Graphite

Graphene is formed out of carbon atoms arranged in a honeycomb lattice and is schematically depicted in the figure 2.1a). This honeycomb lattice can be described by a unit cell (depicted by a red rhombus), the smallest unit which possesses a discrete transla-

tion symmetry defined by lattice vectors $\boldsymbol{a}_1$ and $\boldsymbol{a}_2$, which contains two inequivalent carbon atoms (deleted by white and grey point). Their linear combination, $\boldsymbol{R}$, spans the whole triangular Bravais lattice and can be written as

$$\boldsymbol{R} = n_1\boldsymbol{a}_1 + n_2\boldsymbol{a}_1,$$

where n_i are integers and where $\boldsymbol{R}$ will be also referred to as a lattice site.

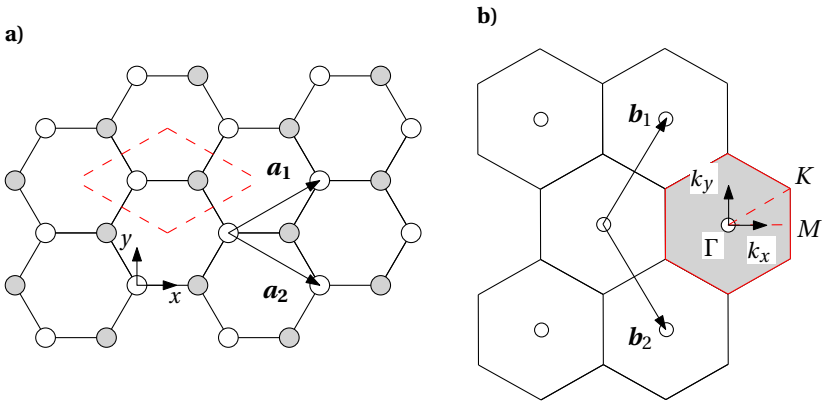

Figure 2.1: Schematic graphene structure a) and graphene's reciprocal space b). In the panels a), the red rhombus denotes a unit cell and $\boldsymbol{a}_i$ are unit vectors in real space. Two sets of inequivalent carbon atoms are denoted by white and grey dots. In the panel b), first Brillouin zone is showed by red shaded hexagon with Γ, M and K being the high symmetry points of the zone, $\boldsymbol{b}_i$ denotes reciprocal lattice vectors and white points corresponding reciprocal lattice points.

Due to discrete translation symmetry of the system, any quantity possesses the same symmetry $f(\boldsymbol{r}) = f(\boldsymbol{r}+\boldsymbol{R})$ and can therefore be described by a Fourier series $f(\boldsymbol{r}) = \sum f_m e^{i\boldsymbol{G}_m\cdot\boldsymbol{r}} = \sum f_m e^{i\boldsymbol{G}_m\cdot\boldsymbol{r}} e^{i\boldsymbol{G}_m\cdot\boldsymbol{R}}$, where f_m are the Fourier coefficients and $\boldsymbol{r}$ is the position vector. This also defines the reciprocal lattice as a set of all $\boldsymbol{G}_m$ satisfying $e^{i\boldsymbol{G}_m\cdot\boldsymbol{R}} = 1$. Consequently, any point of the reciprocal lattice can be described similarly to the real space as $\boldsymbol{G} = m_1\boldsymbol{b}_1 + m_2\boldsymbol{b}_1$, where m_i are integers and $\boldsymbol{b}_i$ are the reciprocal lattice vectors which satisfies $\boldsymbol{a}_i\cdot\boldsymbol{b}_j = 2\pi\delta_{ij}$, with δ_{ij} being Kronecker delta.

The reciprocal space of graphene together with reciprocal lattice points (white dots) and reciprocal lattice vector are displayed in the figure 2.1b). The black hexagons denote Wigner-Seitz cells, known also as Brillouin zones (BZ), are the unit cells of the reciprocal space. The first Brillouin zone (1BZ)[1] is grey-shaded and shows the high symmetry point of the Brillouin zone, Γ, M and K, the dashed red lines show the high symmetry lines of the zone.

[1] Similarly, second Brillouin zone is abbreviated as 2BZ.

The description of graphene given up to this point concerned only mono-layer (ML) graphene. In the experiments both ML, bi-layer (BL) and tri-layer (TL) graphene is used. The stacking of the graphene layers then directly effects graphene properties and to the previously mentioned superconductivity.

Similarly, graphite is nothing but many layers of graphene layered on top of each other (it can be seen as a quasi 2D material). Due to much larger distance between the layers than between the carbon atoms (3.35 Å [48] versus 1.42 Å[49]), graphene layers just weakly interact with each other and many properties of graphene can therefore be judged from graphite.

2.1.2 Electrons in Periodic Systems

As firstly shown by Bloch, in the system that possess translation symmetry (periodic crystals), the eigenstates of Hamiltonian are of the form

$$\psi_{\mu\boldsymbol{k}}(\boldsymbol{r}) = e^{i\boldsymbol{k}\cdot\boldsymbol{r}}\, u_{\mu\boldsymbol{k}}(\boldsymbol{r}), \tag{2.1}$$

with $u_{\mu\boldsymbol{k}}(\boldsymbol{r})$ having the same translation symmetry as the original system which reflects the variation of the wavefunction within the unit cell. This formulation is generally known as Bloch's theorem[2]. The index μ is a band index and $\boldsymbol{k}$ is a wave vector of corresponding eigenstate, known as a Bloch state. The wave vector $\boldsymbol{k}$

Considering $\boldsymbol{k} = \boldsymbol{k}' + \boldsymbol{G}$, where $\boldsymbol{G}$ is any lattice reciprocal vector, the wavefunction can be written as

$$\psi_{\mu\boldsymbol{k}}(\boldsymbol{r}) = e^{i(\boldsymbol{k}'-\boldsymbol{G})\cdot\boldsymbol{r}}\, u_{\mu\boldsymbol{k}'-\boldsymbol{G}}(\boldsymbol{r}) = e^{i\boldsymbol{k}'\cdot\boldsymbol{r}} e^{-i\boldsymbol{G}\cdot\boldsymbol{r}}\, u_{\mu\boldsymbol{k}'-\boldsymbol{G}}(\boldsymbol{r}). \tag{2.2}$$

Defining $u_{\mu\boldsymbol{k}'}(\boldsymbol{r}) = e^{-i\boldsymbol{G}\cdot\boldsymbol{r}}\, u_{\mu\boldsymbol{k}'-\boldsymbol{G}}(\boldsymbol{r})$ the wavefunction can be expressed as

$$\psi_{\mu\boldsymbol{k}}(\boldsymbol{r}) = e^{i\boldsymbol{k}'\cdot\boldsymbol{r}}\, u_{\mu\boldsymbol{k}'}(\boldsymbol{r}) = \psi_{\mu\boldsymbol{k}'}(\boldsymbol{r}). \tag{2.3}$$

The consequence is that crystal momentum is not well defined and $\boldsymbol{k}$ can be modulated by any $\boldsymbol{G}$ without effecting the wave function. This shows that all the information about the particle (electron) wavefunction can be obtained just from the 1BZ. Similarly, electronic band structure (eigenenergy of the system $E_{\boldsymbol{k}\mu}$) of infinite crystals can be determined just by working in the 1BZ.

Since electrons are fermions they must obey Fermi-Dirac statistics

$$f_{\boldsymbol{k}\mu}(E_{\boldsymbol{k}\mu}) = \frac{1}{e^{\frac{E_{\boldsymbol{k}\mu}-E_{\mathrm{F}}}{k_{\mathrm{B}}T}} + 1}, \tag{2.4}$$

[2] For the proof of Bloch's theorem see for example Ref. [50] or Ref. [51].

where $E_{\boldsymbol{k}\mu}$ are eigenenergies of the system, $k_{\mathbb{B}}$ is the Boltzmann constant, T denotes temperature and where E_{F} is the Fermi energy (or Fermi level) - lowest energy occupied by electrons at temperature $T = 0$ K.

If one of the dimensions is reduced, the wave function cannot be periodic within that dimension and has to rapidly decay with the distance from the sample. This corresponds to a particle (an electron) localized in the thin layer of the 2D material.

2.1.3 Graphene Electron Structure and Electron Bands

As mentioned previously, graphene structure is made out of carbon atoms. The carbon atom itself has 6 electrons, 2 core electrons occupying $1s$ orbital, and 4 valence electrons occupying $2s$, $2p_x$,$2p_y$ and $2p_z$. In the following, s, p_x, p_y and p_z will denote the valence orbitals if not mentioned otherwise.

Due to graphene's structure the valence orbitals are sp^2 hybridized which is schematically depicted in the figure 2.2. The p_x remains still localized out of the $x-y$ plane, whereas in-plane orbitals s, p_x, p_y give a rise to new hybridized orbitals p_a, p_b and p_c with an angle of 120° between their symmetry axis and which are responsible for the graphene interlayer bonds. However, these new hybridized orbitals can be expressed as a linear combination of the original in-plane orbitals which will be used in this work[3].

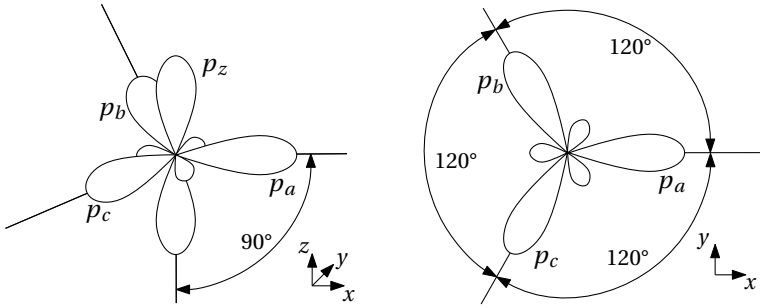

Figure 2.2: Schematic illustration of sp^2 hybridized orbitals. The newly created in-plane orbitals p_a, p_b, p_c are equivalent with an angle of 120° between their symmetry axis, p_z orbital is unchanged (still out of $x-y$ plane).

In the first approximation, only valence bands of the two inequivalent carbon atoms in the unit cell (denoted by A and B) can be considered in the band structure calculation. Due to 2×4 orbitals provided by both atoms, there will be 8 distinct Bloch waves in the crystal giving rise to 8 electron bands. Two electronic bands stem purely from p_z orbitals due to their orthogonality to in-plane orbitals and are named π and π^*, for bonding and anti-bonding combination of the orbitals respectively. The in-plane orbitals give a rise to the other 6 electronic bands, 3 bonding σ and 3 anti-bonding σ^*,

[3] For more details see Ref. [35].

which are the focus of this thesis. The energy of the anti-bonding states σ^* and π^* is higher than the energy of the bonding states and for perfect ML graphene lays above Fermi level. Hence, σ^* and π^* are referred to as unoccupied or conduction bands.

If a more realistic model is used, for example by including d, more bands are present above E_F and the original states stemming from the valence orbitals are modified. Figure 2.3 shows an example of an existing electron band calculation taken from Ref. [52]. The results are calculated from first principles and using a TB model. Figure 2.3a) visu-

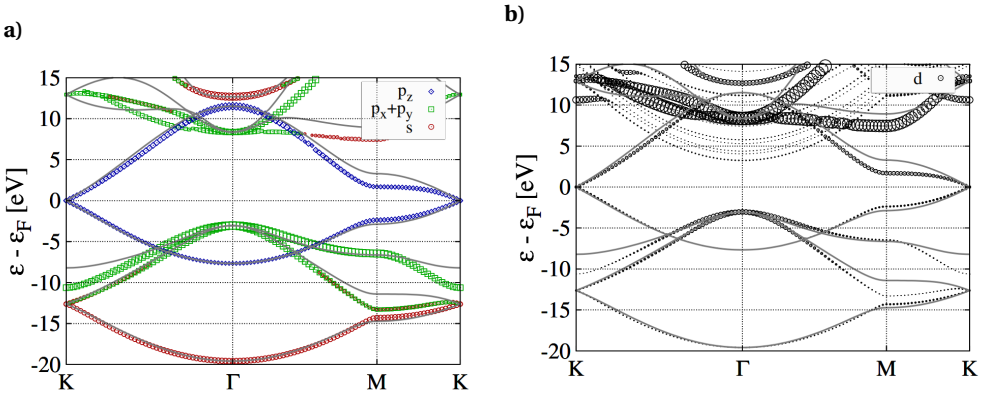

Figure 2.3: Graphene band structure. Panel 2.3a) shows electronic bands with an origin in s (red), $p_x + p_y$ (green) and p_z (blue) orbitals, panel 2.3b) shows a contribution to electronic bands from d orbitals (black). Solid lines are results of TB model.

alizes contributions of valence orbitals to the corresponding bands. The two π and π^* bands (denoted in blue) meet at the Fermi level (here denoted by ϵ_F) at K where they create the so called Dirac cone, which has been of main interest due its direct connection to graphene's electronic properties. The three σ bands are present below the Fermi level (denoted in red and green according to their origin). The σ^* bands are present at much higher energies with the minimum around 8 eV at Γ. The results of the TB model are shown by grey solid lines. Figure 2.3b) shows a contribution to the band structure caused by d orbitals. The new free-electron like bands should be present from approximately 3.5 eV above the Fermi level at Γ and as presented in Ref. [34], they develop a continuum of states.

Moreover, if an environment is included (e.g. by including the surface), more exotic states, such as image potential states can be expected (see the next section). In addition once electron interactions and lattice dynamics are included the band structure can be even further significantly modified, for instance by an electron-phonon coupling as mentioned previously and which is discussed in section 2.1.5 and 2.1.6.

2.1.4 Image Potential States

If an electron is in the vicinity of a conductive surface (metal, graphene/graphite), the electronic field is screened which can be seen as an image potential on the other side of the surface (see figure 2.4a)). As a result the electron feels a Coulomb-like attractive potential. However, if there are no available states below the vacuum level E_v where the electron can escape to the surface, it is trapped in the potential and quantized image potential states are created. The system can be seen as one-dimensional (1D) and develops a Rydberg-like series of image potential states [53]. For graphene on a metal-

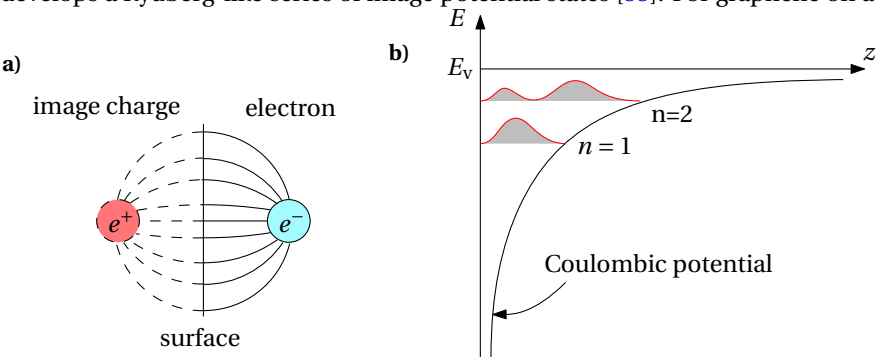

Figure 2.4: Schematic illustration of image potential states. Panel a) shows an electron in vicinity of a conductive surface (graphene). The screening due to the surface can be seen as an image potential created on the other side. Panel b) shows an Coulomb-like potential created near the surface. If there are no available states in the material below the vacuum level E_v, quantized image potential states are created. Probability amplitude (red line) of the first two image potential states (denoted by $n = 1, 2$) is shown.

lic surface, the image potential states have already been observed [54]. For graphene which is on a non-interacting substrate (SiC), two different Rydberg-like series [37], denoted by superscript + and − were predicted [37] and already experimentally reported [55, 56], but questioned by Ref. [34] as mentioned before.

2.1.5 Phonons in Two-dimensional Materials

Similarly to energy quanta assigned to electromagnetic field - photons, the energy quanta of collective lattice vibrations were assigned to phonons.

Due to the thermal energy and quantum mechanical effects, atoms in crystals are not steady but oscillate around their equilibrium position. In the simplest model in Born-Oppenheimer approximation, atomic nuclei are separated from the electronic states and the restoring force is approximated by a harmonic model (e.g. the restoring force is quadratic in the displacement). Considering a system of such interconnected oscillators, an investigation of the propagation of elastic waves through the crystal characterized by two quantum numbers, $\boldsymbol{q}$, the wave vector and ν, mode (branch) quantum

number, can be done. The energy quantum of such propagating waves (collective oscillations) is called phonon. There exists $3j$ phonon modes for j atoms in the primitive cell[4]. For graphene-like systems with two atoms in the primitive cell, there are 6 different modes depicted in the figure 2.5, 3 acoustic modes, where nuclei in the unit cell oscillate in phase and 3 optical modes where the nuclei oscillate out of phase[5]. The motion of nuclei can either be longitudinal with respect to the propagating wave (LA and LO modes for acoustic and optical phonons respectively), transversal in-plane (TA and TO modes) or transversal out-of-plane (ZA and ZO modes). The main difference between the acoustic and optical phonons is that the frequency of acoustic phonons goes to zero with increasing wavelength, whereas optical phonons have non-zero frequency. Figure 2.6 shows phonon dispersion for both graphene (2.6a)) and graphite (2.6b)) based on ab initio calculations (solid lines) and experiments (circles). Both graphs are almost identical due to weak interlayer coupling between graphitic layers. If a strong coupling between the layers is included, out-of-plane oscillations are effected and ZA and ZO dispersions are modified. In this situation, frequency of ZA mode does not tend to zero for long wavelengths, but has finite frequency [58].

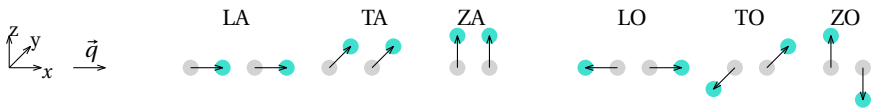

Figure 2.5: Schematic illustration of phonon modes using two atoms from the unit cell. The excited wave with wave vector $\boldsymbol{q}$ propagates in the direction of x-axis. The graphene sheet is located in the x-y plane. From left to right: Longitudinal acoustic (LA) mode, in-plane traversal acoustic (TA) mode, out-of-plane transversal acoustic (ZA) mode, longitudinal optical (LO) mode, in-plane transversal optical (TO) mode and out-of-plane transversal optical (ZA) mode. Figure is inspired by Ref. [59].

Unlike electrons, phonons obey Bose-Einstein statistics

$$n_{\boldsymbol{q}\nu}(E_{\boldsymbol{q}\nu}) = \frac{1}{e^{\frac{E_{\boldsymbol{q}\nu}}{k_B T}} - 1}, \tag{2.5}$$

where $n_{\boldsymbol{q}\nu}$ is a number of particles in state $\boldsymbol{q}$, ν, $E_{\boldsymbol{q}\nu} = \hbar\omega_{\boldsymbol{q}\nu}$ is the energy of corresponding state with frequency $\omega_{\boldsymbol{q}\nu}$, k_B is Boltzmann constant and where T denotes temperature.

[4] See for example textbooks from Kittel [57, 50].

[5] Movement of nuclei in acoustic modes resembles sound propagation in air/water, whereas optical modes can be excited by infrared radiation (for example in NaCl) and hence the corresponding names are used.

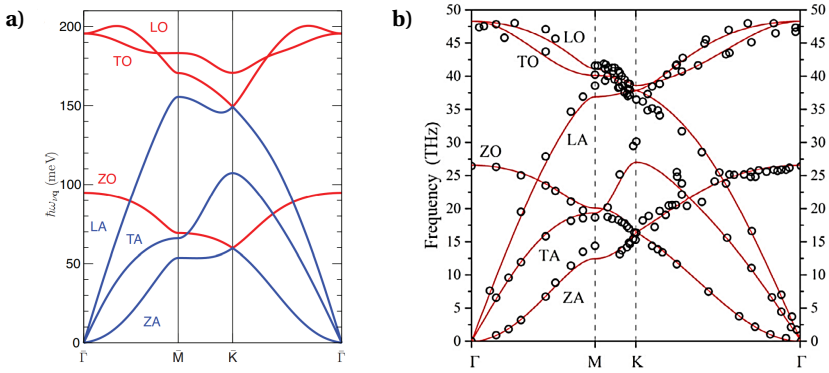

Figure 2.6: Phonon dispersion for **a)** graphene and **b)** graphite. Due to weak coupling between the graphitic layers, phonon dispersions are almost identical (200 meV corresponds to 48.36 THz). Solid lines show ab initio calculations while circles denote experimental data. Figures are adopted from Ref. [29] and Ref. [59] respectively.

2.1.6 Electron-phonon Interactions

In the presence of phonons, the electron with momentum $\boldsymbol{k}$ can be scattered by either emission or absorption of the phonon with momentum $\boldsymbol{q}$ which is schematically shown in the figure 2.7. As a consequence, both electron energy and momentum are changed

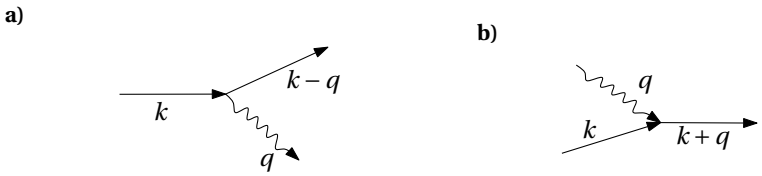

Figure 2.7: Electron scattering by phonons. Phonon emission and phonon absorption are shown in the panel a) and b), respectively.

which can be directly observed in experiments and which effects transport properties of the material. Here, the focus is not graphene's properties, but rather on effects of electron-phonon coupling on the band structure.

One of the striking examples is strong electron-phonon coupling at the top of the highest occupied σ bands. TO phonon mode couples to electrons which results in a kink at the top of the band instead of a parabolic shape of the band. This is depicted in the figure 2.8. The kink is clearly visible in both the 1BZ (2.8a)) and the 2BZ (2.8b)) at energy range around 200 meV which corresponds to the energy of the TO phonon. Both spectra were taken by angle-resolved photoemission spectroscopy (ARPES). The variation and consequent suppression of intensity at the top of the band is caused by the experimental technique, not by a difference of the structure in the 1BZ and the 2BZ.

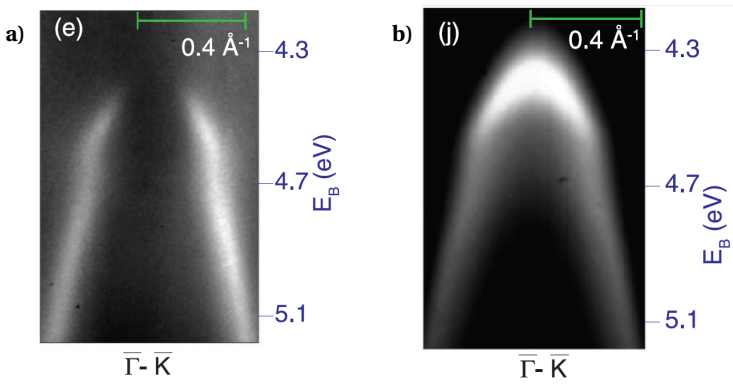

Figure 2.8: Kink observed at the top of the highest occupied σ bands in graphene. Panel a) shows the kink observed by angle-resolved photoemission spectroscopy measured in the 1BZ, panel a) shows the same king measured in the 2BZ. The kink is observed at approximately 200 meV from the top of the band which corresponds to the energy of the optical phonon. The differences in intensity between 1BZ adn 2BZ and consequent suppression of intensity at the top of the σ in the 1BZ stems from angle-resolved photoemission spectroscopy. Adopted from Ref. [29].

In the unoccupied bands, similar kinks should be expected and should therefore be included in the simulations. Recently, a symmetry analysis of electron-phonon coupling in graphite showed that electrons present in the σ^* bands can couple to both LO and TO optical and LA and TA acoustic phonons [45]. Moreover, the same work showed that the electron-phonon is actually present in the unoccupied bands. Due to the in-plane origin of the σ^*, the bands cannot be expect to be highly effected by layer stacking[6] and so similar coupling should be also expected in Graphene.

2.2 A Short Overview Of Experimental Methods

In order to check the validity of theoretical predictions and calculations, experimental techniques have to be utilized. In the 2D materials, surface sensitive techniques have to be used in order to check both the quality of the materials and to investigate their physical properties. The first section presents a short discussion about techniques for band structure investigation with a main focus on unoccupied states. In the second section a brief discussion about possible surface quality investigation techniques is presented.

[6] This was shown by Ref. [28] where the same coupling was also observed in the unoccupied σ bands in graphene.

2.2.1 Techniques for Band Structure Investigation

After the recognition and explanation of the photoelectric effect and consequent development of quantum physics, a strong focus was put on occupied states of materials, especially related to semiconductor technology. Many different spectroscopic techniques were developed. However, none of them are as universal for surface related studies as photo-emission spectroscopy (PES)[7]. The technique direct uses the photoelectric effect. In other words, light is incident on a material, where the energy is transferred to electrons. If the energy is high enough, electrons can escape the material and their energy is measured. Moreover, due to the conservation of momentum parallel to the surface[8], angle-resolved photoemission spectroscopy (ARPES) can be used to map complete band structure in $\boldsymbol{k}$-E space. PES is depicted in the figure 2.9a).

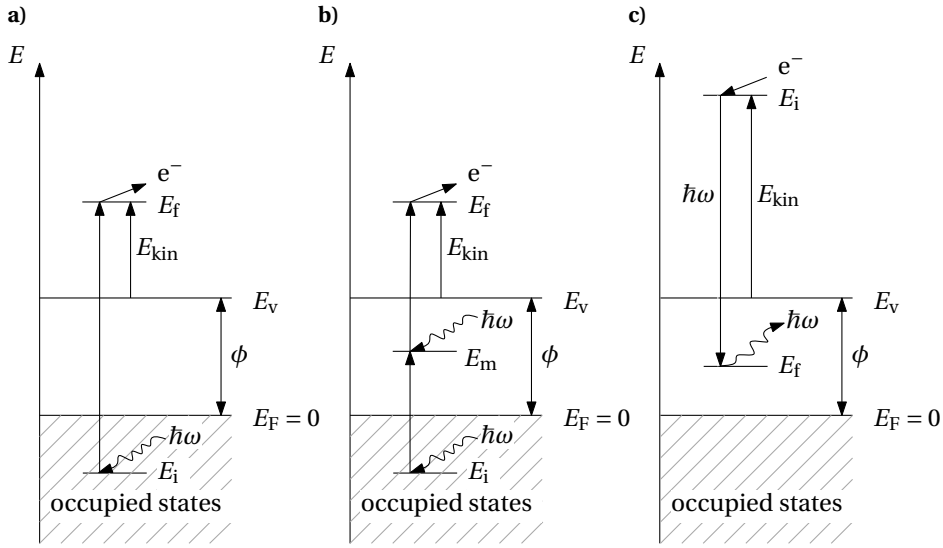

Figure 2.9: Comparison of different spectroscopic techniques. Panel **a)** shows PES, where en electron is excited by a photon of energy $\hbar\omega$ from its initial state with energy E_i to a final state with E_f where it eventually escapes the surface. $E_F = 0$ stands zero energy at Fermi level, E_v is the vacuum level, ϕ the work function and E_{kin} is the kinetic energy of electrons. Panel **b)** shows the principle of 2PPES, direct transition from initial to final state is replaced by two-photon excitation through and intermediate state with energy E_m situated between Fermi energy E_F and vacuum energy E_v. Panel **c)** then shows principle of IPES where an electron from initial state makes transition to final state in a conduction band. During this process radiation can be created.

[7] The original PES was used in X-ray region to investigate atomic binding energies [60].

[8] One rather intuitive explanation why the perpendicular momentum is not preserved is that the escaping electron feels an attractive force to the surface so its momentum $\boldsymbol{k}_\perp$ is therefore changed, however, components parallel to the surface cancel out and hence $\boldsymbol{k}_\parallel$ is preserved.

In the unoccupied bands, ARPES can still be used [61, 62]. However, this requires knowledge of initial states and therefore the analysis is not straight forward. In addition, energy levels below vacuum level E_v cannot be measured. To overcome the problem a modification of ARPES was developed: two-photon photo-emission spectroscopy (2PPES) [63]. This method utilizes two-photon excitation of an electron to introduce an intermediate state in the unoccupied band below the vacuum level which is depicted in the figure 2.9b). Due to the possibility of tunable time delay between the excitations, dynamics of the states can also be studied[64]. The main drawbacks of the technique are a limitation to states with sufficiently long lifetime below the vacuum level[9], a need for femtosecond laser technology to control the excitation process and a need for a special low-energy electron detector[66].

Common alternatives to 2PPES are inverse photo-emission spectroscopy and its $\boldsymbol{k}$-resolved version (KRIPES)[67]. An inverse process to PES is utilized where an electron beam is incident to a material and radiation is produced[10]. Knowing the angle of incident electrons, their energy, and energy of outgoing photons, the unoccupied part of a band structure can be determined. Energy diagram for IPES is shown in the figure 2.9c). Unlike in ARPES, achieving a good resolution in KRIPES experiments is difficult and is typically between 350 and 700 meV, which is more than an orders of magnitude worse than in ARPES experiments. In addition, the scattering cross-section for inverse photoemission is about five order of magnitude lower than for "forward" photoemission, which causes the count rates to be extremely small [67] and requires long acquisition times. An advantage of KRIPES is then the possibility to map the whole unoccupied band directly from Fermi level. Due to the similarity to PES, the same theory can be used with slight modifications[11]. The short mean free path of low-energy electrons in materials (~10 Å) in then responsible for the surface sensitiveness of the technique [68].

In order to overcome small count rates in IPES, several other methods has been developed such as total current spectroscopy (TCS) [69, 70] and very-low-energy electron diffraction (VLEED) [71], which are based on absorption and reflectivity of low-energy electrons respectively. Recently, a new method based on low-energy electron microscopy (LEEM) was presented in Ref. [72] with spatial resolution better than 20 nm which is far superior to all previously mentioned techniques[12]. In comparison to IPES, however, neither TCS, VLEED nor LEEM can measure energies below the vacuum level.

[9] One of the main applications of the technique is an investigation of image-potential states in various metals, see for example Ref. [65]

[10] The radiation is known as "bremsstrahlung" - braking radiation. In the early development of IPES, the technique was called bremsstrahlung spectroscopy and the name is still in use for higher electron energies

[11] For practical purposes and application in solids, processes involved in PES and IPES are just time reversals of each other [67].

[12] For IPES and other measurement techniques where low-electron beam is utilized the typical electron beam spot size on the sample is 1-3 mm.

For this reason and due to the availability of IPES at the home institute, IPES was chosen for the experiments.

2.2.2 Methods to Investigate Surface Quality

Before the actual measurement of the band structure can be performed, the surface quality has to be checked. This can be done in many different ways and at many different scales. The investigation on the atomic level [13] is however not very suitable for IPES measurements due to a relatively large electron beam spot size used in the experiment. Moreover, the sample has to be kept in ultra high vacuum (UHV) to prevent it from being contaminated, which means that the instrument has to be present in the chamber.

The most commonly used technique is low-energy electron diffraction (LEED) [73] which is schematically shown in the figure 2.10. Incident electrons with energies between 20 and 200 eV are diffracted due to the atomic structure of the sample and maxima of intensity are created at certain angles γ. Due to a short mean free path of the low-energy electrons used in LEED (~ 10 Å), the technique is surface sensitive. LEED has the advantage of providing a real-time image.

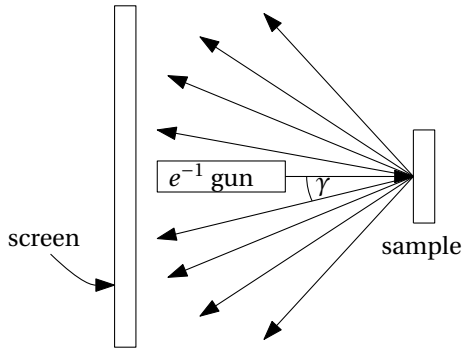

Figure 2.10: Schematic picture of low-energy electron diffraction. Incident electrons are diffracted due atoms in the sample and due to constructive interference, create maxima of intensity at certain angles γ.

Alternatively, the surface quality can be checked by a comparison of results obtained by other surface sensitive techniques which shows a typical future of the material. An example is a ARPES measurement of graphene on SiC [74] which shows a very sharp and distinct Dirac cone around K. Due to a bulk band gap of SiC from the ermi level to approximately 2 eV below the Fermi level, graphene quality and quality of the surface can be judged from the energy broadening of the graphene state within the SiC ban gap.

[13] For example using scanning tunnelling microscopy or atomic force microscopy.

2.3 Inverse Photoemision Spectroscopy

The concept of IPES was already introduced in the previous section, however, a deeper discussion is needed. This section introduces basic principles and apparatus construction rather than an exhausting theoretical description. It should provide the reader with motivation for the following, more theoretical computational chapter and an understanding of the structure of this thesis.

2.3.1 Basic Theory

Figure 2.11 shows a schematic picture of IPES system. Electrons are incident with an angle θ with respect to the sample surface normal, where photons are emitted from with an angle α. Due to the energy conservation and the conservation of momentum parallel to the surface, the intensity can be expressed as

$$I(E,\boldsymbol{K}_\parallel) \propto \left(D_{\text{tot}}(E) * A_{\text{beam}}(\boldsymbol{K}_\parallel)\right) * \left(c_{\text{i}}|M_{\text{fi}}|^2 \times A^+(E,\boldsymbol{K}_\parallel)\right), \tag{2.6}$$

as is derived later in section 3.3. $\boldsymbol{K}_\parallel$ denotes a momentum of the incident electrons parallel to the sample surface and can be determined from its kinetic energy and known angle of incidence . $D_{\text{tot}}(E) * A_{\text{beam}}(\boldsymbol{K}_\parallel)$ is a convolution between the total energy resolution function and a momentum spread function respectively. This pre-factor accounts for the broadening due the measuring apparatus itself. The second term in round brackets, $\left(c_{\text{i}}|M_{\text{fi}}|^2 \times A^+(E,\boldsymbol{K}_\parallel)\right)$, stands for the actual emitted intensity during IPES measurement. c_{i} is a coupling between incident electrons and the initial electronic state, M_{fi} are the so called matrix elements and are a measure of the probability of electron transition from the initial state (i) to the final state (f) with a photon being emitted, and where $A^+(E,\boldsymbol{K}_\parallel)$ is a spectral function, in which the many-body interactions are reflected. Due to low energy electrons, the whole apparatus has to be placed in ultra height vacuum (UHV).

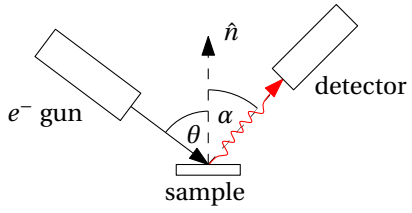

Figure 2.11: Schematic illustration of IPES system. Electrons are emitted from the electron fun and incident to the sample with an angle θ. Emitted photons (red curly arrow) are collected at the detector with angle α from the surface normal. Due to low energy electrons, the whole apparatus has to be placed in ultra height vacuum (UHV).

2.3.2 Working Modes

Recalling the energy diagram for the IPES (figure 2.9c)), energy conservation can be written as

$$E_f = \phi + E_{kin} - \hbar\omega, \tag{2.7}$$

where again, ϕ is the material work function. Since ϕ is related to measured material and is fixed, the final energy state E_f can be scanned either by varying kinetic energy E_{kin} of the incident electron or by varying photon detection energy $\hbar\omega$. The so called isochromat mode utilizes tunable E_{kin} while keeping $\hbar\omega$ fixed, whereas the so called tunable photon energy (TPE) mode keeps E_{kin} fixed while $\hbar\omega$ is tuned. Both modes are schematically depicted in the figure 2.12.

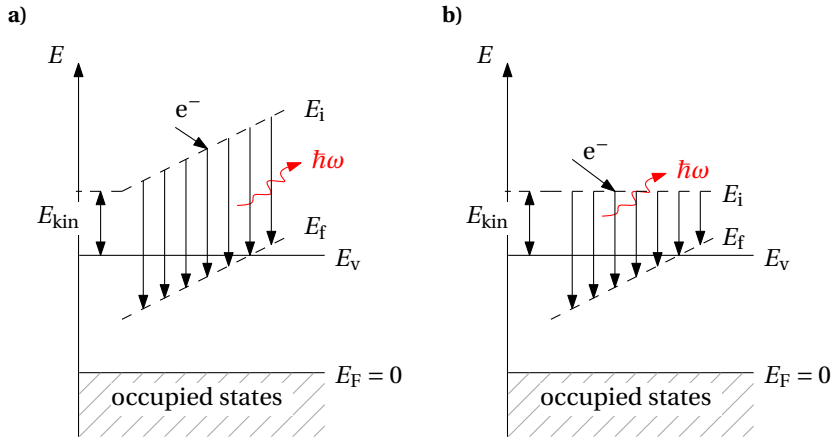

Figure 2.12: IPES working modes. Panel **a)** shows isochromat mode where a photon energy is fixed while the kinetic energy of the electron is varied. Panel **b)** shows tunable photon energy (TPE) mode where the kinetic energy of electron is kept constant while the photon energy is varied.

Even though both modes allow mapping of the energy of final states, both provide different information. In TPE mode, both $\boldsymbol{k}_\parallel$ and $\boldsymbol{k}_\perp$ are kept fixed for angle of incident electrons, moreover, effects of changing the initial electron states are eliminated[14] which presents a great advantage when analysing data. The big disadvantage is a low efficiency of the detector compared to isochromat mode. This will be further discussed in section 2.3.3. The change in electron energy and the corresponding change in $\boldsymbol{k}_\perp$ for fixed angle of the electron gun then allows the investigation of $\boldsymbol{k}_\perp$-dispersion of the energy bands which can be crucial for further band origin analysis [75].

[14] Remember the dependence of intensity on matrix elements - the transition probability between initial and final states.

2.3.3 Construction

Up to this point, working principles and working modes of IPES were discussed, however, the construction of the apparatus itself is missing to complete the picture. Here, a description of the main two components, an electron source and a photon detector (or a photon selector), is given.

Electron source: A good quality electron source is essential in order to achieve good IPES results, however, meeting all the formal requirements - low angular spread (to 5°), working range (5 - 20 eV), small focus spot (1-2 mm), reasonably high electron current, low energy spread - is not a trivial task [67]. Figure 2.13 shows the simplest functional design of the electron source known as the pervatron [76]. Electrons are produced by thermal emission at low-work-function BaO which gives a low energy spread. The electrons then pass through a slit in order to reduce angular divergence and are consequently focused and accelerated by a potential between cathode and anode and on the focal element respectively. Due to the simple design, this type of electron gun has already been commercialized and is also present at Ny-NALOS laboratory at NTNU.

During the history of IPES development, different attempts were made in order to improve the performance of the electron source. A design based on four lenses has been reported [77] and successfully used [78]. The beam energy spread and divergence can be further improved by different types of deflectors or more complex electron optics. Moreover, unlike PES, the implementation of spin-resolved measurements does not lower the count rates and can be easily achieved by illuminating GaAs by a circularly polarized laser light [79, 80].

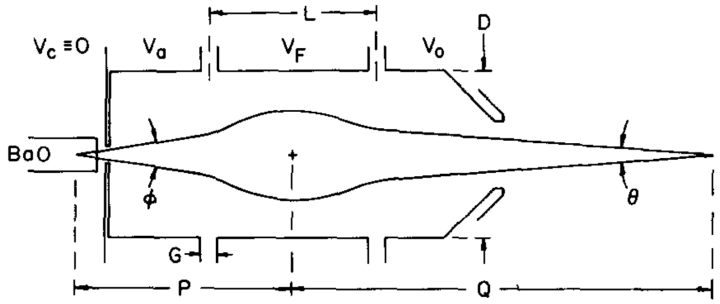

Figure 2.13: A schematic of an electron gun known as the pervatron. Electrons are thermally emitted by a low-temperature emitter (BaO), pass through a pin hole (which serves as a cathode and is kept at $V_c \equiv 0$), and are accelerated by a voltage applied on anode (V_a). The focus can be changed by modifying the focus voltage V_F. Picture adapted from Ref. [76].

The electron source available at NTNU was produce by PSP Vacuum Technology. Its construction corresponds to the pervatron previously described. The emission cathode is made of BaO. The fact manual is available from Ref. [81].

Photon detection: In order to resolve IPES in energy, not all the outgoing photons can be measured, but rather a specific energy has to be selected. This can be achieved by using three different methods - band-pass detectors, grating spectrographs and refracting monochromators (see figure 2.14 for a description of experimental arrangement).

The first method for filtering specific energies is the band-pass filter. The band-pass filter consists of two main consist of two main parts - a window, which serves as a low-pass filter (typically CaF_2), and a photon detector which is a high-pass filter. For the detector, either a Geiger-Müller (GM) counter or a solid-state detector can be used.

The GM counter consists of a hollow tube with a rod in the middle which is held at a fixed potential. The whole tube is filled with a gas (typically I_2) which is ionized by the incoming light. Due to the potential, the ions which are created are transported to electrodes and a current can be measured. In figure 2.15a) both the ionization probability of I_2 and a transmission probability of the CaF_2 window are shown as a function of energy of the incoming photons.

The typical solid-state detector consists of a photocathode (made of, for example, NaCl/KCl/Ta) which is hit by the incoming light to emit electrons which are detected by a photomultiplier [82]. This construction has the advantage of being fairly easy and "pluck and play" in comparison to GM counters. On the other hand, resolution is not optimal and the resolution function does not have a Gaussian shape [83]. The quantum detection efficiency (QDE) for different materials is shown in figure 2.15b).

The resolution of the band-pass detectors can be improved by reducing the width of the band-pass filter, either by moving the window transmission threshold to lower energies, or by moving the Inization probability/QDE thresshold to higher energies. The former can be done by a choice of window material or by changing the temperature of the windows [84, 85]. The latter can be achieved by changing the filling gas [86, 87] or by changing the material of the photocathode (see again figure 2.15b)). It is worth noting that there is a trade-off between improving the resolution and having reasonably high count rates. The count rates can be improved by placing the detector as close as possible to the sample in order to cover the widest possible solid angle.

The second method, grating spectrographs, utilise diffraction on a grid in order to separate photons of different energies. This approach offers offers the possibility of changing the photon energy (and hence work in TPE mode), but also reduces the count rates. The low count rates can be partly overcome using simultaneous collection of different energies, however this approach increase the cost and the complexity significantly. Moreover, the size of such a system is much bigger than for a band-pass detector.

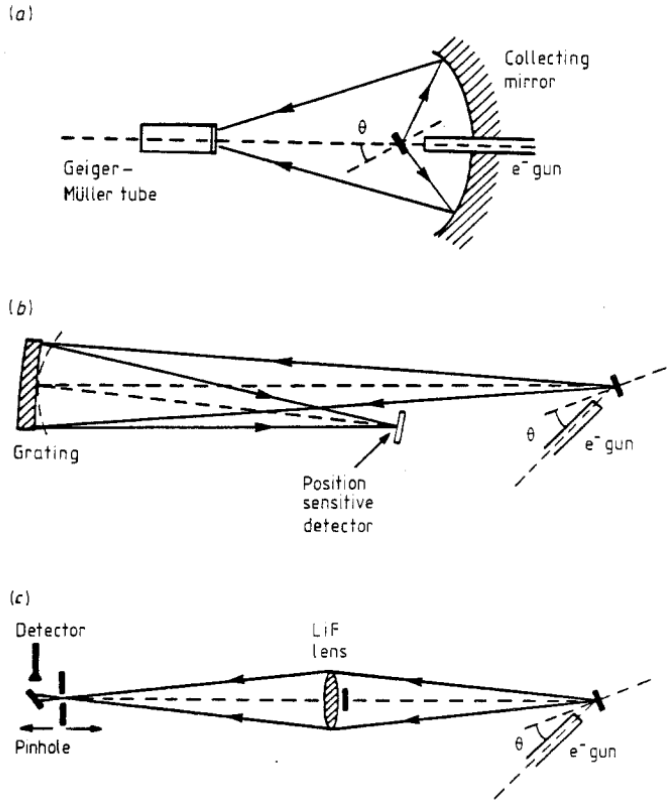

Figure 2.14: Schematic of the experimental arrangement for band-pass detectors, grating spectrographs and refracting monochromators (from top to bottom). Efficiency of a band-pass detector, here represented by a Geiger-Müller tube, can be increased by a collecting mirror which focuses photons emitted at the sample (black rectangle). The arrangement is often replaced by a detector as close as possible to the sample, leaving the mirror out. In the grating spectrograph, emitted photons are incident on a grating, which due to diffraction results in energy separation of incident photons. The last arrangement uses a lens to focus emitted photons. Due to energy dependence of the refraction index (and hence different focal lengths for different energies), different photon energies transmitted through the system can be chosen by a pin hole behind the lens. Figure is adopted from Ref. [67]

The last method to discuss is the refracting monochromator. Refracting monochromators utilize a lens (for example LiF) in order to focus outgoing photons from a big solid angle to a small area so that they can be collected by a single detector. Due to the properties of the lens, focal length for different light energies varies and can therefore be selected by a position of a pinhole with respect to the lens which is placed in front of the detector. This construction is somewhere between band-pass detectors and grating

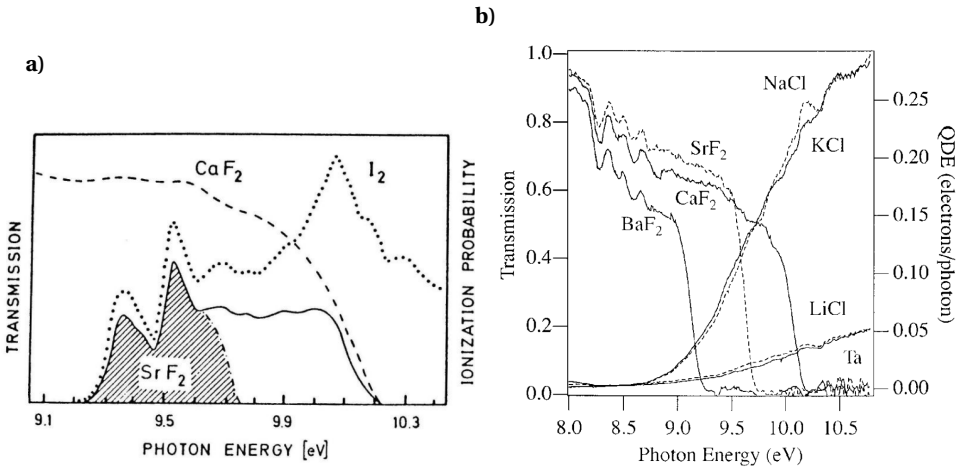

Figure 2.15: Characteristics of band-bass detectors. Panel a) shows transmission characteristics of CaF_2 and ionization characteristics of an I_2 filled Geiger-Müller counter which together make up the band pass filter(solid line). The resolution can be improved by using a SrF_2 window (transmission characteristics is shown in panel a)). In panel b) quantum detection efficiencies (QDE) of solid state detectors made of different materials are shown together with transmission probability of different windows. Adopted from Ref. [24] and Ref.[83]

spectrographs due to possible tunability of selected photon energy and possible wide angle of acceptance. Both the previously mentioned methods suffers from a finite electron beam spot size.

The detector available at NTNU is a solid state NaCl coated Ta detector based with a CaF_2 window [81].

Chapter 3

Theory and Computational Approach for IPES Spectrum Simulations

This chapter presents three main sub-steps which are needed in order to simulate the IPES spectrum. The aim of this chapter is to introduce a general background for a computational approach together with its limitations. In the first section, band structure calculations focused on the graphene TB model are presented. Many-body effects are introduced in the second section with a focus on electron-phonon coupling. The last section revises and extends IPES theory in order to provide the necessary knowledge of matrix element calculation.

3.1 Band Structure Calclations

After the introduction of the Schrödinger equation, it was quickly realized that an exact solution was available for very simple toy-models. In the first attempts to electronic band calculations in solids, approximate methods had to be introduced. One of the first methods was as a linear combination of atomic orbitals (LCAO) [88] or a Bloch method [89]. This method was later revised [90] and is today known as the tight binding model. Later, methods utilizing electron density rather than separated wave functions, known as density functional theory (DFT) theory [91] and many other methods were introduced. However, none of them offers such simplicity nor deep insight as the TB model. Moreover, the TB method is easily implemented and can provide a tool for further calculations related to spectroscopic methods [28, 29, 92]. It is therefore used in this work as a first approximation.

In the first section, a simple 1D TB model is introduced. Subsequently, a description of periodic systems using Bloch and Wannier states and localized atomic orbitals is given in the second section. In the third section, the secular equation is introduced. This allows the eigenstates and the energy eigenvalues of the system to be determined. Finally, the forth section presents the TB model for graphene followed by the fifth section, which presents the results of the TB calculation.

3.1.1 Tight-Binding Model

For a simple introduction to the TB model, 1D example with a periodic potential $U(x)$ is considered (see figure 3.1). This potential can be created for instance by a periodic lattice of atoms. If a particle (an electron) is placed in the potential with energy lower than the potential height, its wave function (marked red) will be localized near the atomic centres (potential minima) and will decay rapidly with increasing distance from the centre. Therefore, the electron will have just a small probability to tunnel from a position j to $j+1$ or $j-1$ and even smaller probability to tunnel to $j+2$ and $j-2$ and so on. If just the former is considered and later neglected, one talks about nearest neighbour hopping and the Hamilton's operator has the following form

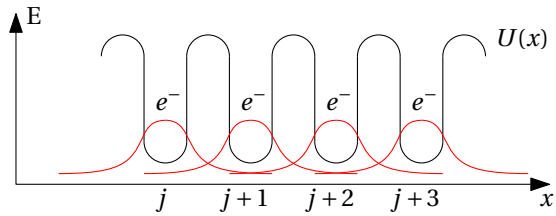

Figure 3.1: A simple schematic of one-dimensional TB model. The electrons are trapped in the periodic potential $U(x)$ and the wave function (marked red) are almost localized at positions $j, j+1, \ldots$. The strong localization of the wave functions causes the overlap between the two neighbouring wave functions to be small and so is the probability of jumping from position j to $j+1$ and vice versa.

$$\mathscr{H} = -t\sum_{j}(c_j^{\dagger}c_{j+1} + c_{j+1}^{\dagger}c_j), \tag{3.1}$$

where $c_j^{\dagger}$ and c_j are creation and annihilation operators at site j and t is hopping integral which will be discussed later[1]. It is worth noting that TB model described above treats the system as being build out of potential wells which were brought together with the original wave functions unchanged, in other words, tight-bound to the original potential well (or an atom). The solution is hence not an exact solution.

[1] One can think about the hopping as a two step process. First, electron is annihilated at site j and then a new electron i created at $j+1$ and vice versa for the hermitian conjugated term. The probability of "hopping" is then related to t.

3.1.2 Construction of Bloch Waves

The Bloch waves were already introduce in the section 2.1.2 but no information how they can be contracted was mentioned. One can try to construct the Bloch state as a Bloch sum over the atomic orbitals $\psi_{\mu\boldsymbol{k}}(\boldsymbol{r}) = \sum_R e^{i\boldsymbol{k}\cdot\boldsymbol{R}}\chi_{\mu\boldsymbol{k}}(\boldsymbol{r}-\boldsymbol{R})$ positioned at lattice sites $\boldsymbol{r}$, however the result is a set of non-orthogonal functions as discussed in [90] and [93]. This problem was later approached and solved by Wannier [94] by introducing so called Wannier wave functions

$$w_{\mu\boldsymbol{R}}(\boldsymbol{r}) = \frac{1}{\sqrt{N}}\sum_{\boldsymbol{k}\in BZ} e^{-i\boldsymbol{k}\cdot\boldsymbol{R}}\psi_{\mu\boldsymbol{k}}(\boldsymbol{r}), \tag{3.2}$$

where N is the number of lattice sites and the summation goes through the entire Brillouin zone. It is worth noting that while Bloch states were highly delocalized, Wannier states are localized around $\boldsymbol{R}$ similarly to atomic centres, which offers better physical interpretation.

Once Wannier states are defined, one can express the Bloch state as an inverse Fourier transform of Wannier states

$$\psi_{\mu\boldsymbol{k}}(\boldsymbol{r}) = \frac{1}{\sqrt{N}}\sum_{\boldsymbol{R}} e^{i\boldsymbol{k}\cdot\boldsymbol{R}} w_{\mu\boldsymbol{R}}(\boldsymbol{r}). \tag{3.3}$$

Having defined Wannier functions one can calculate the value of the hopping parameter $t = -\int \mathrm{d}x^3\, w^*_{\mu\boldsymbol{R}}(\boldsymbol{r})\left(\frac{-\hbar\nabla^2}{2m} + U(\boldsymbol{r})\right) w_{\mu\boldsymbol{R}+\boldsymbol{a}}(\boldsymbol{r})$. The term $\left(\frac{-\hbar\nabla^2}{2m} + U(\boldsymbol{r})\right)$ is nothing but Hamilton's operator for a single particle in the potential $U(\boldsymbol{r})$ and $\boldsymbol{a}$ is the lattice vector.

The difficult task is then to determine the Wannier states. For most of the system the calculation cannot be done analytically, but first principle calculations are required. For our purposes, one can approximate the Wannier states by a linear combination of atomic orbitals [2] and the Bloch states are of the form

$$\psi_{\mu\boldsymbol{k}}(\boldsymbol{r}) \approx \frac{1}{\sqrt{N}}\sum_{\boldsymbol{R}} e^{i\boldsymbol{k}\cdot\boldsymbol{R}}\sum_{\boldsymbol{R}_\mathrm{j}}\sum_{nlm} c_{\mu,\boldsymbol{R}_j nlm}(\boldsymbol{k})\chi_{\mu,\boldsymbol{R}_j nlm}(\boldsymbol{r}-\boldsymbol{R}), \tag{3.4}$$

where $\chi_{\mu,\boldsymbol{R}_j nlm}(\boldsymbol{r}-\boldsymbol{R})$ are the atomic orbitals centred at position $\boldsymbol{R}_\mathrm{j}$ within the unit cell[3], $c_{\mu,\boldsymbol{R}_j nlm}(\boldsymbol{k})$ coefficients to be determined and n, l, m are principal, azimuthal and magnetic quantum numbers respectively. The atomic wave functions are then defined as

$$\chi_{\boldsymbol{R}_j nlm}(\boldsymbol{r}) \equiv \langle \boldsymbol{r}|nlm\rangle = R_{nl}(r)\langle \boldsymbol{r}|lm\rangle = R_{nl}(r)\,Y_l^m(\theta,\varphi), \tag{3.5}$$

[2] Note that the orthogonality is then preserved as discuss in [90].

[3] For graphene-like system with two atoms in the basis, $j = A, B$ and corresponding to two positions $\boldsymbol{R}_\mathrm{A}$ and $\boldsymbol{R}_\mathrm{A}$ of atoms A and B, respectively.

where the band index μ and position index $\boldsymbol{R}_j$ were dropped for convenience. $R_{nl}(r)$ and $Y_l^m(\theta,\varphi)$ are respectively radial and angular parts of the wave function with $Y_l^m(\theta,\varphi)$ also known as spherical harmonics. In physical chemistry, real combinations of atomic orbitals are used and are then commonly known as s, p, d, f,... orbitals are denoted by index ν. The Bloch state (3.4) then becomes

$$\psi_{\mu\boldsymbol{k}}(\boldsymbol{r}) = \frac{1}{\sqrt{N}} \sum_{\boldsymbol{R}} \mathrm{e}^{i\boldsymbol{k}\cdot\boldsymbol{R}} \sum_{\boldsymbol{R}_\mathrm{j}} \sum_{\nu} c_{\mu,\boldsymbol{R}_\mathrm{j}\nu}(\boldsymbol{k}) \chi_{\mu,\boldsymbol{R}_j\nu}(\boldsymbol{r}-\boldsymbol{R}), \tag{3.6}$$

or in the Dirac notation

$$\langle \boldsymbol{r}|\psi_{\mu\boldsymbol{k}}\rangle = \frac{1}{\sqrt{N}} \sum_{\boldsymbol{R}} \mathrm{e}^{i\boldsymbol{k}\cdot\boldsymbol{R}} \sum_{\boldsymbol{R}_\mathrm{j}} \sum_{\nu} c_{\mu,\boldsymbol{R}_\mathrm{j}\nu}(\boldsymbol{k}) \langle \boldsymbol{r}|\boldsymbol{R}+\boldsymbol{R}_\mathrm{j},\nu\rangle. \tag{3.7}$$

Once the Hamilton operator and its eigenstates are found, the eigenvalues of the system - the required electronic bands can be calculated. This is the content of the next section.

3.1.3 Secular Equation

Knowing the basis and Hamiltonian $\mathscr{H}$ of the system, the single-particle Schrödinger equation can be used to determine the energy eigenstates $\mathscr{E}_\mu$ of the system.

$$\langle \psi_{\mu\boldsymbol{k}}|\mathscr{H}|\psi_{\mu\boldsymbol{k}}\rangle = \mathscr{E}_\mu \langle \psi_{\mu\boldsymbol{k}}|\psi_{\mu\boldsymbol{k}}\rangle \tag{3.8}$$

Substituting for the Bloch states and eliminating the energy eigenstates one gets

$$\mathscr{E}_\mu(\boldsymbol{k}) = \frac{\langle \psi_{\mu\boldsymbol{k}}|\mathscr{H}|\psi_{\mu\boldsymbol{k}}\rangle}{\langle \psi_{\mu\boldsymbol{k}}|\psi_{\mu\boldsymbol{k}}\rangle} = \frac{\sum_{\boldsymbol{R}_\mathrm{j}\boldsymbol{R}'_\mathrm{j}} \sum_{\nu\nu'} c^*_{\mu,\boldsymbol{R}_\mathrm{j}\nu}(\boldsymbol{k}) c_{\mu,\boldsymbol{R}'_\mathrm{j}\nu'}(\boldsymbol{k}) \langle \phi_{\nu\boldsymbol{k},\boldsymbol{R}_\mathrm{j}}|\mathscr{H}|\phi_{\nu'\boldsymbol{k},\boldsymbol{R}'_\mathrm{j}}\rangle}{\sum_{\boldsymbol{R}_\mathrm{j}\boldsymbol{R}'_\mathrm{j}} \sum_{\nu\nu'} c^*_{\mu,\boldsymbol{R}_\mathrm{j}\nu}(\boldsymbol{k}) c_{\mu,\boldsymbol{R}'_\mathrm{j}\nu'}(\boldsymbol{k}) \langle \phi_{\nu\boldsymbol{k},\boldsymbol{R}_\mathrm{j}}|\phi_{\nu'\boldsymbol{k},\boldsymbol{R}'_\mathrm{j}}\rangle}, \tag{3.9}$$

where

$$|\phi_{\nu\boldsymbol{k},\boldsymbol{R}_\mathrm{j}}\rangle = \frac{1}{\sqrt{N}} \sum_{\boldsymbol{R}} \mathrm{e}^{i\boldsymbol{k}\cdot\boldsymbol{R}} |\boldsymbol{R}+\boldsymbol{R}_\mathrm{j},\nu\rangle. \tag{3.10}$$

Terms $\langle \phi_{\nu\boldsymbol{k},\boldsymbol{R}_\mathrm{j}}|\mathscr{H}|\phi_{\nu'\boldsymbol{k},\boldsymbol{R}'_\mathrm{j}}\rangle$ and $\langle \phi_{\nu\boldsymbol{k},\boldsymbol{R}_\mathrm{j}}|\phi_{\nu'\boldsymbol{k},\boldsymbol{R}'_\mathrm{j}}\rangle$ are nothing but matrix elements $\mathscr{H}_{\boldsymbol{R}_\mathrm{j}\boldsymbol{R}'_\mathrm{j}\nu\nu'}$ and $\mathscr{S}_{\boldsymbol{R}_\mathrm{j}\boldsymbol{R}'_\mathrm{j}\nu\nu'}$ belonging to transfer and overlap integral matrices. For further convenience $\boldsymbol{k}$ will be omitted, but one should keep in mind the original ($\boldsymbol{k}$) dependence.

By differentiating $\mathscr{E}_\mu$ with respect to coefficients $c^*_{\mu,\boldsymbol{R}_\mathrm{j}\nu}$ and setting equal to zero one can find the local stationary point of $\mathscr{E}_\mu$ and hence the corresponding energy bands.

$$0 = \frac{\partial \mathscr{E}_\mu}{\partial c^*_{\mu,\boldsymbol{R}_j\nu}} = \frac{\sum_{\boldsymbol{R}'_j}\sum_{\nu'} c_{\mu,\boldsymbol{R}'_j\nu'}\mathscr{H}_{\boldsymbol{R}_j\boldsymbol{R}'_j\nu\nu'} \times \sum_{\boldsymbol{R}_j\boldsymbol{R}'_j}\sum_{\nu\nu} c^*_{\mu,\boldsymbol{R}_j\nu} c_{\mu,\boldsymbol{R}'_j\nu'}\mathscr{S}_{\boldsymbol{R}_j\boldsymbol{R}'_j\nu\nu'}}{\left(\sum_{\boldsymbol{R}_j\boldsymbol{R}'_j}\sum_{\nu\nu'} c^*_{\mu,\boldsymbol{R}_j\nu} c_{\mu,\boldsymbol{R}'_j\nu'}\mathscr{S}_{\boldsymbol{R}_j\boldsymbol{R}'_j\nu\nu'}\right)^2} - \frac{\sum_{\boldsymbol{R}_j\boldsymbol{R}'_j}\sum_{\nu\nu'} c^*_{\mu,\boldsymbol{R}_j\nu} c_{\mu,\boldsymbol{R}'_j\nu'}\mathscr{H}_{\boldsymbol{R}_j\boldsymbol{R}'_j\nu\nu'} \times \sum_{\boldsymbol{R}'_j}\sum_{\nu'} c_{\mu,\boldsymbol{R}'_j\nu'}\mathscr{S}_{\boldsymbol{R}_j\boldsymbol{R}'_j\nu\nu'}}{\left(\sum_{\boldsymbol{R}_j\boldsymbol{R}'_j}\sum_{\nu\nu} c^*_{\mu,\boldsymbol{R}_j\nu'} c_{\mu,\boldsymbol{R}'_j\nu'}\mathscr{S}_{\boldsymbol{R}_j\boldsymbol{R}'_j\nu\nu'}\right)^2} \tag{3.11}$$

$$0 = \sum_{\boldsymbol{R}'_j}\sum_{\nu'} c_{\mu,\boldsymbol{R}'_j\nu'}\mathscr{H}_{\boldsymbol{R}_j\boldsymbol{R}'_j\nu\nu'} - \frac{\sum_{\boldsymbol{R}_j\boldsymbol{R}'_j}\sum_{\nu\nu'} c^*_{\mu,\boldsymbol{R}_j\nu} c_{\mu,\boldsymbol{R}'_j\nu'}\mathscr{H}_{\boldsymbol{R}_j\boldsymbol{R}'_j\nu\nu'} \times \sum_{\boldsymbol{R}'_j}\sum_{\nu'} c_{\mu,\boldsymbol{R}'_j\nu'}\mathscr{S}_{\boldsymbol{R}_j\boldsymbol{R}'_j\nu\nu'}}{\sum_{\boldsymbol{R}_j\boldsymbol{R}'_j}\sum_{\nu\nu} c^*_{\mu,\boldsymbol{R}_j\nu'} c_{\mu,\boldsymbol{R}'_j\nu'}\mathscr{S}_{\boldsymbol{R}_j\boldsymbol{R}'_j\nu\nu'}} \tag{3.12}$$

And finally substituting from equation (3.9) in the second term we arrive to so called secular equation

$$\sum_{\boldsymbol{R}'_j}\sum_{\nu'}\left(\mathscr{H}_{\boldsymbol{R}_j\boldsymbol{R}'_j\nu\nu'} - \mathscr{E}_\mu\mathscr{S}_{\boldsymbol{R}_j\boldsymbol{R}'_j\nu\nu'}\right) c_{\mu,\boldsymbol{R}'_j\nu'} = 0, \tag{3.13}$$

or in the matrix for formalism

$$\left(\mathbb{H} - \mathscr{E}_\mu\mathbb{S}\right) c_\mu = 0, \tag{3.14}$$

where c_μ is a column vector with coefficients $c_{\mu,\boldsymbol{R}'_j\nu'}$. The only non-trivial solution to equation (3.14) is when determinant $\det\left[\mathbb{H} - \mathscr{E}_\mu\mathbb{S}\right] = 0$, which is a generalized eigenvalue problem[4]. It is good to keep in mind that $\mathbb{H}$, $\mathscr{E}_\mu$, $\mathbb{S}$ and c_μ are all $\boldsymbol{k}$-dependent. For the purposes of this thesis the problem is solved numerically using LAPACK [96] and the details will not be treated here. As one will see in the following sections, eigenvectors provide a tool to determine the intensity of the bands in the measurements.

3.1.4 Tight-Binding Model for Graphene

As discussed in the previous chapter, graphene can be described by a honeycomb lattice with two atoms in the unit cell. Atomic orbitals are sp^2 hybridized, which can be described by a linear combination of s, p_x, p_y and p_z orbitals. Due to the orthogonality of p_z to the other orbitals both within the atom and within the nearest neighbour, solutions can be separated. Here the focus is put on s, p_x, p_y orbitals which give rise to σ and σ^* bands in graphene. The subsequent derivation follows Ref. [35, 97].

[4] In other words, $\det\left[\mathbb{H} - \mathscr{E}_\mu\mathbb{S}\right]$ has to be singular. For further explanation and discussion one can see Ref [95].

Having 2 atoms in the unit cell (denoted A and B) and considering just s, p_x, p_y orbitals, both transfer and overlap integral matrices are 6×6 matrices. Indices we shortly abbreviated as $i = 1\cdots 6$, corresponding to s, p_x and p_y for atom A and B respectively. The matrices can be further decomposed into $3x3$ matrices and can be written as

$$\mathbb{H} = \begin{bmatrix} \mathscr{H}_{11} & \dots & \dots & \mathscr{H}_{16} \\ \vdots & \ddots & & \vdots \\ \vdots & & \ddots & \vdots \\ \mathscr{H}_{61} & \dots & \dots & \mathscr{H}_{66} \end{bmatrix} = \begin{bmatrix} \mathbb{H}_{AA} & \mathbb{H}_{AB} \\ \mathbb{H}_{BA} & \mathbb{H}_{BB}, \end{bmatrix} \tag{3.15}$$

$$\mathbb{S} = \begin{bmatrix} \mathscr{S}_{11} & \dots & \dots & \mathscr{S}_{16} \\ \vdots & \ddots & & \vdots \\ \vdots & & \ddots & \vdots \\ \mathscr{S}_{61} & \dots & \dots & \mathscr{S}_{66} \end{bmatrix} = \begin{bmatrix} \mathbb{S}_{AA} & \mathbb{S}_{AB} \\ \mathbb{S}_{BA} & \mathbb{S}_{BB}. \end{bmatrix} \tag{3.16}$$

From the definition of transfer matrix elements one can write

$$\begin{aligned} \mathscr{H}_{11} =& \langle \phi_{s\boldsymbol{k},\boldsymbol{R}_\mathrm{A}} | \mathscr{H} | \phi_{s\boldsymbol{k},\boldsymbol{R}_\mathrm{A}} \rangle \\ =& \frac{1}{N} \sum_{\boldsymbol{R},\boldsymbol{R}'} \mathrm{e}^{i\boldsymbol{k}\cdot(\boldsymbol{R}'-\boldsymbol{R})} \langle \boldsymbol{R}+\boldsymbol{R}_\mathrm{A}, s | \mathscr{H} | \boldsymbol{R}'+\boldsymbol{R}_\mathrm{A}, s \rangle \\ =& \frac{1}{N} \sum_{\boldsymbol{R}=\boldsymbol{R}'} \langle \boldsymbol{R}+\boldsymbol{R}_\mathrm{A}, s | \mathscr{H} | \boldsymbol{R}'+\boldsymbol{R}_\mathrm{A}, s \rangle \\ &+ \frac{1}{N} \sum_{\boldsymbol{R}=\boldsymbol{R}'\pm\boldsymbol{a}} \mathrm{e}^{\mp i\boldsymbol{k}\cdot\boldsymbol{a}} \langle \boldsymbol{R}+\boldsymbol{R}_\mathrm{A}, s | \mathscr{H} | \boldsymbol{R}'+\boldsymbol{R}_\mathrm{A}, s \rangle \\ &+ \frac{1}{N} \sum_{\boldsymbol{R}=\boldsymbol{R}'\pm 2\boldsymbol{a}} \dots \\ =& \frac{1}{N} \sum_{\boldsymbol{R},\boldsymbol{R}'} \epsilon_{2s} + \frac{1}{N} \sum_{\boldsymbol{R}=\boldsymbol{R}'\pm\boldsymbol{a}} \mathrm{e}^{\mp i\boldsymbol{k}\cdot\boldsymbol{a}} \langle \boldsymbol{R}+\boldsymbol{R}_\mathrm{A}, s | \mathscr{H} | \boldsymbol{R}'+\boldsymbol{R}_\mathrm{A}, s \rangle \\ =& \epsilon_{2s}, \end{aligned} \tag{3.17}$$

where in the last step just a nearest neighbour approximation and hopping between atomic orbitals at same lattice side were used[5]. Similarly, $\mathscr{H}_{22}$ and $\mathscr{H}_{33}$ can be written as

$$\mathscr{H}_{22} = \langle \phi_{p_x\boldsymbol{k},\boldsymbol{R}_\mathrm{A}} | \mathscr{H} | \phi_{p_x\boldsymbol{k},\boldsymbol{R}_\mathrm{A}} \rangle = \epsilon_{2p} \tag{3.18}$$

$$\mathscr{H}_{33} = \langle \phi_{p_y\boldsymbol{k},\boldsymbol{R}_\mathrm{A}} | \mathscr{H} | \phi_{p_y\boldsymbol{k},\boldsymbol{R}_\mathrm{A}} \rangle = \epsilon_{2p}, \tag{3.19}$$

[5]The closest atom - nearest neighbours are atoms B. Atoms A at the distance $\pm\boldsymbol{a}$ correspond already to second nearest neighbour.

with other elements over atom A being equal to zero due to orthogonality of atomic orbitals. Similarly, one gets $\mathscr{H}_{44} = \epsilon_{2s}$ and $\mathscr{H}_{55} = \mathscr{H}_{66} = \epsilon_{2p}$ and so

$$\mathbb{H}_{AA} = \mathbb{H}_{BB} = \begin{bmatrix} \epsilon_{2s} & 0 & 0 \\ 0 & \epsilon_{2p} & 0 \\ 0 & 0 & \epsilon_{2p}. \end{bmatrix} \tag{3.20}$$

Due to orthogonality of the orbitals, $\mathbb{S}_{AA}$ is found to be

$$\mathbb{S}_{AA} = \mathbb{S}_{BB} = \begin{bmatrix} 1 & 0 & 0 \\ 0 & 1 & 0 \\ 0 & 0 & 1 \end{bmatrix}. \tag{3.21}$$

Solving for off-diagonal matrices $\mathbb{H}_{AB}$,$\mathbb{H}_{BA}$, $\mathbb{S}_{AB}$ and $\mathbb{S}_{BA}$ is a bit more complicated and requires the decomposition of p_x and p_y orbitals into a direction parallel (σ) and perpendicular (π) to a line defined by two nearest neighbour carbon atoms[6]. Using the

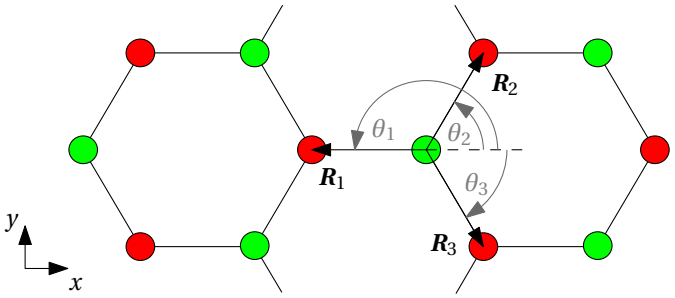

Figure 3.2: Definition of vectors $\boldsymbol{R}_i$ corresponding to nearest neighbours and corresponding angles θ_i of the vectors. Red and green circles show A and B carbon atoms.

definition of the overlap integral matrix elements $\mathscr{H}_{\boldsymbol{R}_\mathrm{A}\boldsymbol{R}_\mathrm{B}\nu\nu'}$

$$\mathscr{H}_{\boldsymbol{R}_\mathrm{A}\boldsymbol{R}_\mathrm{B}\nu\nu'} = \frac{1}{N}\sum_{\boldsymbol{R},\boldsymbol{R}'}^{N} \mathrm{e}^{i\boldsymbol{k}\cdot(\boldsymbol{R}'-\boldsymbol{R})} \langle \boldsymbol{R} + \boldsymbol{R}_\mathrm{A}, \nu | \mathscr{H} | \boldsymbol{R}' + \boldsymbol{R}_\mathrm{B}, \nu' \rangle, \tag{3.22}$$

defining distances $\boldsymbol{R}_i = \boldsymbol{R}' - \boldsymbol{R}$ for nearest neighbours and corresponding angles of the vectors (see figure 3.2), one can write $\mathscr{H}_{14}$ as

$$\mathscr{H}_{14} = \frac{1}{N}\sum_{\boldsymbol{R},\boldsymbol{R}'}^{N} \mathrm{e}^{i\boldsymbol{k}\cdot(\boldsymbol{R}'-\boldsymbol{R})} \langle \boldsymbol{R} + \boldsymbol{R}_\mathrm{A}, s | \mathscr{H} | \boldsymbol{R}' + \boldsymbol{R}_\mathrm{B}, s \rangle = H_{ss\sigma} \sum_{i=1}^{3} \mathrm{e}^{i\boldsymbol{k}\cdot\boldsymbol{R}_i}, \tag{3.23}$$

[6] For further details see appendix B.1.

where $H_{ss\sigma} = \langle \boldsymbol{R} + \boldsymbol{R}_\mathrm{A}, s|\mathscr{H}|\boldsymbol{R}' + \boldsymbol{R}_\mathrm{B}, s\rangle$. Similarly, $\mathscr{H}_{15}$ can be expressed as

$$\mathscr{H}_{15} = \frac{1}{N}\sum_{\boldsymbol{R},\boldsymbol{R}'}^{N} \mathrm{e}^{i\boldsymbol{k}\cdot(\boldsymbol{R}'-\boldsymbol{R})}\langle \boldsymbol{R} + \boldsymbol{R}_\mathrm{A}, s|\mathscr{H}|\boldsymbol{R}' + \boldsymbol{R}_\mathrm{B}, p_x\rangle = H_{sp\sigma}\sum_{i=1}^{3}\mathrm{e}^{i\boldsymbol{k}\cdot\boldsymbol{R}_i}\cos\theta_i, \tag{3.24}$$

where $H_{sp\sigma} = \langle \boldsymbol{R} + \boldsymbol{R}_\mathrm{A}, s|\mathscr{H}|\boldsymbol{R}' + \boldsymbol{R}_\mathrm{B}, p_\sigma\rangle$ and p_σ is a projection of the p orbital to a parallel direction as mentioned before. In order not to break the flow of the text, the rest of the elements for both transfer and overlap integral matrices is listen in appendix B.2.

3.2 Many-Body Effects

In this chapter a theoretical description of how general many-body effects can be modelled is given. Even though the many-body effects could be introduced directly through a spectral function and self-energy, the first two sections are intended to provide a deeper understanding of related physical concepts. In the last section, effects of electron-phonon coupling are calculated.

3.2.1 Introduction to Green's Functions

In order to understand many-body effects on the $\boldsymbol{k}$-resolved inverse photoemission spectroscopy (KRIPES) spectra, an important concept stemming from the theory of ordinary and partial differential equations has to be introduces, the so called Green's function method.

Consider a linear differential equation

$$Lu(\boldsymbol{r}) = f(\boldsymbol{r}), \tag{3.25}$$

where L is the corresponding linear differential operator, $u(\boldsymbol{r})$ is the solution of the equation, and $f(\boldsymbol{r})$ is the source term. The Green's function $G(\boldsymbol{r})$ of the system is then defined as

$$LG(\boldsymbol{r}) = \delta(\boldsymbol{r}), \tag{3.26}$$

where $\delta(\boldsymbol{r})$ is the Dirac delta function.

The solution of the differential equation can then be found by a convolution of the Green's function and the source function

$$u(\boldsymbol{r}) = \int \mathrm{d}\boldsymbol{r}' G(\boldsymbol{r} - \boldsymbol{r}')f(\boldsymbol{r}'). \tag{3.27}$$

After letting L act on the final equation and substituting from the Eq. (3.26), an identity to Eq. (3.25) is obtained. As it can be seen from Eq. (3.27), Green's function fully char-

acterises the original differential equation. As it will be later shown, Green's functions provide a direct tool to account for many body effects in a simple scenario.

3.2.2 Green's Function of Free Particles and the Spectral Function

In quantum theory, the Green's functions formalism can also be adopted. The full derivation will not be given here, but results related to this thesis will be summarized. For a proper treatment see Ref.[98] and Ref. [51].

For a free single particle, the Schrödinger equation can be used to describe the wave, which can be written as

$$(EI - H_0(\boldsymbol{r}))\psi(\boldsymbol{r}) = 0. \tag{3.28}$$

Defining the two-point Green's function as

$$(EI - H_0(\boldsymbol{r}))G_0(\boldsymbol{r}, \boldsymbol{r}', E) = \delta(\boldsymbol{r} - \boldsymbol{r}'), \tag{3.29}$$

it can be shown that the Fourier transform of $G_0(\boldsymbol{r}, \boldsymbol{r}', E)$ of a form $G_0(\boldsymbol{r}\,t, \boldsymbol{r}'\,t')$ takes a role of a particle propagator. In other words, evolution of the wave function $\psi(\boldsymbol{r}, t)$ is fully determined by its initial state $\psi(\boldsymbol{r}', t')$ and the Green's function

$$\psi(\boldsymbol{r}, t) = \int \mathrm{d}\boldsymbol{r}' G_0(\boldsymbol{r}\,t, \boldsymbol{r}'\,t')\psi(\boldsymbol{r}', t'). \tag{3.30}$$

For a translationally invariant system, the resulting $G_0(\boldsymbol{r}, \boldsymbol{r}', E)$ can only depend on the difference $\boldsymbol{r} - \boldsymbol{r}'$. After Fourier transforming the $\boldsymbol{k}$-space representation, $G_0(\boldsymbol{k}, E)$ is obtained.

The cumbersome description of the Green's function was given since it has a direct connection to the experiment, through a so called spectral function which will be introduced shortly. Moreover, frequently in many-body physics, many system can be seen as the free particle-like systems to the first approximation.

The non-interacting system can be described by the quadratic Hamiltonian

$$H = \sum_{\boldsymbol{k}} \epsilon(\boldsymbol{k}) a^\dagger_{\boldsymbol{k}} a_{\boldsymbol{k}}, \tag{3.31}$$

where $\boldsymbol{k}$ is, as usual, the particle wave vector and $\epsilon(\boldsymbol{k})$ is an eigenvalue of the system. The free single-particle Green's function can then be written as

$$G_0(\boldsymbol{k}, E) = \frac{1}{E - \epsilon(\boldsymbol{k}) + i\eta(\boldsymbol{k})}, \tag{3.32}$$

where $i\eta(\boldsymbol{k})$ was added to prevent a divergence in the Fourier transform integrals. To account for a difference between holes (below Fermi energy E_F) and electrons (above E_F),

$\eta(\boldsymbol{k}) = \mathrm{sgn}(\epsilon(\boldsymbol{k}) - E_\mathrm{F})\,\eta$, where η is an infinitesimally small number and $\mathrm{sgn}(\epsilon(\boldsymbol{k}) - E_\mathrm{F}) = 1$ for $\epsilon(\boldsymbol{k}) > E_\mathrm{F}$ and -1 otherwise[7].

As a final step, the previously mentioned spectral function can be introduced. In the case of a particle (an electron), particle spectral function can be written as

$$A^+(\boldsymbol{k}, E) = -\frac{1}{\pi}\mathrm{Im}G(\boldsymbol{k}, E), \tag{3.33}$$

where $\mathrm{Im}G(\boldsymbol{k}, E)$ denotes an imaginary part of the corresponding Green's function[8].

For the free particle Green's function defined in Eq. (3.32) one gets

$$A^+(\boldsymbol{k}, E) = -\frac{1}{\pi}\mathrm{Im}G_0(\boldsymbol{k}, E) = \delta\left(E - \epsilon(\boldsymbol{k})\right), \tag{3.34}$$

which is nothing but a Dirac delta function. As the name suggests, $A^+(\boldsymbol{k}, E)$ reflects the spectrum of the particles. In other words, it describes the energies the particles can be measured with a specific $\boldsymbol{k}$. This has a direct connection to inverse photo-emission measurements, as will be shown later. From Eq. 3.34 one sees that the free particle can be measured with energy just equal to $\epsilon(\boldsymbol{k})$ and for other energies the particle cannot exist.

3.2.3 Quasi-Particles Picture and Self-energy

So far, the system was treated as a free single-particle system. However, in the presence of interactions, the one-particle treatment should be replaced by proper many-body calculations which complicates everything significantly. In many cases, however, the quasi-particle picture can be used.

Figure 3.3 shows a positively charged particle coming into the system where the particle is consequently surrounded by a cloud of negatively charged particles. Due to the presence of the cloud, screening effects are present, and the movement of the original particle is modified. Moreover (again due to the screening), the newly created quasi-particle (the original particle and the cloud) only weakly interacts with other quasi-particles. This is why the concept is so useful. Many-body physics can be simply treated by an introduction of quasi-particles with a finite lifetime τ to account for a decay of the wave function in time due to the interactions. The quasi-particle is further characterized by a renormalized energy $\epsilon(\boldsymbol{k})'$ replacing the energy $\epsilon(\boldsymbol{k})$ of a bare (or undressed) particle defined in the previous section.

[7] Introduction of $i\eta(\boldsymbol{k})$ corresponds to a modification of $G_0(\boldsymbol{k}, t, t')$ by an exponential time decay factor with $\eta(\boldsymbol{k})$ being the decay rate.

[8] In the literature, different pre-factors in the definitions of the spectral function can be found. In this work, definition used in majority of spectroscopic articles is taken.

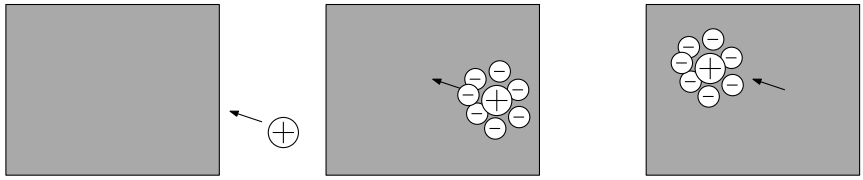

Figure 3.3: Quasi-particle concept illustration. A positively charged particle is surrounded by a cloud of negatively charged particles and together they travel through the medium. The incoming particle and the surrounding cloud are then called a quasi-particle which can be characterized by its lifetime τ and by a renormalized energy ϵ' and can be described using a single-particle picture.

The finite lifetime and the energy correction to the original bare energy can be introduced in so called Self-energy $\Sigma(\boldsymbol{k}, E)$. The renormalized energy is then given by

$$\epsilon(\boldsymbol{k})' = \epsilon(\boldsymbol{k}) + \Sigma(\boldsymbol{k}, E) = \epsilon(\boldsymbol{k}) + \Sigma'(\boldsymbol{k}, E) + i\Sigma''(\boldsymbol{k}, E), \tag{3.35}$$

where $\Sigma'(\boldsymbol{k}, E)$ and $\Sigma''(\boldsymbol{k}, E)$ are the real and imaginary parts of self-energy. The real part expresses the energy correction, whereas the imaginary part accounts for the finite lifetime and can be expressed as $\Sigma''(\boldsymbol{k}, E) = \hbar/\tau$.

3.2.4 Spectral Function for Interacting Particle

Once the self energy is known, effects on self-energy can be investigated. This can be done through Dyson equation[9] which can be expressed as

$$G(E, \boldsymbol{k}) = G_0(E, \boldsymbol{k}) + G_0(E, \boldsymbol{k})\Sigma(E, \boldsymbol{k})G(E, \boldsymbol{k}), \tag{3.36}$$

and formally solved by

$$G(E, \boldsymbol{k}) = \frac{1}{G_0^{-1}(E, \boldsymbol{k}) - \Sigma(E, \boldsymbol{k})}. \tag{3.37}$$

After substitution of the single particle Green's function (Eq. 3.32), the previous equation takes the form

$$G(E, \boldsymbol{k}) = \frac{1}{E - \epsilon(\boldsymbol{k}) - \Sigma(E, \boldsymbol{k})} = \frac{1}{E - [\epsilon(\boldsymbol{k}) + \Sigma'(E, \boldsymbol{k})'] - i\Sigma''(E, \boldsymbol{k})}, \tag{3.38}$$

leading directly to the expression of the spectral function

$$A^+(E, \boldsymbol{k}) = \frac{1}{\pi} \frac{\Sigma''(E, \boldsymbol{k})}{\left[E - \left(\epsilon(\boldsymbol{k}) + \Sigma'(E, \boldsymbol{k})\right)\right]^2 + \Sigma''(E, \boldsymbol{k})^2} \tag{3.39}$$

[9] For a derivation of the Dyson equation see for example Ref. [51] or Ref. [98]

which corresponds to the Lorentzian distribution. In other words, the quasi-particle will not be sharply localized at $E = \epsilon(\boldsymbol{k})$, but distributed around the renormalized energy $E = \epsilon(\boldsymbol{k}) + \Sigma'(E, \boldsymbol{k})$ due to the finite lifetime (represented by $\Sigma''(E, \boldsymbol{k})$).

Connecting this chapter to the previously described TB model, the bare band energy $\epsilon(\boldsymbol{k})$ is nothing but the energy eigenvalue $\mathscr{E}_\mu$ of the TB Hamiltonian.

3.2.5 Modelling Electron-Phonon Coupling

In section 2.1.6, a discussion about symmetries was presented with a conclusion that electrons in occupied sigma bands of graphene can possibly couple to both acoustic (TA, LA) and optical phonons (TO, LO). In this work, only a coupling to optical phonons and only scattering within the σ^* bands is considered. Due to the high acoustic phonon energies, this type of coupling would bring the strongest effects in the energy bands.

As previously discussed, in the presence of interactions, the energy of bare bands is modified which can be characterized by the self-energy. The imaginary part of the self energy can be described [99, 100] by

$$\begin{aligned}\Sigma''(\mathscr{E}_\mu) =& \Sigma''_0 + \pi \int_0^{\omega_{\max}} \mathrm{d}\omega \Big\{ \alpha^2(\mathscr{E}_\mu, \omega) F_{\mathrm{E}}(\mathscr{E}_\mu, \omega) \left[1 + n(\omega) - f(\mathscr{E}_\mu - \hbar\omega)\right] \\ &+ \alpha^2(\mathscr{E}_\mu, \omega) F_{\mathrm{A}}(\mathscr{E}_\mu, \omega) \left[1 + n(\omega) - f(\mathscr{E}_\mu + \hbar\omega)\right] \Big\},\end{aligned} \tag{3.40}$$

where $\alpha^2(\mathscr{E}_\mu, \omega) F_{\mathrm{A}}(\mathscr{E}_\mu, \omega)$ and $\alpha^2(\mathscr{E}_\mu, \omega) F_{\mathrm{E}}(\mathscr{E}_\mu, \omega)$ are Eliashberg coupling functions for absorption and emission respectively, $n(\omega)$ and $f(\mathscr{E}_\mu - \hbar\omega)$ are Bose-Einstein and Fermi-Dirac statistics accounting for finite temperature, $\mathscr{E}_\mu$ is the energy of the final bare electron band (calculated in the TB model), $\omega_{\max}$ is the maximum frequency of phonons and where Σ''_0 accounts for electron-electron interactions and electron-defect scattering and can be considered constant for the small energy range of $\mathscr{E}_\mu$ with which this thesis is concerned [28].

For energies high above the Fermi level, $f(\mathscr{E}_\mu - \hbar\omega) \to 0$ and for coupling to LO and TO optical phonons with energies above 150 meV and room temperatures $n(\omega)$ can also be neglected which yields

$$\Sigma''(\mathscr{E}_\mu) = \Sigma''_0 + \pi \int_0^{\omega_{\max}} \mathrm{d}\omega \alpha^2(\mathscr{E}_\mu, \omega) F_{\mathrm{E}}(\mathscr{E}_\mu, \omega). \tag{3.41}$$

In other words, the resulting imaginary part of the self-energy is dominated by phonon emission.

To model coupling to optical phonons, Einstein phonon model is used [101]. It is based on quantum harmonic oscillators oscillating with the same frequency ω_{E} which gives only one energy of phonons in comparison to Debye model [102]. This energy is

assumed to be 190 meV which corresponds to energy of LO and TO phonons around the Γ point (see Fig. 2.6a)).

The Eliahsber coupling function can be split into two parts, $F_{\mathrm{E}}(\mathscr{E}_\mu,\omega)$, phonon density of states and $\alpha^2(\mathscr{E}_\mu,\omega)$ which can be interpreted as an effective electron-phonon coupling function averaged over the Fermi surface [99]. The former can be expressed as a delta function $\delta(\omega-\omega_{\mathrm{E}})$ since there are only phonons with a single frequency, ω_{E}. The latter has to reflect that the scattering can occur if the energy of the electron is beyond $\hbar\omega_{\mathrm{E}}$ above the minimum of the sigma band. For lower energies, the electron cannot decay though the optical phonon since the energy difference is too small (there no phonons within this energy range) and hence the life-time of the state will be longer (remember the connection between life-time and the imaginary part of self energy). For two-dimensional nearly parabolic bands the Eliahsber coupling function can be expressed [28] as

$$\alpha^2(\mathscr{E}_\mu,\omega)F_{\mathrm{E}}(\mathscr{E}_\mu,\omega)=\lambda\frac{\omega_{\mathrm{E}}}{2}\delta(\omega-\omega_{\mathrm{E}})\Theta(\mathscr{E}_\mu+\hbar\omega_{\mathrm{E}}), \tag{3.42}$$

where λ is electron-phonon coupling constant and where Θ is the Heavy side function[10].

To account for the broadening of the bottom of the final energy state, the Heavyside function should be modified to a smoothly changing function which reflects the character of the broadening as suggested in Ref. [29]. The shape of the function does not quantitatively affect the results but removes artificially high peaks in the spectral function. Since the broadening is unknown, the Heavyside function can be approximated by a Fermi-Dirac distribution[11] of a finite temperature T =400 K. Moreover, in order to account for electron-impurity scattering and electron-electron interactions Σ_0'' = 100 meV is used [12]. The strong coupling was represented by λ = 1 which was the first prediction from the density function theory from other colleagues.

[10] The Heavy side function $\Theta(x)$ is defined being 0 for $x<0$ and 1 otherwise.

[11] Fermi edge corresponds to Gaussian broadening of the final.

[12] The values Σ_0'' = 100 meV and also T =400 K are intentionally higher than for the used previously in occupied bands [29] for more possible electron scattering events due to a presence of more energy band above Fermi level. The constant value is just an approximation since the value can be expected to vary slowly within the working energy range.

3.3 Revision of IPES theory and Matrix Element Calculation

As previously described, IPES is a tool to investigate the unoccupied energy bands both below and above vacuum level. Basic working principles and the energy diagram (2.9c)) have been already introduced in Chapter 2, but a more thorough discussion has to be made to be able to calculate the expected intensity in an IPES experiment.

3.3.1 IPES Intensity in Ideal Systems

The formal theory for IPES was derived in the so called "one-step" model[103]. This model simultaneously treats three main parts of the process:

i) Penetration of the electron to the surface and its coupling to the initial state

ii) Inelastic electron-electron scattering

iii) Optical de-excitation

The one-step model is not easy to implement and does not offer an easy interpretation. An alternative is offered in the form of the "three-step" model which separates the three previously mentioned steps. The model was firstly proposed and successfully used in PES [104, 28, 28], however, later also modified for IPES [103, 105].

In the first step the coupling between the the incoming electron and the initial wave function can be described by a coupling constant c_i which can be calculated as an overlap between the corresponding wave functions [106]. Moreover, energy conservation for transmission of an electron from vacuum to initial state has to be satisfied and can be expressed as

$$E_\mathrm{i} = E_\mathrm{kin} + \phi, \tag{3.43}$$

where E_kin denotes electron kinetic energy in a vacuum, E_i is the energy of the initial state and ϕ stands for the material work function.

After the electron penetration, there is a finite probability $\beta(E)$ for non-radiative decay mainly due to electron-electron interactions, which is the reason for the low penetration depth of low energy electrons and IPES surface sensitivity [105]. The probability for radiative processes is then $1-\beta(E)$ and is assumed to be constant for the low energy range where the electron-phonon coupling will be investigated.

The last step is optical de-excitation. Figure 3.4 shows an example of a simple band structure with two bands above the Fermi level and an electron transition from the initial state (denoted by subscript i) to the final state (denoted by subscript f). The transition probability inside the bulk can be determined by first-order perturbation theory

using Fermi's golden rule

$$\Gamma_{i\to f} = \frac{2\pi}{\hbar}|\langle f|H'|i\rangle|^2\delta(E_\mathrm{i} - E_\mathrm{f} - \hbar\omega) = \frac{2\pi}{\hbar}|M_\mathrm{fi}|^2\delta(E_\mathrm{i} - E_\mathrm{f} - \hbar\omega), \tag{3.44}$$

where $|i\rangle$ and $|f\rangle$ denote initial and final state respectively, H' is the perturbation due to the photon field (which will be discussed later), $|M_\mathrm{fi}|$ are matrix elements of the transition and $\delta(E_\mathrm{i} - E_\mathrm{f} - \hbar\omega)$ stands for conservation of energy for the transition from the initial to the final state while emitting s photon with energy $\hbar\omega$.

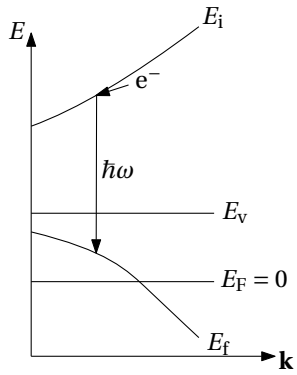

Figure 3.4: Schematic illustration of electron transition from the initial state with energy E_i to the final state with energy E_f. During the process, a photon of energy $\hbar\omega = E_\mathrm{i} - E_\mathrm{f}$ is emitted. The transition is displayed purely horizontally due to the small momentum carried by a photon which can be neglected for photon energies below 100 eV.

Another conservation law which has to be satisfied is conservation of momentum

$$\boldsymbol{k}_\mathrm{f} = \boldsymbol{k}_\mathrm{i} + \boldsymbol{G} + \boldsymbol{k}_\mathrm{photon}, \tag{3.45}$$

where $\boldsymbol{k}_\mathrm{i}$ and $\boldsymbol{k}_\mathrm{f}$ are the initial and final states momenta, $\boldsymbol{G}$ stands for an arbitrary reciprocal lattice vector and $\boldsymbol{k}_\mathrm{photon}$ is the photon momenta. For ultra violent (UV) transitions photon momentum is small and can be neglected. Therefore, the band transitions can be seen as vertical in a reduced Brillouin zone scheme (figure 3.4). It is worth noting that the equation is only exactly valid inside the solid due to an attractive potential near the surface. For an incoming electron with momentum $\boldsymbol{K}$ in a vacuum, however, the perpendicular momentum is not conserved due to attractive forces in the vicinity of the solid and hence $\boldsymbol{k}_{\perp,\mathrm{i}} > \boldsymbol{K}_\perp$. Only the parallel momentum is preserved which can be expressed by

$$\boldsymbol{k}_{\parallel,\mathrm{i}} = \boldsymbol{K}_\parallel + \boldsymbol{G}_\parallel. \tag{3.46}$$

Taking into account the conservation laws (equations (3.43), (3.45) and (3.46)), a connection between $\boldsymbol{K}_\parallel$ and the final band energy E_f can be written. Eliminating $\boldsymbol{K}_\parallel$

from the energy kinetic energy E_{kin} of a free electron and using the mentioned conservation laws, the final expression takes a form

$$\boldsymbol{K}_{\parallel} = \left(2m/\hbar^2(E_{\text{f}} + \hbar\omega - \phi)\right)^{1/2} \sin\theta, \tag{3.47}$$

where θ is the angle of incidence of electrons to the surface as defined in section 2.3.1. The equation provides a direct possibility to map the final energy states to $\boldsymbol{K}_{\parallel}$.

If we now consider Fermi's golden rule (equation (3.44)) in light of the conservation rules, the final intensity of the transition is written as

$$I(E_{\text{kin}}, \boldsymbol{K}_{\parallel}) \propto c_{\text{i}} |M_{\text{fi}}|^2 \delta(E_{\text{i}} - E_{\text{f}} - \hbar\omega)\delta(E_{\text{i}} - E_{\text{kin}} - \phi)\delta(\boldsymbol{k}_{\text{f}} - \boldsymbol{k}_{\text{i}} - \boldsymbol{G})\delta(\boldsymbol{k}_{\parallel,\text{i}} - \boldsymbol{K}_{\parallel}). \tag{3.48}$$

In the presence of multiple initial and final states and multiple reciprocal lattice vectors $\boldsymbol{G}$ the previous equation can be written as

$$I(E_{\text{kin}}, \boldsymbol{K}_{\parallel}) \propto \sum_{\boldsymbol{G},i,f} c_{\text{i}} |M_{\text{fi}}|^2 \delta(E_{\text{i}} - E_{\text{f}} - \hbar\omega)\delta(E_{\text{i}} - E_{\text{kin}} - \phi)\delta(\boldsymbol{k}_{\text{f}} - \boldsymbol{k}_{\text{i}} - \boldsymbol{G})\delta(\boldsymbol{k}_{\parallel,\text{i}} - \boldsymbol{K}_{\parallel}), \tag{3.49}$$

where the summation goes through all possible transitions with both initial and final states above E_{F}.

It is worth noting that Eq. (3.48) neither accounts for many-body effects nor the resolution of the experimental apparatus, which is the content of the next section. Without the inclusion of many-body effects and the resolution of the experimental apparatus, only infinitely sharp peaks would be seen in the spectrum.

3.3.2 Instrumentation and Many-body Effects

At this point, accounting for many-body physics and the measurement apparatus itself have not been introduced. Using a modification of the theory for ARPES [107] and accounting for just one final state, equation (3.48) can be rewritten as

$$\begin{aligned} I(E_{\text{kin}}, \boldsymbol{K}_{\parallel}) \propto \sum_{\boldsymbol{G}} \int \mathrm{d}\omega \int \mathrm{d}E_{\text{i}} \int \mathrm{d}\boldsymbol{k}_{\text{i},\parallel} \int \mathrm{d}k_{\text{i},\perp} c_{\text{i}} |M_{\text{fi}}|^2 \times D_E(\hbar\omega) \times A(E_{\text{i}} - E_{\text{f}} - \hbar\omega) \\ \times A_{\text{beam}}(E_{\text{i}} - E_{\text{kin}} - \phi)\delta(\boldsymbol{k}_{\parallel,\text{f}} - \boldsymbol{k}_{\parallel,\text{i}} - \boldsymbol{G}_{\parallel}) \times \delta(k_{\perp,\text{f}} - k_{\perp,\text{i}} - G_{\perp}) \\ \times A_{\text{beam}}(\boldsymbol{k}_{\parallel,\text{i}} - \boldsymbol{K}_{\parallel}), \end{aligned} \tag{3.50}$$

where $D_E(\hbar\omega)$ is the detector energy resolution function, $A(E_{\text{i}} - E_{\text{f}} - \hbar\omega)$ is the particle spectral function which accounts for effects at the final electronic state, $A_{\text{beam}}(E_{\text{i}} - E_{\text{kin}} - \phi)$ and $A_{\text{beam}}(\boldsymbol{k}_{\parallel,\text{i}} - \boldsymbol{K}_{\parallel})$ are the electron source energy and momentum spectral functions and where $\delta(\boldsymbol{k}_{\text{f}} - \boldsymbol{k}_{\text{i}} - \boldsymbol{G})$ from Eq. (3.48) was split into its parallel and perpendicular parts. The integration over σ comes from the necessity of including a photon detector which serves as a band-pass filter (see section 2.3.3).

As discussed in Ref. [107] with relation to PES, broadening of the final electronic state is much smaller than the lifetime suggests [13] and is rather related to real-space damping of the electronic wave function. Due to the similarity of PES and IPES, similar effects are expected in the IPES measurements. The broadening of the initial state due to the real-space damping can be accounted for by a Lorentzian distribution around the undamped $K_\perp^0$ of the incoming electron replacing $\delta(k_{\perp,\mathrm{f}} - k_{\perp,\mathrm{i}} - G_\perp)$. For 2D states, neither of the other distributions is dependent on $k_{\perp,\mathrm{i}}$ and the integral becomes 1 for sufficiently high $K_\perp^0$ [108].

For the purposes of this work, c_i is considered to be constant and equal for all orbital types, while $|M_\mathrm{fi}|$ is a slowly varying quantity in either of the integration variables. Therefore, both c_i and $|M_\mathrm{fi}|$ can be removed from the integrals. Moreover and being just slowly varying quantity in eider of the integration variables, so both can be taken out of the integrals. Moreover, integration over ω is just a convolution (denoted later by $*$) between D_E and A. Similarly, the integration over E_i can be also transferred to convolution since $A_\mathrm{beam}(E_\mathrm{i} - E_\mathrm{kin} - \phi)$ can be approximated by a Gaussian distribution and is this symmetric with respect to sign change of the integration variable. Similarly, the integration over $\boldsymbol{k}_{\parallel,\mathrm{i}}$ leads to the convolution due to the fact that A is, in general, $\boldsymbol{k}_{\parallel,\mathrm{i}}$-dependent[14]. Considering $\boldsymbol{G}_\parallel = 0$ (which is proffered - see Ref. [106]), the intensity yields a simple expression

$$\begin{aligned} I(E,\boldsymbol{K}_\parallel) &\propto \left(D_E(E) * A_\mathrm{beam}(E) * A_\mathrm{beam}(\boldsymbol{K}_\parallel)\right) * \left(c_\mathrm{i}|M_\mathrm{fi}|^2 \times A^+(E,\boldsymbol{K}_\parallel)\right) \\ &= \left(D_\mathrm{tot}(E) * A_\mathrm{beam}(\boldsymbol{K}_\parallel)\right) * \left(c_\mathrm{i}|M_\mathrm{fi}|^2 \times A^+(E,\boldsymbol{K}_\parallel)\right), \end{aligned} \tag{3.51}$$

where $E = E_\mathrm{kin} + \phi - \hbar\omega$ was introduced for convenience. After the change of variables, $A(E_\mathrm{i} - E_\mathrm{f} - \hbar\omega)$ is nothing but the spectral function from Eq. (3.39)

$$A^+(E,\boldsymbol{K}_\parallel) = \frac{1}{\pi} \frac{\Sigma''(E,\boldsymbol{K}_\parallel)}{\left[E - \left(\epsilon(\boldsymbol{K}_\parallel) + \Sigma'(E,\boldsymbol{K}_\parallel)\right)\right]^2 + \Sigma''(E,\boldsymbol{K}_\parallel)^2}, \tag{3.52}$$

where the $\boldsymbol{K}_\parallel$ is used instead of $\boldsymbol{k}$ in the original expression, using the conservation laws introduced in the previous section[15] and the fact that considered bands are 2D.

[13] remember the connection between the quasi-particle lifetime and the imaginary part of the self-energy.

[14] It is worth noting that this approximation is just correct for flat bands without strong dispersion due to A being dependent on the final state momenta $\boldsymbol{k}_{\parallel,\mathrm{f}}$ and hence also dependent on $\boldsymbol{k}_{\parallel,\mathrm{i}}$ and $\boldsymbol{K}_\parallel$. This fact interconnects the energy resolution to the momentum resolution. For dispersive bands, asymmetry in energy resolution is created due to averaging over certain $\boldsymbol{k}_{\parallel,\mathrm{i}}$. For the purposes of the thesis, however, this effect is neglected.

[15] The conservation law is included in the intensity expression (3.50). The change from $\boldsymbol{k}_{\parallel,\mathrm{f}}$ to $\boldsymbol{K}_\parallel$ is just an approximation which is a part of the assumption that the final $\boldsymbol{K}_\parallel$ broadening can be accounted for as using the convolution.

In this work, the detector function is approximated by a Gaussian distribution[16] as

$$D_E(E) = \frac{1}{\sqrt{2\pi}\Gamma_{\text{det}}} \exp\left(-\frac{1}{2}\frac{E^2}{\Gamma_{\text{det}}}\right), \tag{3.53}$$

where $\Gamma_{\text{det}} = \Delta E_{\text{det}}/\sqrt{8\ln 2}$ is determined by the detector energy resolution ΔE_{det} (full width at half maxima (FWHM) of the detector band pass filter). Similarly, the electron energy spectrum $A_{\text{beam}}(E)$ can also be approximated by a Gaussian distribution using Eq.(3.53) and exchanging ΔE_{det} for electron beam energy spread ΔE_{beam} instead. In the experiments, typically $D_E(E) * A_{\text{beam}}(E)$ is measured, not a separated component and is denoted by $D_{\text{tot}}(E)$ and has a FWHM ΔE_{tot}. Due to the properties of the Gaussian function, the resulting shape of $D_{\text{tot}}(E)$ is also expected to be Gaussian and will be used throughout the simulations.

The momentum spread function $A_{\text{beam}}(\boldsymbol{K}_\parallel)$ is also approximated by the a Gaussian distribution as

$$A_{\text{beam}}(\boldsymbol{K}_\parallel) = \frac{1}{\sqrt{2\pi}\Gamma_{\text{beam},\boldsymbol{K}_\parallel}} \exp\left(-\frac{1}{2}\frac{E^2}{\Gamma_{\text{beam},\boldsymbol{K}_\parallel}}\right), \tag{3.54}$$

where $\Gamma_{\text{beam},\boldsymbol{K}_\parallel} = \Delta\boldsymbol{K}_\parallel\sqrt{8\ln 2}$ with $\Delta\boldsymbol{K}_\parallel$ being the FWHM of the electron $\boldsymbol{K}_\parallel$-spread. In reality, $A_{\text{beam}}(\boldsymbol{K}_\parallel)$ is not constant but changes with a change of kinetic energy and the incident angle of electrons.

3.3.3 The Interaction Hamiltonian

So far, no attention has been paid to the matrix elements[17] M_{fi} and corresponding interaction Hamiltonian H'. Considering the non-relativistic one-particle approximation, the particle-light interaction can be governed by a Hamiltonian of the form

$$H = \left[\frac{1}{2m}\left(\frac{\hbar}{i}\boldsymbol{\nabla} - \frac{e}{c}\boldsymbol{A}(\boldsymbol{r})\right) + \boldsymbol{V}(\boldsymbol{r})^2\right] \tag{3.55}$$

where, $\boldsymbol{A}(\boldsymbol{r})$ is the vector potential of the time-dependent electromagnetic field, $\boldsymbol{\nabla}$ is the gradient operator, $\boldsymbol{V}(\boldsymbol{r})$ denotes potential energy and m, e, c stand for electron mass, electron charge and speed of light respectively. After subtraction of the unperturbed Hamiltonian

$$H_0 = -\frac{\hbar^2}{2m}\boldsymbol{\nabla}^2 + \boldsymbol{V}(\boldsymbol{r}), \tag{3.56}$$

[16] This is true for gas detectors [109]. Solid state detectors have non-Gaussian shapes as will be shown later in Chapter 5.

[17] The matrix elements were defined in Eq. (3.44) as $\langle f|H'|i\rangle$ as a probability of transition from the initial to the final electronic state.

the interaction Hamiltonian reads

$$H' = \frac{e}{2mc}\left[-\frac{\hbar}{i}\Big(\boldsymbol{\nabla}\cdot\boldsymbol{A}(\boldsymbol{r}) + \boldsymbol{A}(\boldsymbol{r})\cdot\boldsymbol{\nabla}\Big) + \frac{e}{c}\boldsymbol{A}(\boldsymbol{r})^2\right]. \tag{3.57}$$

Before further steps, one important thing should questioned. The possibility to use the previously described theory. At the beginning there are no protons present in the IPES and hence no interactions with electrons should not be possible. This question concerned people already in connection with spontaneous emission. For its proper treatment $\boldsymbol{A}(\boldsymbol{r})$ has to be quantized, as discussed in Ref. [67]. For application in solids, the theory developed for PES can be used with hardly any changes. Since the quantization of the field is not essential for this work, semi-classical treatment developed for PES will be followed, however, the reader is encouraged to check the formal derivation in some of the quantum optics books.

If the electromagnetic field is weak (which is the case for IPES), the non-linear term can be neglected. If one assumes small variations of $\boldsymbol{A}(\boldsymbol{r})$, the first term also disappears. The interaction Hamiltonian then reads

$$H' = -\frac{e\hbar}{2imc}\boldsymbol{A}(\boldsymbol{r})\cdot\boldsymbol{\nabla} = -\frac{e}{2mc}\boldsymbol{A}(\boldsymbol{r})\cdot\boldsymbol{p}, \tag{3.58}$$

where $\boldsymbol{p}$ is the momentum operator. In a dipole approximation one gets

$$H' = -\frac{e\hbar}{2imc}\boldsymbol{e}\cdot\boldsymbol{\nabla}, \tag{3.59}$$

where $\boldsymbol{e}$ is the light polarization vector.

3.3.4 Calculation of Matrix Elements

Using the TB framework which was developed in Chapter 3.1, matrix elements can be calculated. In ARPES, a plane wave approximation of the final electronic state already showed its validity for graphite [92] and also for unoccupied σ bands in graphene [28, 29] which have the same origin as the unoccupied σ states which were discussed previously. Therefore the same assumption is used for the initial wave function. The following derivation of the KRIPES matrix elements is based on a thorough theory derivation presented in Ref. [110] related to ARPES.

Assume an initial electron to be free electron-like[18] denoted by $|\boldsymbol{k}_i\rangle$ and in position representation $\psi_\mathrm{i} \equiv \langle\boldsymbol{r}|\boldsymbol{k}_\mathrm{i}\rangle \equiv e^{i\boldsymbol{k}_\mathrm{i}\cdot\boldsymbol{r}}$, where $\boldsymbol{k}_\mathrm{i}$ are the wave vector electrons in the initial electronic state and are equal to the waves vector of incoming electrons, not considering damping of the initial wave-function. The final state, the Bloch state, with band

[18] This assumption seems to be reasonable due to a presence of a continuum of states above the first two unoccupied σ^* states (see section 4.1).

index μ can be (in a TB approximation) written as (3.7))

$$|\psi_{\mu \boldsymbol{k}_\mathrm{f}}\rangle = \frac{1}{\sqrt{N}} \sum_{\boldsymbol{R}} \mathrm{e}^{i \boldsymbol{k}_\mathrm{f} \cdot \boldsymbol{R}} \sum_{\boldsymbol{R}_\mathrm{j}} \sum_{\nu} c_{\mu, \boldsymbol{R}_\mathrm{j} \nu}(\boldsymbol{k}_\mathrm{f}) |\boldsymbol{R} + \boldsymbol{R}_\mathrm{j}, \nu\rangle, \tag{3.60}$$

where, once more, $\boldsymbol{k}_\mathrm{f}$ is the wave vector of the final Bloch state, $|\boldsymbol{R}+\boldsymbol{R}_\mathrm{j}, \nu\rangle$ are real atomic orbitals (indexed by $\nu = p_x, p_y, s$) at position $\boldsymbol{R} + \boldsymbol{R}_\mathrm{j}$. $\boldsymbol{R}$ is the lattice side position and $\boldsymbol{R}_\mathrm{j}$ are positions of atoms in the unit cell. The summations run over all lattice sides relevant to the experiment and all atoms in the unit cell.

Considering an interacting Hamiltonian in a dipole approximation from the previous section (eq. (3.59)), matrix elements can be expressed as

$$\begin{aligned} M_{\mathrm{fi},\mu} &= \langle \psi_{\mu \boldsymbol{k}_\mathrm{f}} | H' | \boldsymbol{k}_i \rangle \\ &\propto \frac{1}{\sqrt{N}} \sum_{\boldsymbol{R}} \mathrm{e}^{i \boldsymbol{k}_\mathrm{f} \cdot \boldsymbol{R}} \sum_{\boldsymbol{R}_\mathrm{j}} \sum_{\nu} c_{\mu, \boldsymbol{R}_\mathrm{j} \nu}(\boldsymbol{k}_\mathrm{f}) \langle \boldsymbol{R} + \boldsymbol{R}_\mathrm{j}, \nu | \boldsymbol{e} \cdot \boldsymbol{\nabla} | \boldsymbol{k}_i \rangle \\ &= (i \boldsymbol{e} \cdot \boldsymbol{k}_\mathrm{i}) \frac{1}{\sqrt{N}} \sum_{\boldsymbol{R}} \mathrm{e}^{i \boldsymbol{k}_\mathrm{f} \cdot \boldsymbol{R}} \sum_{\boldsymbol{R}_\mathrm{j}} \sum_{\nu} c_{\mu, \boldsymbol{R}_\mathrm{j} \nu}(\boldsymbol{k}_\mathrm{f}) \langle \boldsymbol{R} + \boldsymbol{R}_\mathrm{j}, \nu | \boldsymbol{k}_i \rangle \\ &= (i \boldsymbol{e} \cdot \boldsymbol{k}_\mathrm{i}) \frac{\sqrt{N}}{V} \sum_{\boldsymbol{R}_\mathrm{j}} \sum_{\nu} c_{\mu, \boldsymbol{R}_\mathrm{j} \nu}(\boldsymbol{k}_\mathrm{f}) \langle \boldsymbol{R}_\mathrm{j}, \nu | \boldsymbol{k}_i \rangle, \end{aligned} \tag{3.61}$$

where in the last step summation over $\boldsymbol{R}$ was written as an the integral $\frac{N}{V} \int \mathrm{d}\boldsymbol{R}$. The matrix elements can be further rewritten as

$$M_{\mathrm{fi},\mu} \propto \boldsymbol{e} \cdot \boldsymbol{k}_\mathrm{i} \sum_{\boldsymbol{R}_\mathrm{j}} \sum_{\nu} c_{\mu, \boldsymbol{R}_\mathrm{j} \nu}(\boldsymbol{k}_\mathrm{f}) e^{i \boldsymbol{k}_\mathrm{f} \cdot \boldsymbol{R}_\mathrm{j}} \langle \boldsymbol{0}, \nu | \boldsymbol{k}_i \rangle, \tag{3.62}$$

where $\langle \boldsymbol{0}, \nu | \boldsymbol{k}_\mathrm{i} \rangle$ is nothing but a Fourier transform of real hydrogen-like atomic wave function and can be split into a radial $f_\nu(k_\mathrm{i})$ and angular part $Y_\nu(\theta_{\boldsymbol{k}_\mathrm{i}}, \phi_{\boldsymbol{k}_\mathrm{i}})$ [111] which can be expressed as

$$\langle \boldsymbol{0}, \nu | \boldsymbol{k}_\mathrm{i} \rangle = f_\nu(k_\mathrm{i}) Y_\nu(\theta_{\boldsymbol{k}_\mathrm{i}}, \phi_{\boldsymbol{k}_\mathrm{i}}). \tag{3.63}$$

Angles $\theta_{\boldsymbol{k}_\mathrm{i}}$ and $\phi_{\boldsymbol{k}_\mathrm{i}}$ define a direction of $\boldsymbol{k}_\mathrm{i}$ with respect to the original axis, k_i is the amplitude of the initial wave vector. The angular part $Y_\nu(\theta_{\boldsymbol{k}_\mathrm{i}}, \phi_{\boldsymbol{k}_\mathrm{i}})$ has the same form as the radial part of the corresponding orbitals [112], whereas the radial part is expressed using Gegenbauer polynomials (for more details see appendix B.3). The final expression for the matrix elements can be expressed as

$$M_{\mathrm{fi},\mu} \propto \boldsymbol{e} \cdot \boldsymbol{k}_\mathrm{i} \sum_{\boldsymbol{R}_\mathrm{j}} \sum_{\nu} c_{\mu, \boldsymbol{R}_\mathrm{j} \nu}(\boldsymbol{k}_\mathrm{f}) e^{i \boldsymbol{k}_\mathrm{f} \cdot \boldsymbol{R}_\mathrm{j}} f_\nu(k_\mathrm{i}) Y_\nu(\theta_{\boldsymbol{k}_\mathrm{i}}, \phi_{\boldsymbol{k}_\mathrm{i}}) \tag{3.64}$$

has two parts, $\boldsymbol{e} \cdot \boldsymbol{k}_\mathrm{i}$ which is determined by the polarization of the emitted light (which is not distinguished in experiments), and a part dependent on initial and final wave

functions. The former is not treated here and will be assumed to be constant (or slowly varying between the measurements with different angles of electron incidence). Treatment of the $\boldsymbol{e} \cdot \boldsymbol{k}_{\mathrm{i}}$ factor for different light polarizations is presented in Ref. [110], Ref. [106, 113] show that the radiation from metallic surface states can be well approximated by dipole radiation. The latter is treated here for unoccupied σ^* bands in graphene which were previously discussed.

Chapter 4

Computational Results

4.1 Band Structure Calculations

Using parameters for the TB Hamiltonian found in Ref. [35] and Ref. [52], band structures of graphene along high symmetry lines were simulated and are presented in figures 4.1a) and 4.1b), respectively. The Γ point corresponds to $|\boldsymbol{K}_{\parallel}| \sim 1.7\,\text{Å}^{-1}$.

The two sets of parameters make the bands behave quite differently and place the unoccupied sigma bands (dark blue) at different energy levels. The first set of parameters shows the minimum of the σ^* bands at approximately 4 eV at Γ, whereas the minimum is at 8 eV in the case of the second set of parameters. This difference stems from parametrization of the TB model which was determined by fitting the bands either to experimentally observed or *ab initio* calculated. The character of the bands is however the same.

Figure 4.1c) shows a graphene band structure calculated from first principles [34]. The shaded area shows a continuum of states, whereas red lines show states where symmetry properties could be identified. The two states between Γ and K labelled A_1 and B_1 were identified as sigma bands, stemming only from interlayer s, p_x and p_y orbitals. Hence the origin corresponds to the origin of TB σ^* bands as will be discussed later.

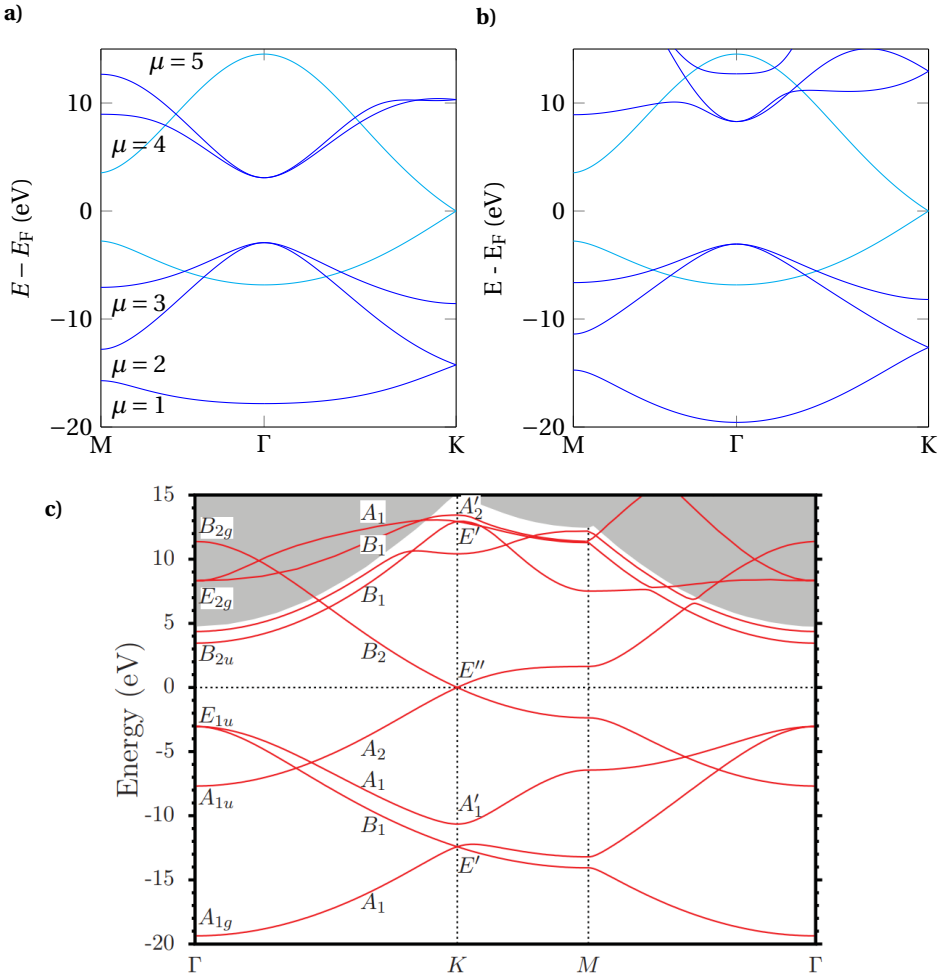

Figure 4.1: Graphene band structure calculated by a TB model in a) and b) and a band structure calculated from first principles c) adopted from Ref. [34]. In a) and b) σ bands are denoted by dark blue (and numbered $\mu = 1..5$), whereas π bands are denoted by light blue. It can be seen that both parametrizations place the lowest unoccupied σ^* bands to different energies with respect to the Fermi level (approximately 4 eV and 8 eV). The first principle calculations place the position of the lowest unoccupied σ^* bands to approximately 8 eV (denoted by A_1 and B_1 within the shaded area) to a continuum of states (shaded area).

4.2 Self-Energy and the Spectral Function

The results of the self energy calculations accounting for strong electron-phonon coupling to TO phonon mode are displayed in the figure 4.2c). In order to account for

effects of impurity scattering and electron-electron interactions, the self energy offset was set to $\Sigma_0'' = 100\,\text{meV}$, as previously mentioned.

To visually illustrate the effects of self-energy on the spectral function, a parabolic approximation of the bare σ^* band in the vicinity of the Γ point based on the DFT calculation found in Ref. [37] was used. Figure 4.2a) shows the spectral function in the absence of electron-phonon coupling, whereas figure 4.2b) shows the same with strong electron-phonon coupling included. The kink is clearly visible, similar to the occupied bands (figure 2.8). The minima was shifted to $E = 0\,\text{eV}$ by introducing a constant energy shift E_σ.

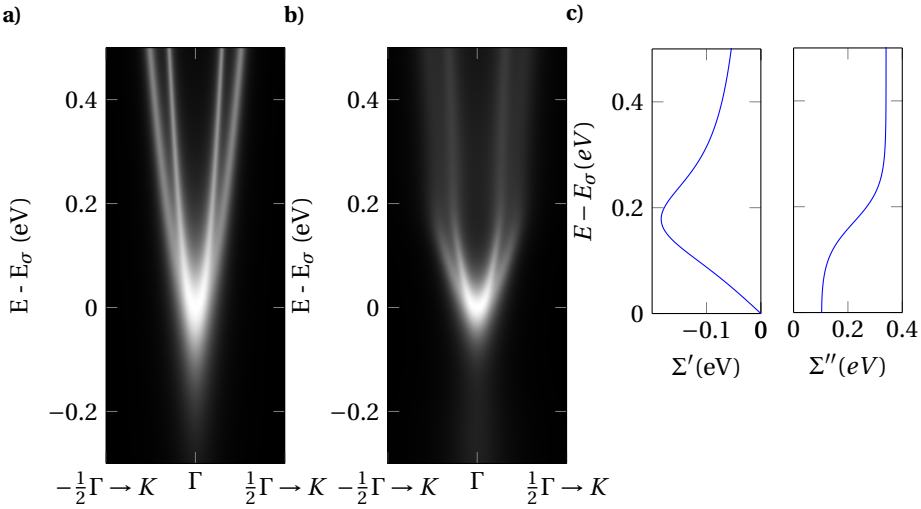

Figure 4.2: Effects of the self energy on bare band structure. Panel a) shows two sigma bands in the Γ to K direction. The bands were approximated by a parabolic dispersion corresponding to DFT calculations according to Ref. [37]. The effects of inter-band electron-phonon coupling results in the typical kink b). The real and imaginary parts of the self energy are shown in the panel 4.2c). Intense features are marked white. $\frac{1}{2}\Gamma \rightarrow K$ corresponds to $|\boldsymbol{K}_\parallel| \sim 0.85\,\text{Å}^{-1}$.

4.3 Matrix Elements

Figure 4.3 shows results of the $|M_{\text{fi},\mu}|^2$ simulation based on previously presented TB model for two lowest unoccupied σ bands ($\mu = 4,5$). One of the bands has matrix elements equal to 0 for all values of $\boldsymbol{k}_\parallel$ towards K and hence should disappear from the spectra. The second band is zero at Γ and increases towards K. This means that there should be no measured intensity for the normal electron incidence, considering a per-

fect instrument (infinite resolution). The results are calculated from the first set of TB parameters according to Ref. [35]. The second set of parameters [37] revealed very similar results and is therefore not included.

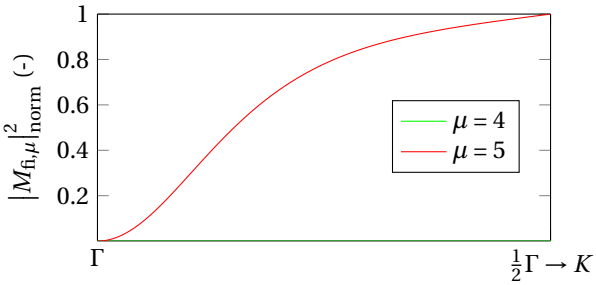

Figure 4.3: Normalized magnitude of $|M_{\mathrm{fi},\mu}|^2$ of the two lowest unoccupied σ^* bands. One of the bands vanishes for the whole spectra, whereas the second one has just non-vanishing intensity the Γ point. $\frac{1}{2}\Gamma \rightarrow K$ corresponds to $|\boldsymbol{K}_{\parallel}| \sim 0.85 \text{Å}^{-1}$.

4.4 The Total IPES Spectrum

Figure 4.4a) shows the impact of matrix elements on the expected spectra from the two lowest σ^* bands . Figure 4.4b) extends the simulation to account for energy and momentum broadening due to the measuring apparatus (Δ). Even if the effects of the apparatus are included, no visible peak should be present in the spectra at normal electron incidence.

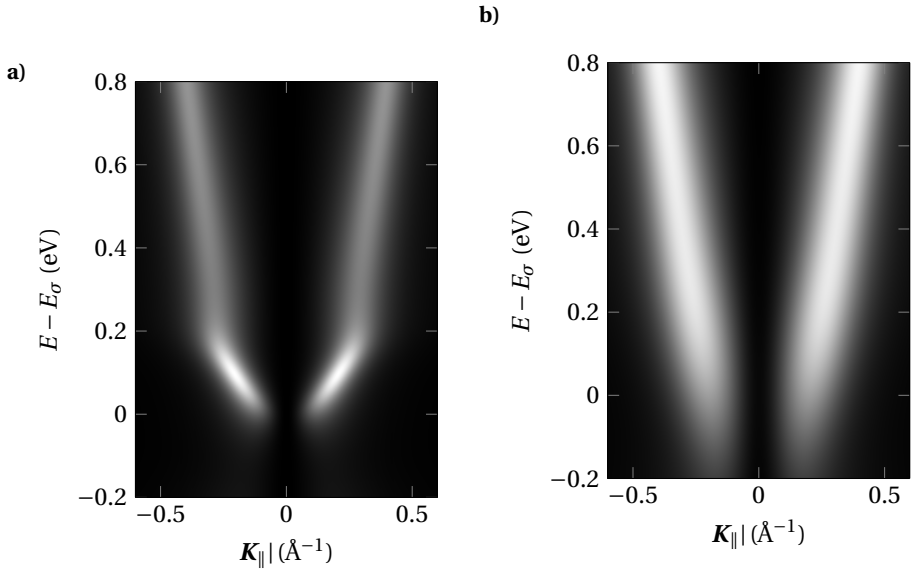

Figure 4.4: Simulation of expected KRIPES spectra for the two lowest unoccupied σ^* bands in the Γ to K direction including strong coupling to optical phonons and matrix elements without instrument broadening a) and with instrument broadening b). Intense features are marked white.

Chapter 5

Experimental and Analytical Methods

As was briefly mentioned before, the final measurements of graphene could not be performed in the NTNU laboratories due to poor energy resolution of the instrument. Experimental work was therefore carried out at the Physikalisches Institut, Münster within the group of Prof. Dr. Markus Donath. The methods related to the characterization of the IPES instruments are given in the first two sections. Even though they are discussed in connection to the NTNU apparatus (manual available from Ref. [81]), the same methods can be (and are) used for experimental characterization of all IPES instruments. First, a characterization of the electron beam and its divergence is presented in the first section, followed by an energy resolution characterization. The last section then focusses on the actual experiment performed on graphene.

5.1 Characterization of The Electron Beam

As discussed in section 3.3.2, the instrument is characterized by its resolution function

$$D_{\text{tot}}(E) * A_{\text{beam}}(\boldsymbol{K}_{\parallel}),$$

which consists of two independent parts, a total energy resolution function of the apparatus $D_{\text{tot}}(E)$, and $A_{\text{beam}}(\boldsymbol{K}_{\parallel})$ which stands for an uncertainty of $\boldsymbol{K}_{\parallel}$ due to electron beam divergence. This will be the focal point of this section.

In order to achieve the best resolution in $\boldsymbol{K}_{\parallel}$, the electron beam has to be as parallel as possible (in other worlds, the divergence of the beam as low as possible). Due to the low energy electrons present in IPES the electron beam is strongly effected by their repulsive forces and also by any magnetic/electric fields. Moreover, the final width of

the electron emitter also contributes to the beam divergence. This section presents a method how the best working conditions regarding the momentum broadening of the electron gun can be found.

5.1.1 Experimental Method

The simplest and most commonly used method to characterize the electron beam is based on the Faraday cup. The whole measurement device consists of a Faraday cup with a slit in the upper plate and a collecting plate inside the cage. The slit is swept through the electron beam and an electron current is measured on the collective plate. Once the beam profile is known for different positions of the electron gun, an analysis can be performed in order to find the divergence of the electron beam. This method is schematically depicted in figure 5.1a).

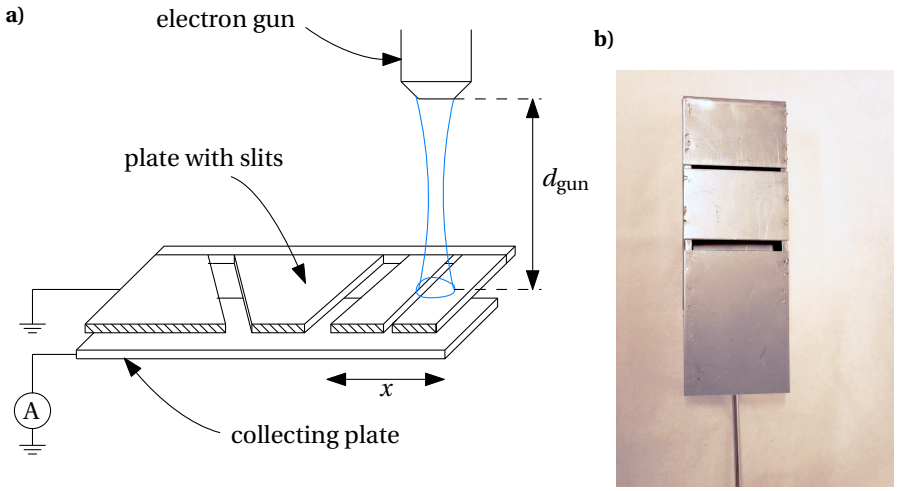

Figure 5.1: Schematic picture of the Faraday cup with slits in the upper plane a) and a view of the final realization b) with 1 mm and 3 mm slits. The slit present in the upper plate of the Faraday cup is swept through the electron beam. Electrons which pass through are then collected on the inner plate where the current is measured.

5.1.2 Realisation of the Experiment

In figure 5.1b) a final realisation of the Faraday cup is shown. For the experiment just the upper slit with width of 1.02±0.04 mm was used. The position of the slit x was measured by a calliper attached to a moving flange where the slit was mounted. The calliper was aligned with the axis of the flange within 5° which gives a systematic relative measurement error of 0.4 % in the position measurement. Since the error can be seen as

constant for the small distance range used within the measurement, the effects are on the further analysis are small and are neglected.

The position of the slit was manually adjusted by moving the flange 0.2 mm for every step, and the current was read by a nano-ammeter for every corresponding position. After the sweep through the full range of interest, either the gun position or the voltage on the focus element (referred to as the focus) was changed and the whole sweep was repeated. Due to this enormously time consuming method, every sweep was performed just once. All measurements were performed in UHV with pressures below 2×10^{-9} mbar. The filament current was set to 1.07 eV for all the measurements. The whole experiment was performer in the preparation chamber.

As mentioned previously (section 2.3.3), the electron gun is a very simple pervatron type emitter with a BaO cathode.

5.1.3 Fitting Procedure

In order to fit the data and determine the uncertainty of the measurement, the procedure described and used in Ref. [114] and Ref. [115] is used in the following[1]. To illustrate the procedure, the figure 5.2 will be used.

From the set of the original data points (black dots), new data points (red dots) are generated with a distribution around the original data points corresponding to their uncertainty (the distribution is denoted by grey curves). The newly generated data points are then fitted with a corresponding function (red curve). The curve data is saved and the whole procedure is repeated again. In order to get a reasonably robust statistical performance, 10000 repetitions were performed. As a result, a summary of the statistical fitting parameters is obtained and a mean value and standard deviation can be found.

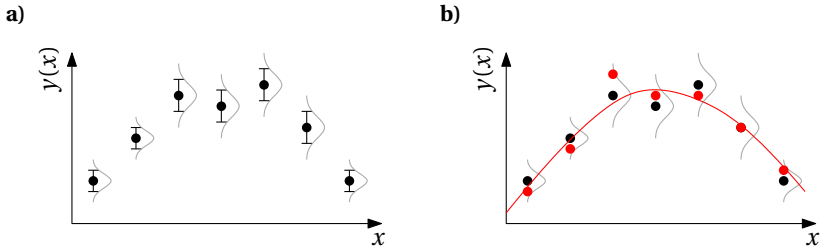

Figure 5.2: Schematic of a fitting procedure. The original data (black dots) are modified according to uncertainty distribution (grey). The new points (red dots) are randomly generated within a distribution and then fitted (red solid line).

[1] The fitting procedure was successfully used to detect a position of the peaks in IPES measurements in Ref. [114] and Ref. [115] with resolution better than the resolution of the instrument.

5.1.4 Electron Beam Divergence and Momentum Uncertainty

Before the actual beam divergence could be calculated, a FWHM of the electronic beam at different positions of the gun had to be determined.

Similarly to the previously described fitting procedure, the position of the original data was modified according to the calliper accuracy (0.03 mm) and the new data were numerically deconvoluted to account for the final width of the slit. Consequently, the FWHM was determined from a parabolic interpolation of the deconvoluted data[2]. This procedure was again repeated 10000 times in order to obtain robust results.

The newly obtained FWHM were then fitted with a polynomial function by applying the procedure discussed in the previous section. Finally, the divergence angle together with its standard deviation were determined from the differentiation of the polynomial. The divergence angle was then used for a calculation of uncertainty in $\boldsymbol{K}_{\parallel}$ using the conservation laws from previous chapters.

Note that in the analysis, the uncertainty of the current measurements and the electron gun position measurement were neglected, having much smaller effects on the beam divergence angle uncertainty than the measurement of the slit position and slit width.

5.2 Characterization of Apparatus Energy Resolution Function

In this section, second part of the total resolution of the experimental apparatus, $D_{\mathrm{tot}}(E)$, is treated both experimental and analytical methods are presented.

5.2.1 Experimental Methods

To measure the energy resolution of the apparatus D_{tot}, two different methods can be used. The first method utilizes the IPES measurement of an isolated state which is sharp in comparison to the Apparatus function, such as the surface states of Cu(100) [116, 117], whereas the other method is based on IPES measurements of the Fermi edge in metals[3]. Due to the apparatus resolution function both the image-potential states and the Fermi edge are broadened which can be used for instrument characterization.

[2] The parabolic interpolation was used in order to characterize the beam profile as closely as possible. Note that several different methods, including linear interpolation and polynomial fitting were accedes. Gaussian fitting could not be reliably used due to the shape of the profile.

[3] The exacted curve should correspond to $1 - f(E - E_{\mathrm{F}})$ considering constant density of states which is a good approximation for Ag and Au and was used before in Ref.[109, 118]. $f(E)$ is the Fermi distribution to account for final temperature.

5.2.2 Realisation of the Experiment

In order to have a direct comparison to the specification sheet of the instrument, measurement of the Fermi edge of polycrystalline silver was performed. Within the regions around the Fermi edge, the density of states of Ag is non-zero and approximately constant [119, 120] and so the effects on the shape of the Fermi edge are neglected.

The sample was glued to the sample holder by a silver glue paste(EO-TEK H21D) cured at 120 °C for 15 min. Before the experiment, the surface was sputtered[4] by argon to obtain a clean surface. The sputtering was done at 3 kV bias at an argon pressure of 10^{-6} mbar for 1 h. For the measurement, the electron gun approximately 25 mm from the sample with 30% focus, the sample current was set to 12.2 mA at 20 eV with an electron filament current of 1.09 A.

As mentioned in section 2.3.3, the detector is a simple NaCl coated Ta solid-state detector with a CaF_2 window.

5.2.3 Analytical Method

To find the energy resolution of the apparatus, the measured data were fitted with a polynomial within the region of ±1.5 eV around the Fermi Edge. Consequently, a trial resolution function was created and convoluted with a Fermi edge of 300 K (which accounts for the broadening due to finite temperature). The result was then compared to the polynomial fit and the trial function was modified accordingly. The whole procedure was repeated until a good match was obtained[5].

The whole analysis was not automatized due to the presence of convolution, but was performed manually. The results cannot be expected to be perfect, but should provide the necessary information about the total apparatus energy resolution function.

5.3 Graphene Measurements

As mentioned before and as will be shown in the results, energy resolution of the NTNU instrument is too poor to be able to properly distinguish the band character and possibly further investigate many-body effects. Fortunately, the experiments could be performed at Physikalisches Institut, Münster within a group of Prof. Dr. Markus Donath.

[4] Sputtering is process where particles are ejected from a solid sample which is bombarded by high energy particles.

[5] The difference between the fitted polynomial and the obtained curve was measured around the Fermi edge (±1 eV) and was required not to exceeded 2 % of the maxima of intensity within the investigated region.

5.3.1 Experimental Method

The instrument set-up at Physikalisches Institut, Münster has already been described in a previous work [121, 80], so only a brief discussion is given.

The electron beam is generated using a BaO cathode illuminated by a laser beam in order to provide the smallest emission spot possible. The beam is then lead through a 90° toroidal electrostatic deflector with a 1.5 mm slit aperture at the focal point which gives a beam divergence of ±1.5° corresponding to $\Delta \boldsymbol{K}_{\parallel} \approx 0.06\,\text{Å}^{-1}$ at the Fermi level. The system includes 4 independent Geiger-Müller counters working as bandpass detectors at a fixed mean energy of 9.9 eV with ΔE_{tot} =350 meV and a Gaussian-shaped energy resolution function. Even though two of the detectors were equipped with heated CaF_2 and possible improvement of resolution was available, the final $\boldsymbol{k}$-resolved experiments were performed using only one detector with ΔE_{tot} =350 meV due to several detector problems[6]. All the measurements were taken using a detector placed at 70° from the sample surface normal at normal electron incidence.

The sample, ML graphene on 4H-SiC(0001) [7] was clamped to a sample holder and directly transported into the chamber. It was first annealed (heated) at approximately 300 °C over 9 hours (overnight) and did show a recognisable LEED pattern [124], however, no states were observed. The sample was then annealed again at temperature slightly above 500 °C (which was believed to be sufficient [125]). During the annealing processes, the pressure was kept below 1.8×10^{-8} mbar to prevent a contamination of both the sample and the chamber. Unfortunately, due to problems with manipulators and sample holders, there was no other method to properly investigate the surface quality.

After the LEED measurement, IPES could be measured. All IPES measurements were performed with a pressure better than 4×10^{-10} mbar and the measurement was performed on a symmetry line between Γ and K.

5.3.2 Analytical Method

In order to analyse the data and the parameters of every peak, each measured spectrum was normalized with respect to its maximal value and consequently fitted with Voigt profile (Lorentzian convoluted with a Gaussian curve). For the fitting procedure, the technique described in section 5.1.3 was used which allowed the determination of both peak position, peak width, relative peak height and standard deviations.

[6] One of the counters was not installed, moreover, the main high-efficiency counter was not working properly and could operate reliably for just a couple of hours which was not sufficient for the measurements and had to be disregarded from the data analysis. In order to obtain the best possible number of photon counts, it was decided to measure with lower resolution due to dramatic reduction of count rate for lower values of ΔE_{tot} [122, 121, 123]

[7] The sample was a commercial sample from Graphensic. According to the documentation and scanning probe microscopy, the sample was 97.9% mono-layer, 2% double-layer and 0.1% tri-layer.

Chapter 6

Experimental Results

The results presented in this chapter are all determined using methods described in the previous chapter. In the first section measurements of the NTNU apparatus are presented. The second section presents results from IPES measurements of graphene.

6.1 NTNU Apparatus Characterization

6.1.1 Electron Beam Measurements

In figure 6.1 and 6.2 sample measurements of the electron beam profile for electron energies 6 eV and 12 eV are shown respectively. The measured current was normalized for simple visualisation. The beam is not well shaped for low energies and diverges rapidly. For higher energies, the divergence is not as rapid as for the low frequencies and the beam is preserved even for distances around 30 mm, which is beyond the recommended working distance (25 mm according to the manual [81]). It can be observed that the beam profile moves towards higher values of x, for 30 mm gun distance and 12 eV the shift is around 1 mm. Moreover, the beam profile is not symmetric and does not have a Gaussian shape. In general, the asymmetry gets larger with increasing focus value.

The resulting FWHM for energies 6, 8, 10 and 12 eV are displayed in figure 6.3 by dots. The solid lines are polynomials fitted to guide the eye. Different colours correspond to different focus values. It can be seen from the figure that the beam diverges rapidly for low energy electrons, whereas it stays fairly constant for higher energies. Moreover, the width in the vicinity of the focus (minimal value of FWHM) seems to correlate well with the focus value, where for higher focus values FWHM generally increases. However, an exception exists at 10 eV and 30 % focus. The uncertainty of the measurements was not included since its values were almost within the size of the dots.

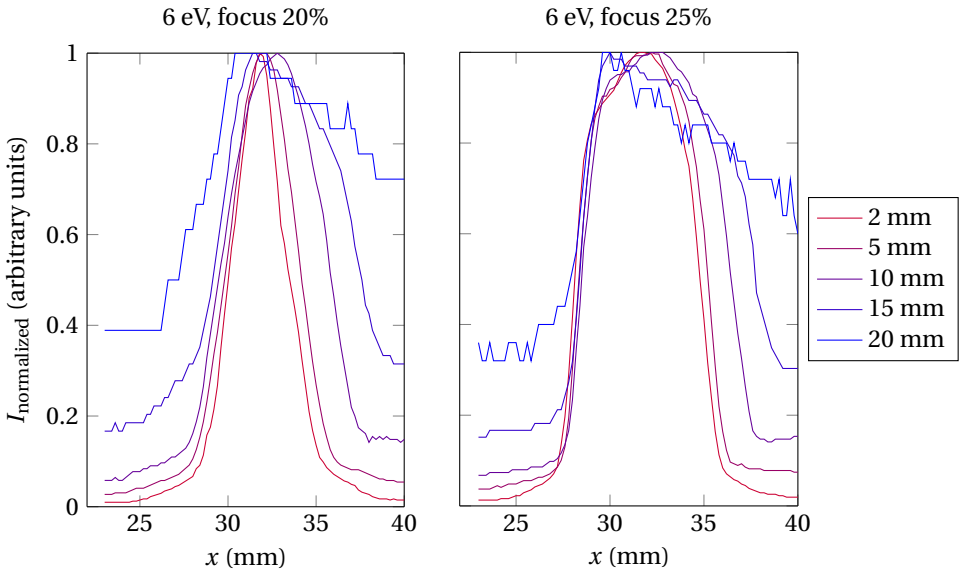

Figure 6.1: Measurements of the electron beam profile for kinetic energy 6 eV for different focuses as a function of slit position x. The beam diverges quickly, possibly due to electromagnetic fields in the chamber.

Standard deviations varied from 0.05 to 0.06 mm and it is mainly caused by the uncertainty in the slit position measurement (even though the slit with uncertainty was also included in the calculation).

The uncertainty of momenta parallel to the surface $\Delta \boldsymbol{K}_{\parallel}$ is shown in figure 6.4. It can be seen that the uncertainty of $\Delta \boldsymbol{K}_{\parallel}$ in general decreases with increasing energy which makes $\boldsymbol{k}$-resolved measurements at low energy states rather difficult. Moreover, the optimal working distance (where the solid lines cross 0) seems to increase with increasing electron energy. Using the previously described method, standard deviation was determined to range from 0.02 to 0.03 Å^{-1} within the region of interest. Due to the polynomial fit, the standard deviation increases drastically for close vicinity of the electron gun as well as for a far distance from the electron gun. A figure displaying standard deviation is attached in the appendix B.5.

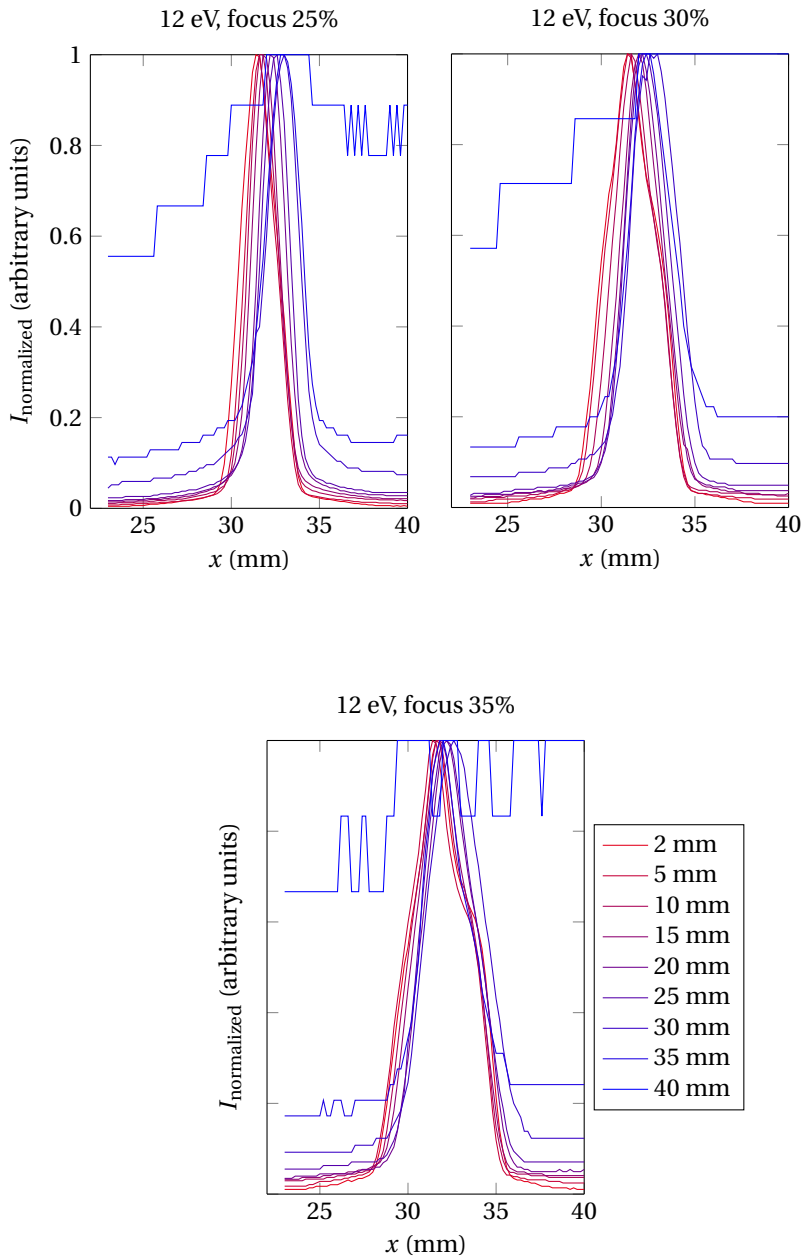

Figure 6.2: Measurements of the electron beam profile for kinetic energy 12 eV for different focuses as a function of slit position x. The beam profile maxima moves towards the higher x possibly due to a electromagnetic fields in the chamber or due to slightly tilted electron gun. The beam profile gets more asymmetric for higher values of focus.

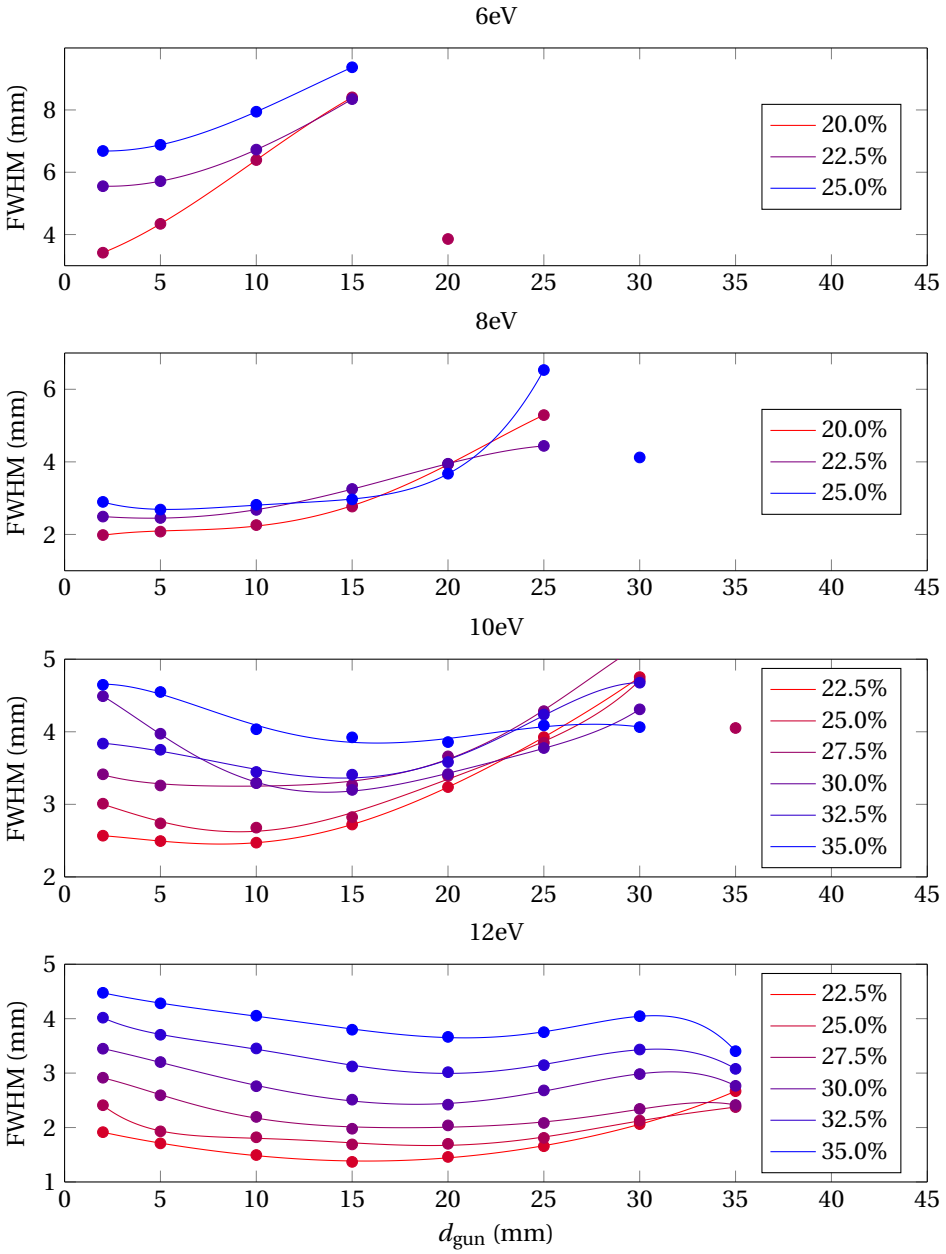

Figure 6.3: Calculated FWHM as a function of electron gun distance d_{gun} for different energies of the electron gun and different percentage of the focus knob. Dots denote measured data which are fitted by polynomials to guide the eye. The working range of the electron gun increases with the increasing energy of the electrons. The electron beam spot size generally increases with increasing focus value.

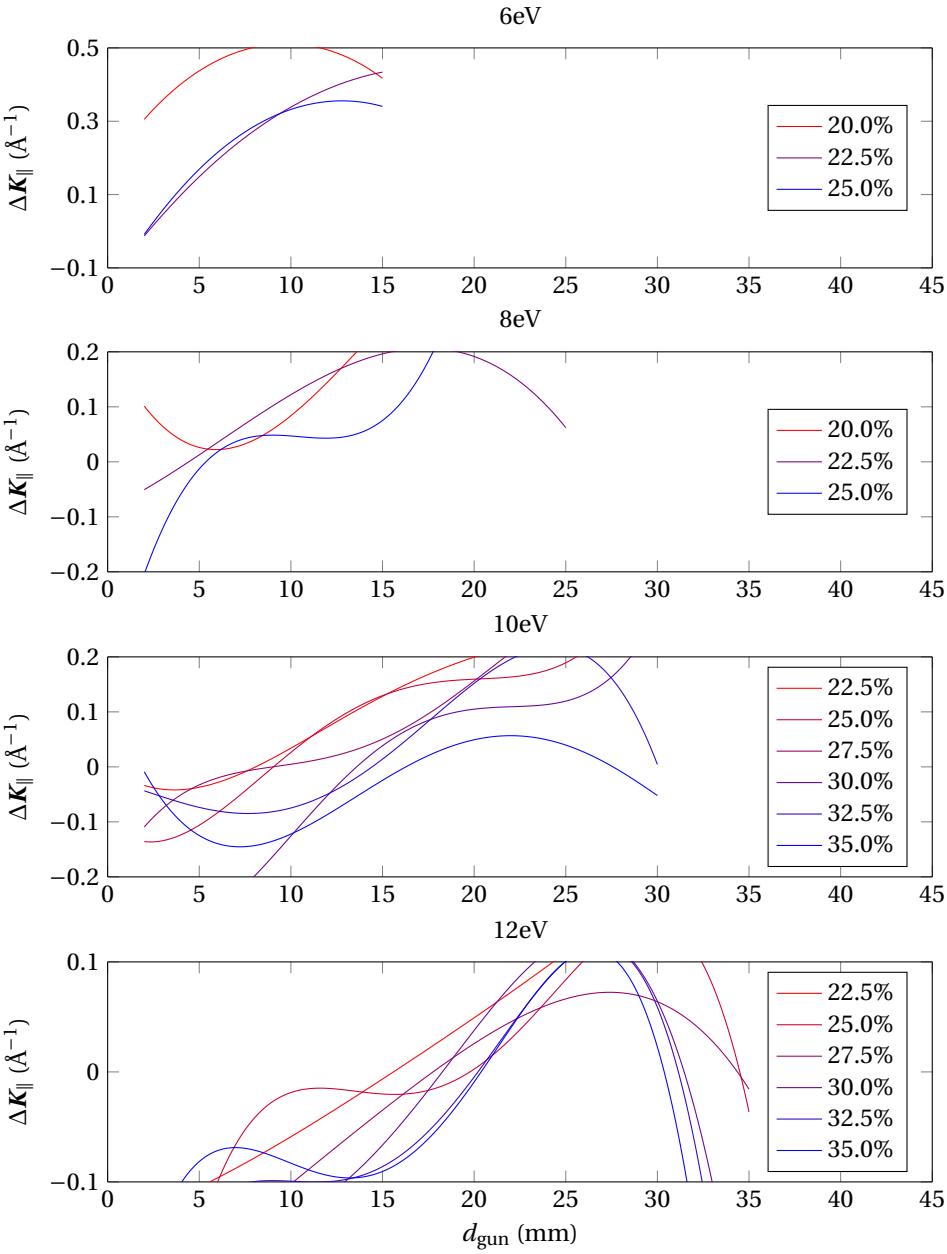

Figure 6.4: Calculated $\Delta \boldsymbol{K}_{\parallel}$ values. The $\Delta \boldsymbol{K}_{\parallel}$ as a function of electron gun distance d_{gun} for different energies of the electron gun and different percentage of the focus are shown. The solid lines denote different values of the knob. The optimal working range of the electron gun increases with the increasing energy of the electrons.

6.1.2 Energy Resolution

Figure 6.5a) shows the result of IPES performed on polycrystalline silver. The measured values are denoted by black dots (the solid line is just to guide the eye). The blue line shows a Fermi edge which can be expected at infinite instrument resolution and at temperature 300 K). The polynomial fit is displayed in green. The apparatus energy resolution function (figure 6.5b)) was determined by its convolution with the Fermi edge fitted to the polynomial (the convolution is denoted red in the figure 6.5a)). It can be seen that the energy resolution function does not have a purely Gaussian shape. FWHM was determined to be 0.88 eV which is about 0.2 eV more in comparison to the data-sheet of the instrument (see appendix B.4 for data-sheet analysis).

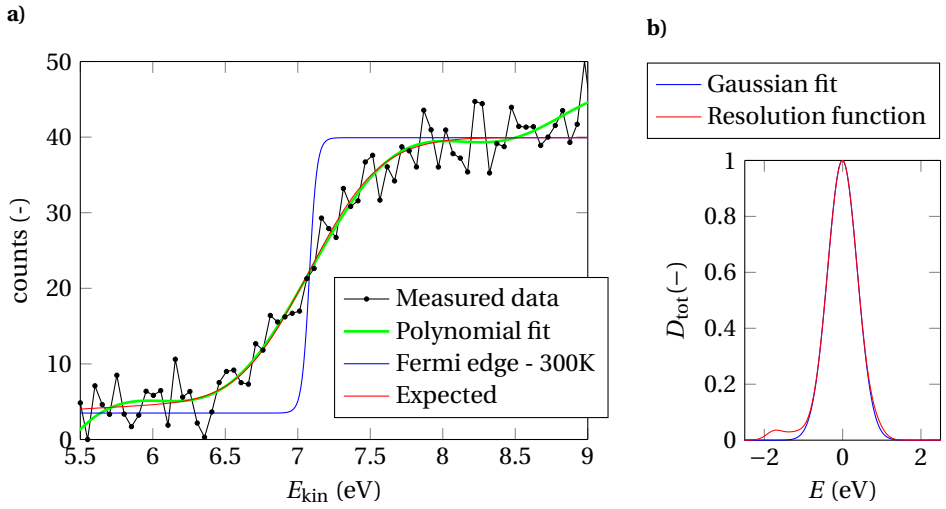

Figure 6.5: IPES measurement of Fermi Edge on polycrystalline silver (111) a) and apparatus energy resolution function b). Measured data (black dots) are fitted by polynomial (green) which is then fitted with a curve corresponding to the determined apparatus resolution function D_{tot} b) (red) which is convoluted with the Fermi edge (blue). The resulting convolution is depicted red.

6.2 Experiments on Graphene

6.2.1 LEED

The LEED pattern after the second annealing is shown in figure 6.6. It shows a typical Moiré pattern of graphene on SiC [126]. Dots present due to a presence of Si in SiC are denoted by black arrows. C corresponding to the creation of graphene is displayed by a red arrow.

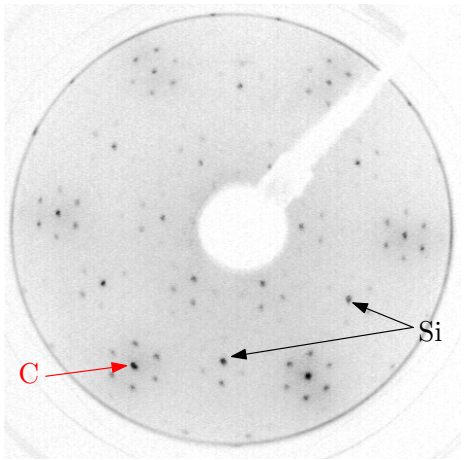

Figure 6.6: A negative of the LEED picture taken of the graphene sample at 99 eV. It shows a Moiré pattern typical for graphene reconstructed on SiC.

6.2.2 IPES

The preliminary measurements of graphene showed only one resolved peak at approximately 3.5 eV above the Fermi level which is shown in figure 6.7. Even for higher angles (along the high symmetry line towards K), the preliminary results did not show any other well resolved peaks (the possible reason will be discussed in the next chapter).

The following figure (Fig. 6.8) shows a measurement of the dispersion of the identified peak. The data for different angles (marked in the figure) were normalized to the highest measured counts of the corresponding measurement angle and plotted with increment 0.5 (-) in intensity for every following measurement[1]. The measurements were taken using a detector placed at 70° from the sample surface normal at normal electron incidence. The positions of both the electron gun and the detector ware fixed, which corresponds to the increasing detector angle for higher measured angles[2]. Error

[1] For an angle of 17°, the intensity scale is correct, for the angle of 7°, the intensity is shifted by 0.5 (-) up, for 5° by 1 (-) and so on.

[2] For instance, for sample measured at 7°, the detector angle was 77° from the sample surface normal.

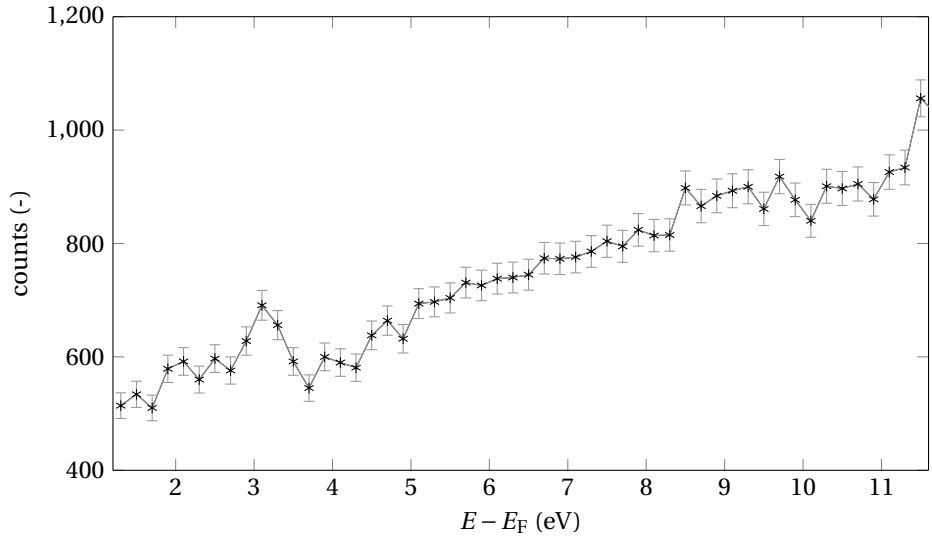

Figure 6.7: IPES measurement of ML graphene on 4H-SiC(0001) close to normal incidence. The only resolved peak was found at approximately 3.5 eV above E_F.

bars are not included to preserve clarity in the figure. Even from the raw data it can be seen that the intensity of the peak decreases towards higher angles. An angle of 17° corresponds to a detector axis of 87° degrees and so most of the incoming photons were screened by the sample and sample manipulator.

In order to see the dispersion of the peak and a change in the peak height (or width), previously described fitting procedures (see section 5.1.3) was used. The peak dispersion, normalized peak heights[3] and peak widths are shown in figure 6.9 and are denoted in blue, error bars for corresponding measurement points are included. The peak disperses from approximately 3.5 eV towards 3.9 eV for the angle -17° (~ −0.5 Å). It can be observed that the normalized peak height decreases towards negative values of $\boldsymbol{K}_\parallel$ and the intensity is not symmetric around zero. The width of the individual peaks varies slightly but is around 0.5 eV, which is more than the energy broadening of the instrument (350 meV).

[3] The values were normalized to the highest measured peak.

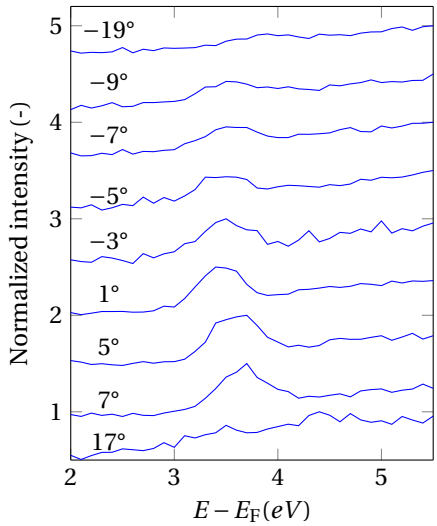

Figure 6.8: IPES measurement of the dispersion of the state localized at approximately 3.5 eV above Fermi level on graphene on SiC after annealing at 500 °C. One can see that the peak disperses towards higher energies for higher absolute value of the angle of electron incidence (noted above the corresponding IPES measurements) and its amplitude with respect to the background signal decreases.

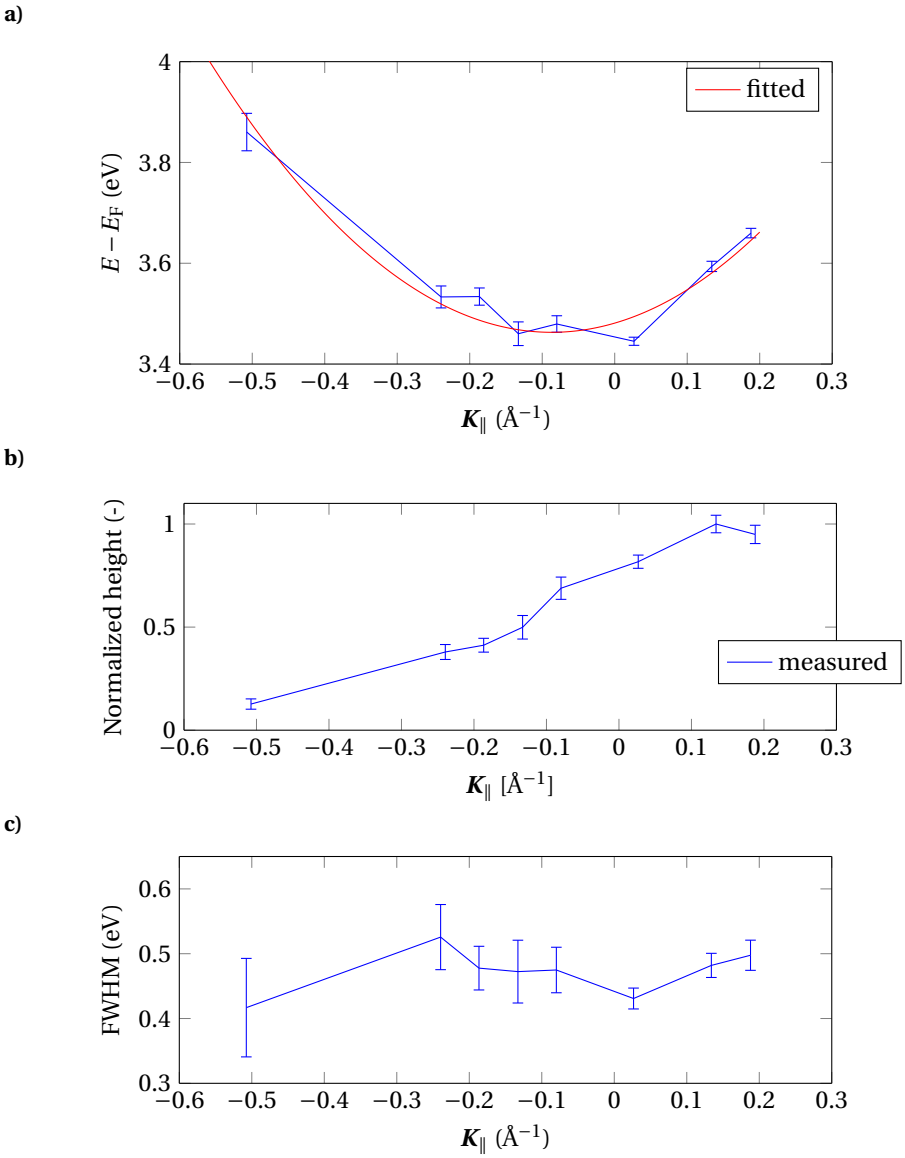

Figure 6.9: IPES measurements of the lowest observed graphene band. Peak dispersion a), normalized peak height b) and peak width c) are shown in blue (the blue solid line is just displayed to guide the eye, the measured points are displayed with error bars). In the panel a), fitted with a parabolic fit (red) to demonstrate the deviation of the data from the parabolic dispersion. From panel b) it can be seen that the normalized peak height is non-symmetric. The last panel (c)) shows FWHM of the measured peak which is bigger than the instrument broadening (0.35 eV).

Chapter 7

Discussion

7.1 Apparatus Characterization

7.1.1 Beam Profile

In section 6.1.1, the electron beam profile was measured for various positions of the electron gun and values of focus. The raw data showed an asymmetry of the beam profile and its positions shift with increasing distance of the electron gun.

The first apparent explanation of the position movement could be an electron gun which is tilted by a small angle with respect to the normal of the slit. Looking to the data for the 12 eV measurements, the position shift is about 1 mm for a gun distance difference of 23 mm. This would mean a tilt angle of 2° of the electron gun which is a reasonable value due to the high forces acting on the moving flange where the electron gun was mounted. However, for lower energies (8 eV and 10 eV) the tilt angle would need to be almost 3° which cannot be the case. In addition, this would not explain the asymmetry of the peak.

An alternative explanation can be found by looking back to the measurement set-up and remembering that low-energy electrons are strongly effected by magnetic/electric fields. The entire measurement process was performed in a preparation chamber which was not magnetically shielded. In the presence of a magnetic field, a moving particle will experience a Lorentz force and consequently, the trajectory of the particle is modified. This would also explain the asymmetry of the beam if one considers a non-homogeneous magnetic field present in the chamber.

The last, most probable explanation can be the construction of the electron gun itself which does not have to be symmetric. From the data it can be clearly seen that the asymmetry gets larger for higher values of the focus which suggests that the focusing coil inside the electron gun can could be non-symmetric or damaged.

In order to further determine the reasons of the asymmetry and the beam position shift, the electron beam profile should be checked in a magnetically-shielded chamber when possible. If the asymmetry is still present, the electron gun should be subjected to deeper investigation.

7.1.2 Momentum Uncertainty

The momentum uncertainty was presented in figure 6.4, together with the FWHM in figure 6.3. The figures show that the electron gun cannot be easily used for the lowest energies around 6 eV with a good momentum resolution; either the spot size is too big or the beam diverges rapidly. The figures show that the optimal working distance of the electron gun increases with increasing energy. As a consequence, $\boldsymbol{k}$-resolved measurements should be performed within a short energy range with ideal electron gun set-up. If a long energy range is needed, the measurements should be split into several parts while adjusting the gun between the measurements. An ultimate solution would be an automate the procedure adjusting everything automatically.

The results suggest that the electron gun can be used in a regime with $\Delta\boldsymbol{K}_\parallel = 0.0 \pm 0.6\,\text{Å}^{-1}$. However, this need further discussion. The method which was used did not account for the asymmetry of the electron beam, moreover, the electrons ware considered to have laminar flow behaviour[1]. This picture is rather crude, however, it was successfully used in Ref. [80] and should provide a good estimate. If a classical picture with non-interacting electrons is used, the worst situation which can possible occur is an electron with a trajectory from the left of the electron gun opening to the right side of the sample. For 12 eV, 25 % focus and a working distance of 25 mm, $\boldsymbol{K}_\parallel$ of the electron would be around $0.1\,\text{Å}^{-1}$. This is rather unlikely. If a more realistic picture was used, electrons having straight random trajectories within the beam profile, $\boldsymbol{K}_\parallel$ would be about half of that value and $\Delta\boldsymbol{K}_\parallel \approx 0.1\,\text{Å}^{-1}$. The value would correspondingly scale up with a bigger electron beam spot size and shorter working distances.

It can be concluded that in order to reach the best $\boldsymbol{k}$-resolved result, the electron beam spot size should be kept as small as possible while maximizing the working distance and while keeping the electron beam parallel ($\Delta\boldsymbol{K}_\parallel = 0.0\,\text{Å}^{-1}$ according to figure 6.4). With this optimal set-up, $\Delta\boldsymbol{K}_\parallel < 0.1\,\text{Å}^{-1}$ should be achievable.

7.1.3 Energy Resolution

The FWHM was determined from figure 6.5 to be 0.88 eV which is about 0.2 eV more than the data-sheet of the instrument shows (see appendix B.4). The difference is probably caused by low power in the statistical analyses of the actual measurement. In several consequent measurements, the results were getting worse with the increasing

[1] In other words, the trajectories of the particles were not crossing each other.

number of measurements. This was attributed to surface degradation. Moreover, both the filament current and the sample current were relatively high (1.09 A and 12.2 mA at 20 eV, respectively), which has a direct impact on the electron beam shape and its energy spread[2]. In addition to the high value of the FWHM, the energy resolution function does not have a Gaussian shape which can significantly complicate analysis of the results.

The findings in this section correspond well to the previous work presented in Ref. [83], where a similar solid state detector was used (Na). This makes the IPES system at the NTNU lab not suitable for the intended measurements - for instance, two image potential states would not be resolvable from each other.

7.2 Model Justification

The simulation of the expected IPES spectra as described and performed in Chapters 3 and 4, respectively, were based on a TB model of graphene. The two different sets of parameters placed the minima of the two lowest σ^* bands at Γ to very different energies (4 and 8 eV). Moreover, the shape of the bands very roughly approximates the results of the *ab initio* calculations found in the literature. Therefore, a discussion about a validity of the TB model for the purpose of this work has to take place.

Recently, a study showing band character of graphene bands was published [33] and which was used for model validation. Figure 7.1b) shows a band structure calculated from first principles and figure 7.1a) depicts the corresponding band character. It both figures, zero energy was assigned to the lowest unoccupied state at Γ (which is not the σ^* band). Looking back at figure 7.1b), two states at approximately 5 eV at Γ with just a p_x- and p_y-character can be seen (marked blue). Connecting this to the corresponding band structure calculation, 2 states with a shape of the unoccupied σ^* bands can be seen. This is also supported by a band structure calculation presented in the second chapter and performed in Ref. [34]. From figure 7.1a) it can be seen that the bands almost purely originate from p_x and p_y orbitals.

In order to confirm the character of the σ^* bands in the TB model, a sum over the projection of corresponding σ^* band wave functions to p_x and p_y orbitals ($\sum_{p_{xy}} \equiv \sum_{\boldsymbol{R}'_j,\mu=p_x,p_y} c_{\mu,\boldsymbol{R}'_j\nu'}$) and s orbitals ($\sum_s \equiv \sum_{\boldsymbol{R}'_j,\mu=s} c_{\mu,\boldsymbol{R}'_j\nu'}$) is shown in figure 7.2a). The projection to p_x and p_y orbitals is non-zero at Γ and is within the range of 1.5 to 2.2 for both bands (denoted by subscript $\mu = 4,5$ in the TB calculation). The projection to s orbitals is zero at Γ and just slightly increases towards K for both states. This results in a p_x- and p_y-like character of the corresponding σ^* bands. In other words, it is in good agreement with first principle calculations (Fig. 7.1a)). Note that the analysis is only

[2]The divergence of the electron beam is increased with higher sample current due to stronger repulsive forces between the electrons. As a result, broadening in energy can be present due to averaging over certain $\boldsymbol{K}_\parallel$ regions. The energy spread of the bean then increases with higher temperature of the emitter.

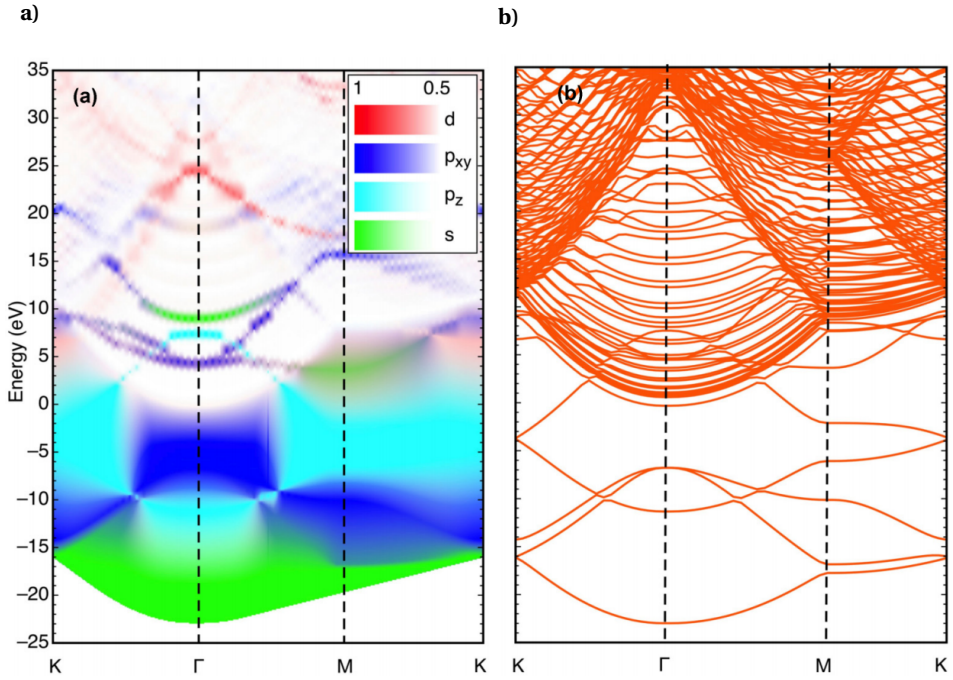

Figure 7.1: Band structure character a) and corresponding band structure calculation b). The energy range is shifted so that zero corresponds to the energy of the lowest unoccupied state at Γ. The lowest σ^* bands with minimum of 5 eV (approximately 9 eV above the Fermi level) have mostly p_x and p_y character (blue marked states in panel a)). Both plots are adopted from Ref. [33].

shown for the first set of parameters (presented in figure 4.1a)), but a very similar result was obtained for the second set of parameters (resented in figure 4.1c)).

Another justification has to be made regarding the assumptions made during the calculation of matrix elements. For the derivation of the final IPES intensity a three-step model and an assumption about slow variations of matrix elements with energy was used. The three-step model was already shown to closely match the experiments both within the framework of the PES [28, 29, 92] and the IPES [105]. Moreover, the model, including the assumption about slow variations of matrix elements was also proven to match PES experiments of occupied σ bands both related to graphene and graphite [28, 29, 92, 125]. Due to the same origin of the σ and σ^*, time-reversal symmetry of IPES and PES processes[3] and small energy range of the simulations, the same validity of results can be expected using the model within the IPES.

[3] As discussed in Ref. [67] and mentioned in section 2.2, both processes can be seen as a time-reversal of each other in an application in solids.

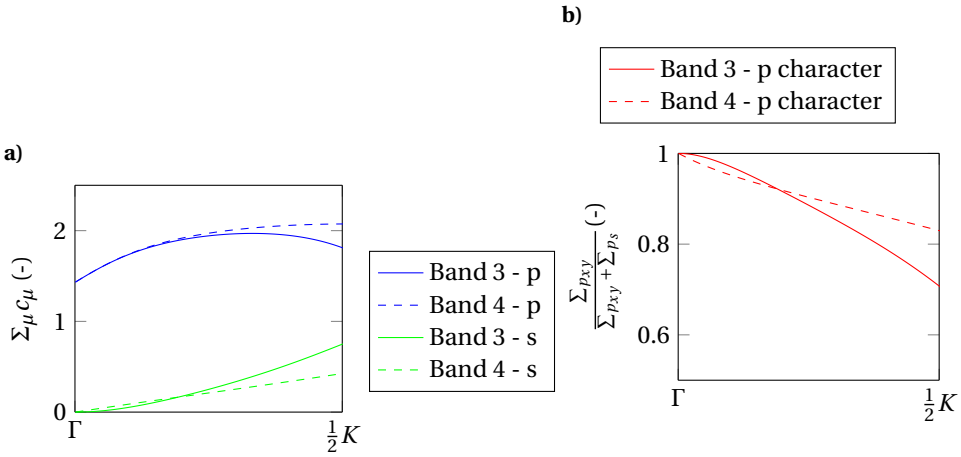

Figure 7.2: Sum over the projection σ band wave function into p_x and p_y (blue) and s orbitals (green) a) and corresponding p-like band character of the σ orbitals b) with the same parametrization as in Fig. 4.1a). Projection into p_x and p_y is dominant and both σ bands are almost p-like which is in good agreement with previously published first principle calculations.

As briefly mentioned in section 3.3.4, a free-electron like initial state can be assumed due to a presence of a continuum of states above the vacuum level [34]. This can also be seen from figure 7.2b) where free-electron bands are present between approximately 10 and 20 eV. Moreover, the origin of the bands is not well resolved (see figure 7.2a)) which also supports the assumption of a free-electron-like initial state. This comes from the initial fee-electron like state described by a plane wave, which can be further expanded into a series of spherical harmonics (in other worlds, it is a combination of different atomic orbitals).

7.3 IPES Graphene

Results presented in figure 6.7 showed a single resolved peak at approximately 3.5 eV above the Fermi level. The result is very different from the spectra measured on ML graphene (MLG) on 6H-SiC obtained in Ref. [39], where a very distinct peak was also measured at approximately 6 eV above E_F (see figure 7.3). However, this peak (denoted by C) was attributed to the presence of Si vacancies in the topmost layers of the substrate[127]. Due to a different polytype of SiC and hence different layer stacking and structure, this peak can be missing in 4H-SiC. The first peak was assigned to the unoccupied σ^* band.

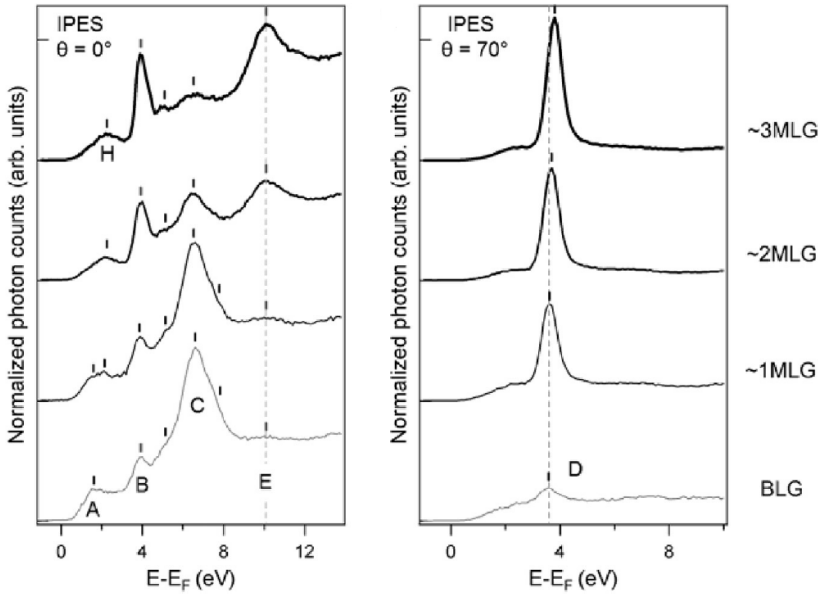

Figure 7.3: IPES measurement of 6H-SiC substrate (BLG), together with ML, BL and TL graphite gown on the substrate (denoted by 1MLG, 2MLG, 3MLG). Peak B was attributed to σ^*, peak C to the presence of Si vacancies in the topmost layers of the substrate. Adopted from Ref. [39].

Figure 7.4 shows a modification of the previously presented IPES measurement of the only identified peak, now also including the results from the theoretical model. In figure 6.9b) a peak height (blue) is shown together with expected values for σ^* calculated using the TB model, both with electron-phonon coupling (green) and without (red). It can be seen that even strong electron-phonon coupling does not show a significantly different expected intensity, which should still be suppressed at Γ. The suppres-

sion of intensity is also preserved even if the coupling constant c_i between the initial state and incoming electron is varied.

In the measured data, the intensity is non-vanishing at normal incidence which suggests that the measured band is not a σ^* band and could have been previously misjudged [39]. Moreover, peak height is asymmetry, which can be attributed to experimental geometry and a related polarization pre-factor which was omitted in the calculations[4]. It is worth reminding that both the detector and the electron gun were fixed during the measurement, whereas the sample was rotated. This resulted in a change of angle between the sample normal and the detector.

The minimum of the energy band around 3.5 eV is below the vacuum level present at 4.3±0.2 eV (determined by target current spectroscopy [69, 70]) which allows for the existence of image potential states. This is in good agreement with previously published results using 2PPES [36], where the first two image-potential states were found at 1.05 and 0.78 eV below the vacuum level. Now, consider figure 7.4c) showing the peak width. The averaged peak width (FWHM) is just slightly below 0.5 eV which is higher than the resolution of the instrument (0.35 eV). If the energy difference of 0.27 eV between the two image potential states is considered and the same intensity of the peaks is considered (the peaks are very sharp and so here two delta-like peaks are considered), a convolution with the instrument resolution of 350 meV results in a Gaussian-like peak with FWHM of approximately 0.5 eV. This FWHM agrees well with the determined peak width.

From the fit in Fig. 6.9a), the effective mass was determined to be 1.5 ± 0.2 free-electron masses which is above the expected free-electron mass for image potential states [36]. It is worth noting that the fit is rather rough and its minima is not at $\boldsymbol{K}_\parallel = 0$ as it should be [5]. The bad fit can be attributed to an insufficient amount of data points . For further judgements of the dispersion, more data points are needed.

[4] In the simulations, the polarization term was considered to be constant (see section 3.3.4), resulting in an isotropic photon emission to whole half-space above the sample.

[5] The value of $0.1\,\text{Å}^{-1}$ for the minimum of the band would correspond to a misalignment of the sample of 6°. This cannot happen - the sample holder holds stiff in the manipulator and the angle deviation is typically within 1°)

a)

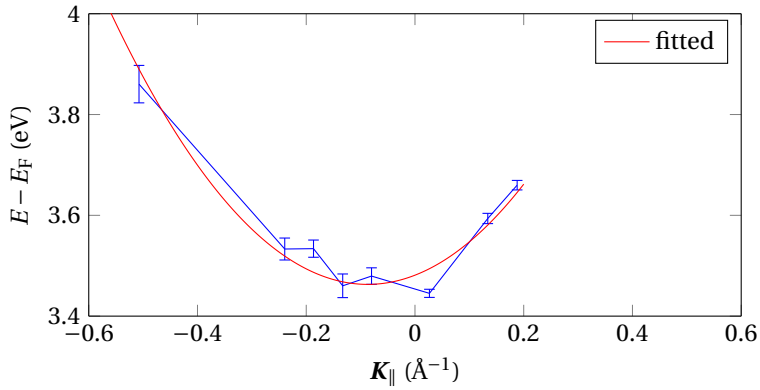

b)

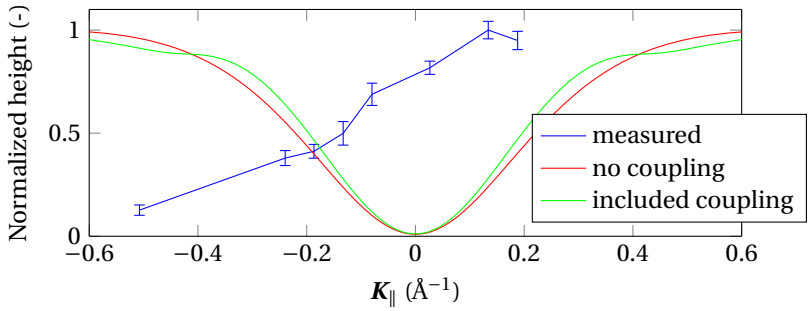

c)

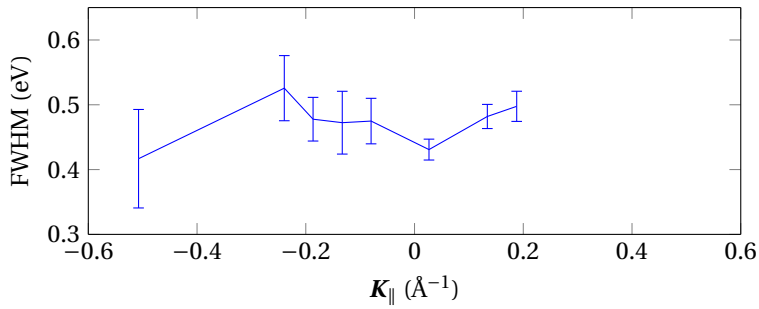

Figure 7.4: Peak dispersion a), normalized peak height b) and peak width c) are shown. In panel a), measured values denoted blue (the blue line is just to guide the eye, measured point are displayed with error bars) are fitted with a parabolic fit (red). The dispersion seems to deviate a lot from the parabolic shape but for further judgements, better measurement is needed. In panel b), measured normalized peak height is shown (blue). The height is non-symmetric probably due to the geometry of the apparatus and experimental alignment. Expected values from the band structure simulation both considering strong electron-phonon coupling and no coupling are shown for comparison (green and read lines respectively). The last panel (c)) shows FWHM of the measured peak which is bigger than the instrument broadening (0.35 eV, 0.1 Å^{-1}).

7.4 Final Thoughts and Further Work

The experiments of ML graphite on 4H-SiC presented in this work showed only one resolved state which was assigned to the two lowest image-potential states. However, the surface quality judgement of the sample was just based on a LEED pattern which can be misleading since no reasonable data can be obtained even if the LEED pattern is visible. Hence, further surface quality investigation (such as ARPES as mentioned in section 2.2.2) should be performed before the next KRIPES measurements.

The simulations or KRIPES intensity showed that no intensity should be expected at the minimum of the lowest unoccupied σ^* bands. The fact that the lowest state was attributed to the image potential state suggests that further investigation at higher energy should be done. Further experiments should be started at higher angles (such as 10° from normal incidence) where the intensity of the peak should be sufficient for certain identification. The fact that the intensity is vanishing at normal incidence complicates an investigation of possible electron-phonon coupling in the σ^* band or other many-body effects. If the band is found, the experiment should be performed with 1° angle increments to provide a sufficient data set to see the deviations from the parabolic shape. To further support the measurement, the polarization factor in the matrix element calculation and the coupling constant between the initial state and in incoming electron should be included.

This complication with a possible investigation of electron-phonon coupling in the lowest σ^* band rose a question about the possibility to investigate electron-phonon coupling in the image-potential state. To the author best knowledge this has not been done for graphene, but already some studies exist with a connection to metallic surfaces [128, 129]. As presented in Ref. [37], the image-potential states wave function has a significant overlap with the atomic orbitals and thus the coupling should be possible. However, since the image-potential states are below the vacuum level, different spectroscopic techniques such as 2PPES should be considered.

In order to be able perform the precise KRIPES experiments at NTNU laboratory, the electron detector should be modified to improve its resolution. As discussed in section 2.3.3, this can be achieved by a different type of window introduced in the photon path, for instance made out of SrF_2. Ideally, the window should be removable without opening the vacuum chamber in order to allow both high efficiency and high resolution measurements.

Chapter 8

Conclusion

The aim of the thesis was to simulate inverse photoemission intensity from the lowest unoccupied σ^* band and consequently measure graphene band structure in order to investigate the origin of the previously claimed σ^* band found in the literature. The tight-binding model of graphene was implemented and justified to model the band structure. In the three-step model and with a free-electron like initial state and dipole approximation, an emission spectrum for inverse photoemission was calculated. To fully understand the two lowest unoccupied σ^* bands of graphene, a possible coupling to transversal optical phonons was included to account for many-body interactions in graphene. This coupling has been previously showed to play a significant role in the occupied σ bands, and due to the symmetry properties of the bands can be also expected in the unoccupied σ^* bands.

The results from the calculations showed zero intensity at normal electron incidence which is contradictory to previously published experimental results, where the claimed σ^* state was non-vanishing at normal electron incidence. This suggests that the previously found state does not originate from intralayer atomic orbitals, but rather corresponds to a different state, such as an image potential state.

In order to measure the band structure experimentally, both the energy and momentum resolution of home-lab apparatus had to be measured. Especially the former, which was found to be below 0.80 eV, is too limiting for detailed measurements of the band structure. The final experiments of mono-layer graphene on 4H-SiC were therefore performed at Physikalisches Institut, Münster. Notwithstanding the graphene sample annealing at 500 °C, the surface quality check by low energy electron diffraction and the sample placed in an ultra high vacuum, a single peak with a minimum at approximately 3.5 eV above the Fermi level was identified. The energy of the peak minimum corresponds well to the previous experiments, where, however, other peaks were found.

The experiment nonetheless used a different polytype of the substrate which can give a rise to different observed states.

The position of the peak at 0.8 eV below the vacuum level is in good agreement with previously theoretically predicted image-potential states which were studied using two-photon photoemission spectroscopy. The intensity of the measured peak was found to decrease towards higher electron incidence angles and being non-vanishing close to the normal incidence. This is again contradicts the obtained values from the theoretical model. Moreover, the width of the state was found to be bigger than the energy broadening of the experiment. The determined width corresponds well to two peaks separated by 0.25 eV which merge together due to the experimental resolution. This again agrees well with previous experiments and theoretical predictions, where the two lowest image-potential states are separated by 0.27 eV. For further judgements about the origin of the state, further experimental work is required regarding both sample quality investigation and inverse photoemission measurements.

The overall results suggest that the lowest unoccupied σ^* states are present at higher energies (as predicted by first principle calculations), however, their observation and identification seems to be rather difficult due to vanishing matrix elements at a normal electron incidence. This rises the question of whether or not a strong electron-phonon coupling can be observed in the lowest σ^* bands in graphene using inverse photoemission spectroscopy.

Looking back to the results, it can be seen that an understanding of the band structure and band origin of one of the theoretically simplest materials, graphene, has proved itself to be extremely difficult and spans far beyond this thesis.

Appendix A

Acronyms

1BZ FirstBrillouin zone

1D One-dimensional

2BZ SecondBrillouin zone

2D Two-dimensional

2PPES Two-photon photo-emission spectroscopy

3D Three-dimensional

ARPES Angle resolved photo-emission spectroscopy

BL Bi-layer

BZ Brillouin zone

PES Photo-emission spectroscopy

DFT Density function theory

FWHM Full width at half maximum

GM Green's function

HOPG Highly oriented polycrystalline graphite

IPES Inverse photo-emission spectroscopy

KRIPES $\boldsymbol{k}$-resolved inverse photo-emission spectroscopy

ML Mono-layer

LA Longitudinal acoustic

LAPACK Linear Algebra PACKage

LCAO Linear combination of atomic orbitals

LEED Low-energy electron diffraction

LEEM Low-energy electron microscopy

LO Longitudinal optical

TA Transversal acoustic

TB Tight binding

TCS Total current spectroscopy

TL Tri-layer

TO Transversal optical

TPE Tunable photon energy

VLEED Very-low-energy electron diffraction

TPE Tunable photon energy

UHV Ultra high vacuum

UV Ultra-violent

ZA Out-of-plane acoustic

ZO Out-of-plane optical

Appendix B

Additional Figures and Theory

B.1 Decomposition of Atomic Orbitals

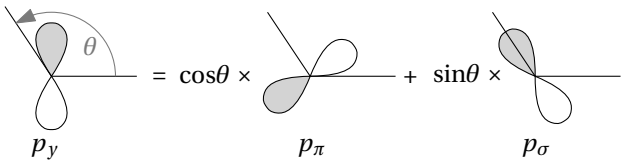

Figure B.1: Decomposition of a p_y orbital into orbitals parallel p_σ and perpendicular p_π to the line defined by two neighbouring carbon atoms.

B.2 The Full Form of The Transfer and Overlap Integral Matrices for Graphene

As described in the section 3.1.4, the transfer and overlap integral matrices can be expressed as

$$\mathbb{H} = \begin{bmatrix} \mathscr{H}_{11} & \dots & \dots & \mathscr{H}_{16} \\ \vdots & \ddots & & \vdots \\ \vdots & & \ddots & \vdots \\ \mathscr{H}_{61} & \dots & \dots & \mathscr{H}_{66} \end{bmatrix} = \begin{bmatrix} \mathbb{H}_{AA} & \mathbb{H}_{AB} \\ \mathbb{H}_{BA} & \mathbb{H}_{BB}, \end{bmatrix} \tag{B.1}$$

$$\mathbb{S} = \begin{bmatrix} \mathscr{S}_{11} & \dots & \dots & \mathscr{S}_{16} \\ \vdots & \ddots & & \vdots \\ \vdots & & \ddots & \vdots \\ \mathscr{S}_{61} & \dots & \dots & \mathscr{S}_{66} \end{bmatrix} = \begin{bmatrix} \mathbb{S}_{AA} & \mathbb{S}_{AB} \\ \mathbb{S}_{BA} & \mathbb{S}_{BB} \end{bmatrix} \tag{B.2}$$

with sub-matrices

$$\mathbb{H}_{AA} = \mathbb{H}_{BB} = \begin{bmatrix} \epsilon_{2s} & 0 & 0 \\ 0 & \epsilon_{2p} & 0 \\ 0 & 0 & \epsilon_{2p}. \end{bmatrix} \tag{B.3}$$

$$\mathbb{S}_{AA} = \mathbb{S}_{BB} = \begin{bmatrix} 1 & 0 & 0 \\ 0 & 1 & 0 \\ 0 & 0 & 1 \end{bmatrix}. \tag{B.4}$$

Elements of the sub-matrix $\mathbb{H}_{AB}$ can be written as [97]

$$\mathscr{H}_{14} = \frac{1}{N}\sum_{\boldsymbol{R},\boldsymbol{R'}}^{N} \mathrm{e}^{i\boldsymbol{k}\cdot(\boldsymbol{R'}-\boldsymbol{R})} \langle \boldsymbol{R}+\boldsymbol{R}_{\mathrm{A}}, s|\mathscr{H}|\boldsymbol{R'}+\boldsymbol{R}_{\mathrm{B}}, s\rangle = H_{ss\sigma}\sum_{i=1}^{3} \mathrm{e}^{i\boldsymbol{k}\cdot\boldsymbol{R}_i} \tag{B.5}$$

$$\mathscr{H}_{15} = \frac{1}{N}\sum_{\boldsymbol{R},\boldsymbol{R'}}^{N} \mathrm{e}^{i\boldsymbol{k}\cdot(\boldsymbol{R'}-\boldsymbol{R})} \langle \boldsymbol{R}+\boldsymbol{R}_{\mathrm{A}}, s|\mathscr{H}|\boldsymbol{R'}+\boldsymbol{R}_{\mathrm{B}}, p_x\rangle = H_{sp\sigma}\sum_{i=1}^{3} \mathrm{e}^{i\boldsymbol{k}\cdot\boldsymbol{R}_i}\cos\theta_i \tag{B.6}$$

$$\mathscr{H}_{16} = \frac{1}{N}\sum_{\boldsymbol{R},\boldsymbol{R'}}^{N} \mathrm{e}^{i\boldsymbol{k}\cdot(\boldsymbol{R'}-\boldsymbol{R})} \langle \boldsymbol{R}+\boldsymbol{R}_{\mathrm{A}}, s|\mathscr{H}|\boldsymbol{R'}+\boldsymbol{R}_{\mathrm{B}}, p_y\rangle = H_{sp\sigma}\sum_{i=1}^{3} \mathrm{e}^{i\boldsymbol{k}\cdot\boldsymbol{R}_i}\sin\theta_i \tag{B.7}$$

$$\begin{aligned} \mathscr{H}_{25} &= \frac{1}{N}\sum_{\boldsymbol{R},\boldsymbol{R'}}^{N} \mathrm{e}^{i\boldsymbol{k}\cdot(\boldsymbol{R'}-\boldsymbol{R})} \langle \boldsymbol{R}+\boldsymbol{R}_{\mathrm{A}}, p_x|\mathscr{H}|\boldsymbol{R'}+\boldsymbol{R}_{\mathrm{B}}, p_x\rangle \\ &= \sum_{i=1}^{3} \left[H_{pp\sigma}\cos^2\theta_i + H_{pp\pi}\sin^2\theta_i\right] \mathrm{e}^{i\boldsymbol{k}\cdot\boldsymbol{R}_i} \end{aligned} \tag{B.8}$$

$$\begin{aligned} \mathscr{H}_{26} &= \frac{1}{N}\sum_{\boldsymbol{R},\boldsymbol{R'}}^{N} \mathrm{e}^{i\boldsymbol{k}\cdot(\boldsymbol{R'}-\boldsymbol{R})} \langle \boldsymbol{R}+\boldsymbol{R}_{\mathrm{A}}, p_x|\mathscr{H}|\boldsymbol{R'}+\boldsymbol{R}_{\mathrm{B}}, p_y\rangle \\ &= \sum_{i=1}^{3} \left[H_{pp\sigma} - H_{pp\pi}\right] \sin\theta_i\cos\theta_i \mathrm{e}^{i\boldsymbol{k}\cdot\boldsymbol{R}_i} \end{aligned} \tag{B.9}$$

$$\begin{aligned} \mathscr{H}_{36} &= \frac{1}{N}\sum_{\boldsymbol{R},\boldsymbol{R'}}^{N} \mathrm{e}^{i\boldsymbol{k}\cdot(\boldsymbol{R'}-\boldsymbol{R})} \langle \boldsymbol{R}+\boldsymbol{R}_{\mathrm{A}}, p_y|\mathscr{H}|\boldsymbol{R'}+\boldsymbol{R}_{\mathrm{B}}, p_y\rangle \\ &= \sum_{i=1}^{3} \left[H_{pp\sigma}\sin^2\theta_i + H_{pp\pi}\cos^2\theta_i\right] \mathrm{e}^{i\boldsymbol{k}\cdot\boldsymbol{R}_i}. \end{aligned} \tag{B.10}$$

The rest of the elements of sub-matrix $\mathbb{H}_{AB}$ can be written using previously derived elements as $\mathscr{H}_{24} = -\mathscr{H}_{15}$, $\mathscr{H}_{34} = -\mathscr{H}_{16}$ and $\mathscr{H}_{35} = \mathscr{H}_{26}$. Due to the identical carbon atoms in the unit cell, sub-matrix $\mathbb{H}_{BA}$ is just a complex conjugation of $\mathbb{H}_{AB}$.

Elements of the sub-matrix $\mathbb{S}_{AB}$ have the same form as elements of $\mathbb{H}_{AB}$ with only $H_{ss\sigma}$, $H_{sp\sigma}$, $H_{pp\sigma}$ and $H_{pp\pi}$ exchanged for $S_{ss\sigma}$, $S_{sp\sigma}$, $S_{pp\sigma}$ and $S_{pp\pi}$ in the final expres-

sions. Here, an example of $\mathscr{S}_{14}$ is shown:

$$\mathscr{S}_{14} = \frac{1}{N}\sum_{\boldsymbol{R},\boldsymbol{R}'}^{N} \mathrm{e}^{i\boldsymbol{k}\cdot(\boldsymbol{R}'-\boldsymbol{R})}\langle \boldsymbol{R}+\boldsymbol{R}_{\mathrm{A}}, s|\boldsymbol{R}'+\boldsymbol{R}_{\mathrm{B}}, s\rangle = S_{ss\sigma}\sum_{i=1}^{3}\mathrm{e}^{i\boldsymbol{k}\cdot\boldsymbol{R}_i}. \tag{B.11}$$

Similarly, $\mathbb{S}_{BA}$ is just a complex conjugated $\mathbb{S}_{AB}$.

B.3 Real Atomic Orbitals

For better illustration, the whole theory of this work was described using the real atomic orbitals, s, p_x, p_y and p_z which are defined as a linear combination of the complex hydrogen-like orbitals and are defined as

$$s = R_{n,0}(r)\,Y_0^0(\theta,\phi), \tag{B.12}$$

$$p_x = \frac{1}{\sqrt{2}}R_{n,1}(r)\left[Y_1^1(\theta,\phi) - Y_1^{-1}(\theta,\phi)\right], \tag{B.13}$$

$$p_y = \frac{1}{i\sqrt{2}}R_{n,1}(r)\left[Y_1^1(\theta,\phi) + Y_1^{-1}(\theta,\phi)\right], \tag{B.14}$$

$$p_z = R_{n,1}(r)\,Y_1^0(\theta,\phi), \tag{B.15}$$

where n is the main quantum number, and for valence electrons which contribute to electronic band structure $n = 2$. $R_{n,l}(r)$ and $Y_l^m(\theta,\phi)$ are the radial and the angular part of atomic orbitals (the latter is known as spherical harmonics [112]), l and m are orbital and magnetic quantum numbers respectively. The radial part can be written as

$$R_{n,l}(r) \propto \mathrm{e}^{r/nr_0}\left[\frac{2r}{nr_0}\right]^l L_{n-l-1}^{2l+1}\left(\frac{2r}{nr_0}\right), \tag{B.16}$$

where r_0 is the characteristic orbital radius and for C is $r_0 = 62\times10^{-12}\,\mathrm{m}$ [130, 131] and $L_{n-l-1}^{2l+1}\left(\frac{2r}{nr_0}\right)$ are associated Laguerre polynomials [112]. The angular parts can be written as

$$Y_0^0(\theta,\phi) = \sqrt{\frac{1}{4\pi}} \tag{B.17}$$

$$Y_1^0(\theta,\phi) = \sqrt{\frac{3}{4\pi}}\cos(\theta) \tag{B.18}$$

$$Y_1^1(\theta,\phi) = \sqrt{\frac{3}{8\pi}}\sin(\theta)\mathrm{e}^{i\phi} \tag{B.19}$$

$$Y_1^{-1}(\theta,\phi) = \sqrt{\frac{3}{8\pi}}\sin(\theta)\mathrm{e}^{-i\phi} \tag{B.20}$$

The Fourier transform of $R_{n,l}(r)Y_l^m(\theta,\phi)$ has a form $f_{n,l}(k)Y_l^m(\theta_{\boldsymbol{k}},\phi_{\boldsymbol{k}})$ [111, 112], where $Y_l^m(\theta_{\boldsymbol{k}},\phi_{\boldsymbol{k}})$ are the same spherical harmonics as defined in Eq. (B.17-B.20). The radial part can be written as [112]

$$f_{n,l}(k) \propto \frac{(-ik')^l}{(k'^2+1)^{l+2}} C_{n-l-1}^{l+1}\left(\frac{k'^2-1}{k'^2+1}\right), \tag{B.21}$$

where $C_{n-l-1}^{l+1}\left(\frac{k'^2-1}{k'^2+1}\right)$ are Gegenbauer polynomials and $k' = nkr_0$. Using the definitions for real atomic orbitals (Eq. (B.12-B.15))), the real atomic orbitals in $\boldsymbol{k}$-space representation can be expressed as

$$s = f_{n,0}(k)\,Y_0^0(\theta_{\boldsymbol{k}},\phi_{\boldsymbol{k}}), \tag{B.22}$$

$$p_x = \frac{1}{\sqrt{2}} f_{n,1}(k)\left[Y_1^1(\theta_{\boldsymbol{k}},\phi_{\boldsymbol{k}}) - Y_1^{-1}(\theta_{\boldsymbol{k}},\phi_{\boldsymbol{k}})\right], \tag{B.23}$$

$$p_y = \frac{1}{i\sqrt{2}} f_{n,1}(k)\left[Y_1^1(\theta_{\boldsymbol{k}},\phi_{\boldsymbol{k}}) + Y_1^{-1}(\theta_{\boldsymbol{k}},\phi_{\boldsymbol{k}})\right], \tag{B.24}$$

$$p_z = f_{n,1}(k)\,Y_1^0(\theta_{\boldsymbol{k}},\phi_{\boldsymbol{k}}). \tag{B.25}$$

B.4 Energy Resolution Analysis of Instrument Data-Sheet

Figure B.2 shows energy analysis of the data-sheet listed plot. The data were digitalized from the data-sheet [**?**] and the analysis described in section 5.2 was used.

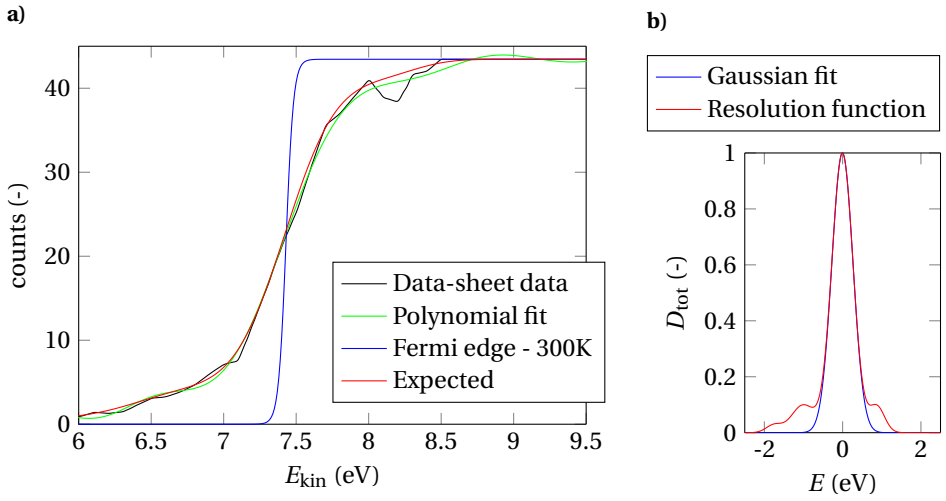

Figure B.2: Data-sheet IPES measurement of Fermi Edge on polycrystalline silver (111) a) and apparatus energy resolution function b). The extracted data (black) are fitted by a polynomial (green) which is then fitted by a convolution (red) of the Fermi edge (blue) the detector resolution function to D_{tot} displayed in b) (red). It can be seen that D_{tot} has a non-Gaussian shape due to a presence of a "tail".

B.5 Standard Deviation of Calculated Parallel Momenta Deviation

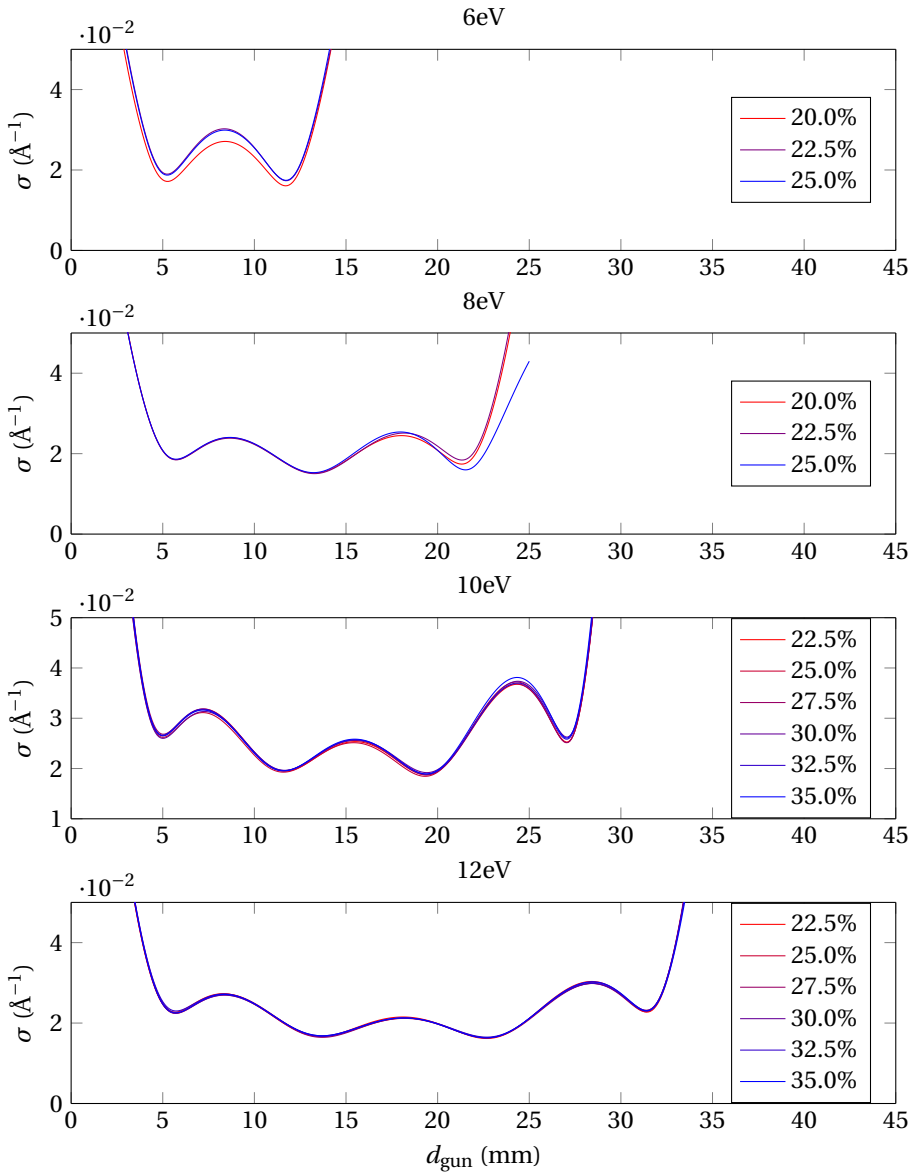

Figure B.3: Standard deviation of $\Delta \boldsymbol{K}_{\parallel}$ calculated using the method described in section 5.1. Due to the polynomial fit, standard deviation blows up at the vicinity of the electron gun as well as at a far distance from the gun. In order to improve the variations of the uncertainty, the beam profile should be measured at more values of x.

Bibliography

[1] P. R. Wallace; The band theory of graphite. *Physical Review*, 71(9):622–634, May 1947.

[2] K. S. Novoselov; Electric field effect in atomically thin carbon films. *Science*, 306(5696):666–669, October 2004.

[3] Nobel Foundation; The nobel prize in physics 2010. Online, 2010. Available from: http://www.nobelprize.org/nobel_prizes/physics/laureates/2010/

[4] C. Berger; Electronic confinement and coherence in patterned epitaxial graphene. *Science*, 312(5777):1191–1196, May 2006.

[5] Y. Zhang, L. Zhang, C. Zhou; Review of chemical vapor deposition of graphene and related applications. *Accounts of Chemical Research*, 46(10):2329–2339, March 2013.

[6] K. S. Novoselov, A. K. Geim, S. V. Morozov, D. Jiang, M. I. Katsnelson, I. V. Grigorieva, S. V. Dubonos, and A. A. Firsov; Two-dimensional gas of massless dirac fermions in graphene. *Nature*, 438(7065):197–200, November 2005.

[7] J.-H. Chen, Ch. Jang., S. Xiao, M. Ishigami, M. S. Fuhrer; Intrinsic and extrinsic performance limits of graphene devices on SiO2. *Nature Nanotechnology*, 3(4):206–209, March 2008.

[8] H. Zhang, S. Virally, Q. Bao, L. K. Ping, S. Massar, N. Godbout, P. Kockaert; Z-scan measurement of the nonlinear refractive index of graphene. *Optics Letters*, 37(11):1856, May 2012.

[9] C. Lee, X. Wei., J. W., Kysar, J. Hone; Measurement of the elastic properties and intrinsic strength of monolayer graphene. *Science*, 321(5887):385–388, July 2008.

[10] S. Sahu and G. C. Rout; Band gap opening in graphene: a short theoretical study. *International Nano Letters*, 7(2):81–89, March 2017.

[11] R. Balog et al.; Bandgap opening in graphene induced by patterned hydrogen adsorption. *Nature Materials*, 9(4):315–319, March 2010.

[12] G. Giovannetti, P. A. Khomyakov, G. Brocks , P. J. Kelly, and J. van den Brink; Substrate-induced band gap in graphene on hexagonal boron nitride:ab initio density functional calculations. *Physical Review B*, 76(7), August 2007.

[13] J. R. Williams, L. DiCarlo, and C. M. Marcus; Quantum hall effect in a gate-controlled p-n junction of graphene. *Science*, 317(5838):638–641, August 2007.

[14] G. Gu, S. Nie., R. M. Feenstra, R. P. Devaty, W. J. Choyke, W. K. Chan, M. G. Kane; Field effect in epitaxial graphene on a silicon carbide substrate. *Applied Physics Letters*, 90(25):253507, June 2007.

[15] G. Liang, N. Neophytou, D. E. Nikonov. M. S. Lundstrom; Performance projections for ballistic graphene nanoribbon field-effect transistors. *IEEE Transactions on Electron Devices*, 54(4):677–682, April 2007.

[16] S. Kim, J. K. Seo, J. H. Park, Y. Song Y. S. Meng, M. J. Heller; White-light emission of blue-luminescent graphene quantum dots by europium (III) complex incorporation. *Carbon*, 124:479–485, November 2017.

[17] M.C. Chong, N. Afshar-Imani., F. Scheurer, C. Cardoso, A. Ferrett,i D. Prezzi, G. Schull; Bright electroluminescence from single graphene nanoribbon junctions. *Nano Letters*, 18(1):175–181, December 2017.

[18] A. I. Chernov et al.; Optical properties of graphene nanoribbons encapsulated in single-walled carbon nanotubes. *ACS Nano*, 7(7):6346–6353, June 2013.

[19] C. E. P. Villegas, P. B. Mendonça, and A. R. Rocha; Optical spectrum of bottom-up graphene nanoribbons: towards efficient atom-thick excitonic solar cells. *Scientific Reports*, 4(1), October 2014.

[20] Y. Cao, V. Fatemi, S. Fang K. Watanabe T. Taniguchi E. Kaxiras P. Jarillo-Herrero; Unconventional superconductivity in magic-angle graphene superlattices. *Nature*, 556(7699):43–50, March 2018.

[21] A.Takayama T. Takahashi S.Hasegawa S. Ichinokura, K. Sugawara; Superconducting calcium-intercalated bilayer graphene. *ACS Nano*, 10(2):2761–2765, January 2016.

[22] L. Ju et al.; Topological valley transport at bilayer graphene domain walls. *Nature*, 520(7549):650–655, April 2015.

[23] P. Rickhaus et al.; Transport through a network of topological states in twisted bilayer graphene. 2018.

[24] S. Hufner; *Photoelectron Spectroscopy: Principles and Applications (Springer Series in Solid-state Sciences)*. Springer Verlag, February 1996.

[25] P. Puschnig and D. Lüftner; Simulation of angle-resolved photoemission spectra by approximating the final state by a plane wave: From graphene to polycyclic aromatic hydrocarbon molecules. *Journal of Electron Spectroscopy and Related Phenomena*, 200:193–208, April 2015.

[26] S. Y. Zhou, D. A. Siegel, A. V. Fedorov, A. Lanzara; Kohn anomaly and interplay of electron-electron and electron-phonon interactions in epitaxial graphene. *Physical Review B*, 78(19), November 2008.

[27] A. Bostwick, T.Ohta, T. Seyller, K. Horn, E. Rotenberg; Quasiparticle dynamics in graphene. *Nature Physics*, 3(1):36–40, December 2006.

[28] F. Mazzola, J. W. Wells., R. Yakimova et al.; Kinks in the σ band of graphene induced by electron-phonon coupling. *Phys. Rev. Lett.*, 111:216806, November 2013.

[29] F. Mazzola, T. Frederiksen, T. Balasubramanian., P.Hofmann B. Hellsing J. W. Wells; Strong electron-phonon coupling in the sigma band of graphene. *Phys. Rev. B*, February 2017.

[30] J. Bardeen, L. N. Cooper, J. R. Schrieffer; Microscopic theory of superconductivity. *Physical Review*, 106(1):162–164, April 1957.

[31] Nobel Foundation; The nobel prize in physics 1972. Online, 1972. Available from: http://www.nobelprize.org/nobel_prizes/physics/laureates/1972/.

[32] Y. Ge, A. Y. Liu; Phonon-mediated superconductivity in electron-doped single-layer MoS_2: A first-principles prediction. *Physical Review B*, 87(24), June 2013.

[33] M. D. Kapetanakis et al.; Low-loss electron energy loss spectroscopy: An atomic-resolution complement to optical spectroscopies and application to graphene. *Physical Review B*, 92(12), September 2015.

[34] E. Kogan, V. U. Nazarov; Symmetry classification of energy bands in graphene. *Physical Review B*, 85(11), March 2012.

[35] R. Saito, G. Dresselhaus, M. S. Dresselhaus; *Physical properties of carbon nanotubes*. World Scientific, 1998.

[36] D. Niesner, T. Fauster; Image-potential states and work function of graphene. *Journal of Physics: Condensed Matter*, 26(39):393001, August 2014.

[37] V. M. Silkin, J. Zhao, F. Guinea, E. V. Chulkov, P. M. Echenique, H. Petek; Image-potential states in graphene. *Physical Review B*, 80(12), September 2009.

[38] Y.-P. Lin, Y. Ksari, J. Prakash, L. Giovanelli, J.-C. Valmalette, J.-M. Themlin; Nitrogen-doping processes of graphene by a versatile plasma-based method. *Carbon*, 73:216–224, July 2014.

[39] Y.-P. Lin, Y. Ksari, D. Aubel, S. Hajjar-Garreau, G.Borvon, Y. Spiegel,L. Roux, L.Simon. J.-M. Themlin; Efficient and low-damage nitrogen doping of graphene via plasma-based methods. *Carbon*, 100:337–344, April 2016.

[40] L. Kong et al.; Graphene/substrate charge transfer characterized by inverse photoelectron spectroscopy. *The Journal of Physical Chemistry C*, 114(49):21618–21624, November 2010.

[41] N. A. W. Holzwarth, S. G. Louie, S. Rabii; X-ray form factors and the electronic structure of graphite. *Physical Review B*, 26(10):5382–5390, November 1982.

[42] H. Ohsawa, T. Takahashi, T. Kinoshita, Y. Enta, H. Ishii, and T. Sagawa; Unoccupied electronic band structure of graphite studied by angle-resolved inverse photoemission. *Solid State Communications*, 61(6):347–350, February 1987.

[43] H. Carstensen R. Claessen and M. Skibowski; Conduction-band structure of graphite single crystals studied by angle-resolved inverse photoemission and target-current spectroscopy. *Physical Review B*, 38(17):12582–12588, December 1988.

[44] J. Lehmann, M. Merschdorf, A. Thon, S. Voll,W. Pfeiffer; Properties and dynamics of the image potential states on graphite investigated by multiphoton photoemission spectroscopy. *Physical Review B*, 60(24):17037–17045, December 1999.

[45] S. Tanaka, K. Mukai, J. Yoshinobu; Direct observation of the electron-phonon coupling between empty states in graphite via high-resolution electron energy-loss spectroscopy. *Physical Review B*, 95(16), April 2017.

[46] B. Aufray et. al; Graphene-like silicon nanoribbons on Ag(110): A possible formation of silicene. *Applied Physics Letters*, 96(18):183102, May 2010.

[47] A. J. Mannix et al.; Synthesis of borophenes: Anisotropic, two-dimensional boron polymorphs. *Science*, 350(6267):1513–1516, December 2015.

[48] Pierre Delhaes, editor; *Graphite and Precursors (World of Carbon)*. CRC Press, 2000.

[49] D. R. Cooper et al.; Experimental review of graphene. *ISRN Condensed Matter Physics*, 2012:1–56, 2012.

[50] Charles Kittel, Paul McEuen, and Paul McEuen; *Introduction to solid state physics*, volume 8. Wiley New York, 1996.

[51] H. Bruus and K. Flensberg; *Many-body quantum theory in condensed matter physics: an introduction*. Oxford university press, 2004.

[52] S. Konschuh, M. Gmitra, J. Fabian; Tight-binding theory of the spin-orbit coupling in graphene. *Physical Review B*, 82(24), December 2010.

[53] P. M. Echenique, J. B. Pendry. The existence and detection of rydberg states at surfaces. *Journal of Physics C: Solid State Physics*, 11(10):2065–2075, May 1978.

[54] D. Nobis, M. Potenz, D. Niesner, T. Fauster; Image-potential states of graphene on noble-metal surfaces. *Physical Review B*, 88(19), November 2013.

[55] K.Takahashi, M. Imamura, I. Yamamoto, J. Azuma, and M. Kamada; Image-potential states in monolayer, bilayer, and trilayer epitaxial graphene studied with time- and angle-resolved two-photon photoemission spectroscopy. *Physical Review B*, 89(15), April 2014.

[56] S. Bose et al.; Image-potential states as a quantum probe of graphene interfaces. *New Journal of Physics*, 12(2):023028, 2010.

[57] Charles Kittel; *Quantum theory of solids*. Wiley, 1987.

[58] T. Aizawa, R. Souda, S. Otani, Y. Ishizawa, and C. Oshima; Bond softening in monolayer graphite formed on transition-metal carbide surfaces. *Physical Review B*, 42(18):11469–11478, December 1990.

[59] T. Sohie; *Electrons and phonons in graphene: electron-phonon coupling, screening and transport in the field effect setup*. PhD thesis, Université Pierre et Marie Curie-Paris VI, 2015.

[60] C. Nordling, E. Sokolowski, K.Siegbahn; Precision method for obtaining absolute values of atomic binding energies. *Physical Review*, 105(5):1676–1677, March 1957.

[61] S. K. Mahatha, K. S. R. Menony T. Balasubramanian; Unoccupied electronic structure of graphite probed by angle-resolved photoemission spectroscopy. *Physical Review B*, 84(11), September 2011.

[62] T. L. Miller et al.; Resolving unoccupied electronic states with laser ARPES in bismuth-based cuprate superconductors. *Physical Review B*, 91(8), February 2015.

[63] Th. Fauster; Two-photon photoemission. *Progress in Surface Science*, 46(2-3):177–186, June 1994.

[64] H. Petek, S. Ogawa; Femtosecond time-resolved two-photon photoemission studies of electron dynamics in metals. *Progress in Surface Science*, 56(4):239–310, December 1997.

[65] W. Steinmann; Spectroscopy of image-potential states by two-photon photoemission. *Applied Physics A Solids and Surfaces*, 49(4):365–377, October 1989.

[66] T. Fauster, W. Steinmann; Two-photon photoemission pectroscopy of image states. In *Photonic Probes of Surfaces*, pages 347–411. Elsevier, 1995.

[67] N. V. Smith; Inverse photoemission. *Reports on Progress in Physics*, 51(9):1227–1294, September 1988.

[68] M. P. Seah, W. A. Dench; Quantitative electron spectroscopy of surfaces: A standard data base for electron inelastic mean free paths in solids. *Surface and Interface Analysis*, 1(1):2–11, February 1979.

[69] S.A. Komolov, L.T. Chadderton; Total current spectroscopy. *Surface Science*, 90(2):359–380, December 1979.

[70] P. J. Møller and M. H Mohamed, Total current spectroscopy. *Vacuum*, 35(1):29–37, January 1985.

[71] V. N. Strocov, H. I. Starnberg, P. O. Nilsson, H. E. Brauer, L. J. Holleboom; New method for absolute band structure determination by combining photoemission with very-low-energy electron diffraction: Application to layered VSe_2. *Physical Review Letters*, 79(3):467–470, July 1997.

[72] J. Jobst, J. Kautz, D. Geelen, R. M. Tromp, S. J. van der Molen; Nanoscale measurements of unoccupied band dispersion in few-layer graphene. *Nature Communications*, 6(1), November 2015.

[73] J.J. Lander; Low-energy electron diffraction and surface structural chemistry. *Progress in Solid State Chemistry*, 2:26–116, January 1965.

[74] K. V. Emtsev, F. Speck, Th. Seyller, L. Ley and J. D. Riley; Interaction, growth, and ordering of epitaxial graphene on SiC{0001} surfaces: A comparative photoelectron spectroscopy study. *Physical Review B*, 77(15), April 2008.

[75] I. R. Collins, P. T. Andrews, A. R. Law; Unoccupied electronic states of single-crystal graphite by angle-resolved ultraviolet inverse photoemission. *Physical Review B*, 38(18):13348–13354, December 1988.

[76] N. G. Stoffel, P. D. Johnson; A low-energy high-brightness electron gun for inverse photoemission. *Nuclear Instruments and Methods in Physics Research Section A: Accelerators, Spectrometers, Detectors and Associated Equipment*, 234(2):230–234, February 1985.

[77] P. W. Erdman, E. C. Zipf; Low-voltage, high-current electron gun. *Review of Scientific Instruments*, 53(2):225–227, February 1982.

[78] P. Martensson; W.-X. Ni, G. V. Hansson, J. M. Nicholls, B. Reihl; Surface electronic structure of Si(111)7×7-Ge and Si(111)5×5-Ge studied with photoemission and inverse photoemission. *Physical Review B*, 36(11):5974–5981, October 1987.

[79] D.T. Pierce, F. Meier, P. Zürcher; Direct observation of spin dependent electronic structure of gas using spin polarized photoemission. *Physics Letters A*, 51(8):465–466, May 1975.

[80] S. D. Stolwijk, H. Wortelen, A. B. Schmidt, M. Donath; Rotatable spin-polarized electron source for inverse-photoemission experiments. *Review of Scientific Instruments*, 85(1):013306, January 2014.

[81] PSP Vacuum Technology IPES manual; Online. Accessed: 2018-06-15, Available from: http://www.pspvacuum.com/files/inverse_photoemission_ipes.pdf

[82] A. Kovacs, P. O. Nilssonm, J. Kanski; A simple apparatus for studies of uv-bremsstrahlung. *Physica Scripta*, 25(6A):791–792, June 1982.

[83] F. Schedin, G. Thornton, R. I. G. Uhrberg; Windows and photocathodes for a high resolution solid state bandpass ultraviolet photon detector for inverse photoemission. *Review of Scientific Instruments*, 68(1):41–46, January 1997.

[84] W.R. Hunter, S.A. Malo; The temperature dependence of the short wavelength transmittance limit of vacuum ultraviolet window materials—i. experiment. *Journal of Physics and Chemistry of Solids*, 30(12):2739–2745, December 1969.

[85] M. H. Reilly; Temperature dependence of the short wavelength transmittance limit of vacuum ultraviolet window materials—II theoretical, including interpretations for u.v. spectra of SiO_2, GeO_2, and Al_2O_3. *Journal of Physics and Chemistry of Solids*, 31(5):1041–1056, May 1970.

[86] D. Funnemann and H. Merz; 10 eV photon detector for inverse photoemission. *Journal of Physics E: Scientific Instruments*, 19(7):554–557, July 1986.

[87] K. C. Prince; Improved inverse photoemission detector. *Review of Scientific Instruments*, 59(5):741–742, May 1988.

[88] J. E. Lennard-Jones; The electronic structure of some diatomic molecules. *Transactions of the Faraday Society*, 25:668–686, September 1929.

[89] F. Bloch; Über die quantenmechanik der elektronen in kristallgittern. *Zeitschrift für Physik*, 52(7-8):555–600, July 1929.

[90] J. C. Slater, G. F. Koster; Simplified LCAO method for the periodic potential problem. *Physical Review*, 94(6):1498–1524, June 1954.

[91] C. Fiolhais, F. Nogueira, M. A. L. Marques, editors; *A Primer in Density Functional Theory*. Springer Berlin Heidelberg, 2003.

[92] E. L. Shirley, L. J. Terminello, A. Santoni, F. J. Himpsel; Brillouin-zone-selection effects in graphite photoelectron angular distributions. *Physical Review B*, 51(19):13614–13622, May 1995.

[93] E. Pavarini, A. Lichtenstein, D. Vollhardt,d E. Koch; The LDA+ DMFT approach to strongly correlated materials. Technical report, Theoretische Nanoelektronik, October 2011.

[94] G. H. Wannier; The structure of electronic excitation levels in insulating crystals. *Physical Review*, 52(3):191–197, August 1937.

[95] Gilbert Strang; *Linear Algebra and Its Applications, 4th Edition*. Cengage Learning, 2006.

[96] LAPACK; online. Accessed: 2018-06-15, Aavailable from: http://www.netlib.org/lapack/.

[97] B. Gharekhanlou, S. Khorasani; *Graphene: Properties, Synthesis and Applications (Nanothechnology Science and Technology)*. Nova Science Pub Inc, 2012.

[98] W. Schattke, M. A. Van Hove, editors; *Solid-State Photoemission and Related Methods*. Wiley-VCH Verlag GmbH, October 2003.

[99] G. Grimvall; The electron-phonon interaction in normal metals. *Physica Scripta*, 14(1-2):63–78, July 1976.

[100] Ph. Hofmann, I. Yu, Sklyadneva, E. D. L. Rienks, E. V. Chulkov; Electron–phonon coupling at surfaces and interfaces. *New Journal of Physics*, 11(12):125005, December 2009.

[101] A. Einstein; Die plancksche theorie der strahlung und die theorie der spezifischen wärme. *Annalen der Physik*, 327(1):180–190, 1907.

[102] P. Debye; Zur theorie der spezifischen wärmen. *Annalen der Physik*, 344(14):789–839, 1912.

[103] J. B. Pendry; Theory of inverse photoemission. *Journal of Physics C: Solid State Physics*, 14(9):1381–1391, March 1981.

[104] W. E. Spicer; Photoemissive, photoconductive, and optical absorption studies of alkali-antimony compounds. *Physical Review*, 112(1):114–122, October 1958.

[105] D. P. Woodruff, N. V. Smith, P. D. Johnson, W. A. Royer; k-resolved inverse photoelectron spectroscopy and its application to Cu(001), Ni(001), and Ni(110). *Physical Review B*, 26(6):2943–2955, September 1982.

[106] J. C. Fuggle; *Unoccupied Electronic States: Fundamentals for Xanes, Eels, Ips and Bis (Topics in Applied Physics)*. Springer Verlag, 1992.

[107] R. Matzdorf; Investigation of line shapes and line intensities by high-resolution UV-photoemission spectroscopy — some case studies on noble-metal surfaces. *Surface Science Reports*, 30(4-5):153–206, January 1998.

[108] C Kirkegaard, T K Kim, Ph Hofmann; Self-energy determination and electron–phonon coupling on bi(110). *New Journal of Physics*, 7:99–99, April 2005.

[109] M. Budke, T. Allmers, M. Donath; Inverse photoemission with energy resolution better than 200 mev. *Review of Scientific Instruments*, 78(8):083903, 2007.

[110] S.Moser; An experimentalist's guide to the matrix element in angle resolved photoemission. *Journal of Electron Spectroscopy and Related Phenomena*, 214:29–52, January 2017.

[111] B. Podolsky and L. Pauling; The momentum distribution in hydrogen-like atoms. *Physical Review*, 34(1):109–116, July 1929.

[112] Gordon W F Drake; *Springer Handbook of Atomic, Molecular, and Optical Physics*. Springer-Verlag New York Inc., 2006.

[113] B. Trninić-Radja and M. Šunjić; Inverse photoemission from electronic surface states: Intensity, angular, and polarization dependence. *Physical Review B*, 42(12):7409–7415, October 1990.

[114] M. Donath and K. Ertl; Adsorbate-induced enhancement of image-potential surface states on Ni(110). *Surface Science*, 262(1-2):L49–L54, February 1992.

[115] F. Passek and M. Donath; Spin-split image-potential-induced surface state on Ni(111). *Physical Review Letters*, 69(7):1101–1104, August 1992.

[116] D. Straub and F. J. Himpsel; Identification of image-potential surface states on metals. *Physical Review Letters*, 52(21):1922–1924, May 1984.

[117] V. Dose, W. Altmann, A. Goldmann,U. Kolac,J. Rogozik; Image-potential states observed by inverse photoemission. *Physical Review Letters*, 52(21):1919–1921, May 1984.

[118] S. Banik, A. K. Shukla, S. R. Barman; Optimal operating conditions and characteristics of acetone/caf2 detector for inverse photoemission spectroscopy. *Review of Scientific Instruments*, 76(6):066102, June 2005.

[119] N. E. Christensen; The band structure of silver and optical interband transitions. *Physica Status Solidi (b)*, 54(2):551–563, December 1972.

[120] B. Reihl, R. R. Schlittler; Empty electronic states of silver as measured by inverse photoemission. *Physical Review B*, 29(4):2267–2269, February 1984.

[121] M. Budke, T. Allmers, M. Donath, G. Rangelov; Combined experimental setup for spin- and angle-resolved direct and inverse photoemission. *Review of Scientific Instruments*, 78(11):113909, November 2007.

[122] V. Dose, Th. Fauster, R. Schneider; Improved resolution in VUV isochromat spectroscopy. *Applied Physics A Solids and Surfaces*, 40(4):203–207, August 1986.

[123] J. Braun, C. Math, A. Postnikov, M. Donath Surface resonances versus surface states on fe(110). *Physical Review B*, 65(18), April 2002.

[124] N. Srivastava, G. He, Luxmi, P. C. Mende, R. M. Feenstra, and Y. Sun; Graphene formed on SiC under various environments: comparison of Si-face and C-face. *Journal of Physics D: Applied Physics*, 45(15):154001, March 2012.

[125] S. W. Jung et al.; Sublattice interference as the origin of σ band kinks in graphene. *Physical Review Letters*, 116(18), May 2016.

[126] C. Riedl,C. Coletti, U. Starke; Structural and electronic properties of epitaxial graphene on SiC(0001): a review of growth, characterization, transfer doping and hydrogen intercalation. *Journal of Physics D: Applied Physics*, 43(37):374009, September 2010.

[127] I. Forbeaux, J.-M Themlin, A. Charrier, F. Thibaudau,J.-M. Debever; Heteroepitaxial graphite on6h-SiC(0001): interface formation through conduction-band electronic structure. *Physical Review B*, 58(24):16396–16406, December 1998.

[128] T. S. Rahman, D. L. Mills; Electron-phonon coupling in image-potential bound states. *Physical Review B*, 21(4):1432–1444, February 1980.

[129] T. Fauster, M. Weinelt, U. Höfer; Quasi-elastic scattering of electrons in image-potential states. *Progress in Surface Science*, 82(4-6):224–243, January 2007.

[130] J. T. Waber, D. T. Cromer; Orbital radii of atoms and ions. *The Journal of Chemical Physics*, 42(12):4116–4123, June 1965.

[131] Robert J. Silbey, Robert A. Alberty, Moungi G. Bawendi; *Physical Chemistry*. Wiley, 2004.